Alma Mater Studiorum · University of Bologna

School of Science
Department of Physics and Astronomy
Master Degree in Physics

The XENONnT Neutron Veto: Performance in the Gd-doped phase

Supervisor:
Prof. Marco Selvi

Co-supervisor:
Dr. Pietro Di Gangi

Submitted by:
Virginia Mazza

Academic Year 2023/2024

Abstract

Many observations from astrophysics and cosmology point to postulate that Dark Matter (DM) constitutes approximately 85% of the universe's total mass. As of today, it still remains undetected, with Weakly Interacting Massive Particles (WIMPs) being one of the primary DM candidates.

The XENONnT experiment is located underground at the Laboratori Nazionali del Gran Sasso (LNGS) in Italy and aims to detect WIMPs using a dual-phase Time Projection Chamber (TPC) with a liquid Xenon (LXe) target. The detector contains a total of 8.6 tonnes of LXe, with 5.9 tonnes instrumented as the active target. In addition to the TPC, XENONnT is equipped with a Muon Veto and a Neutron Veto (NV), two water Cherenkov detectors used to tag backgrounds from cosmogenic and radiogenic radiation. Since data-taking began in 2021, XENONnT has performed three Scientific Runs. In Science Run 0 (SR0) and Science Run 1 (SR1), the NV was operated as a demineralized water Cherenkov detector, while Science Run 2 (SR2), starting in October 2023, marked the beginning of operations with a Gd-doped NV, reaching the current mass concentration of 500 ppm of Gadolinium sulphate (GdSO), to improve the neutron capture efficiency. The NV performance, in particular in the Gd-doped phase, is deeply studied and presented in this thesis.

XENONnT uses a comprehensive Montecarlo (MC) simulation framework that allows for detailed simulations of each subdetector. A Hitlet Simulator is specifically developed for the NV and allows to extend the simulation chain up to the photomultipliers' response, by generating simulated signals with charge and timing that closely mirror real data. The NV response to neutron captures is calibrated using an Americium Beryllium (AmBe) neutron source.

Experimental data from AmBe calibration demonstrate a significant reduction in neutron capture lifetime from 163 μs (pure water) to 75 μs (Gd-doped water). The neutron tagging efficiency of the NV increased from 53% in SR0 to 77% with GdSO in SR2. MC simulations of AmBe calibration widely agree with real data, thus confirming these findings. Overall, the introduction of Gd significantly enhanced the NV system's ability to suppress neutron-induced backgrounds by a further factor 2 with respect to the previous Science Runs with demineralized water. Based on MC simulations, a neutron tagging efficiency of $\sim$ 85% will be achieved with the final 5000 ppm GdSO concentration.

Contents

Introduction

The work developed in this master thesis is focused to investigate the Neutron Veto (NV) performance of the XENONnT Dark Matter (DM) experiment, particularly in its Gadolinium (Gd)-doped phase, aimed at enhancing the rejection of the neutron-induced background.

Chapter 1 presents an overview on DM, which constitutes approximately 85% of the universe's mass, and its elusive nature. The chapter emphasizes the importance of understanding DM, presenting key evidence from galactic rotation curves, gravitational lensing, and the Cosmic Microwave Background. It introduces the theoretical models for DM, focusing on Weakly Interacting Massive Particles (WIMPs) as prime candidates, and presents various detection techniques, including direct and indirect detection, collider searches, and future directions.

Chapter 2 introduces XENON, a leading project for DM direct detection based on a dual-phase Time Projection Chamber (TPC) filled with liquid Xenon. In particular, the XENONnT experiment is currently in operation at the underground INFN Laboratori Nazionali del Gran Sasso in Italy. This chapter details the TPC design, its cryostat, and the crucial veto systems, such as the Muon Veto and Neutron Veto. Moreover, this chapter outlines the XENONnT working principles, its capability to reject Electronic and Nuclear Recoil backgrounds, and the steps taken to enhance sensitivity in DM searches. Future advancements for the XENONnT experiment are also discussed.

Chapter 3 focuses on the Montecarlo (MC) simulations of the NV, emphasizing the detector's geometry, materials and optical properties. The simulations play a crucial role in optimizing the detector performance, in validating the relevant physical models and in making predictions about the future NV performances. XENONnT relies on a comprehensive simulation framework that encompasses all subdetectors. The PMT response is simulated using the Hitlet Simulator, a fast and efficient tool designed to generate signals with charge and timing characteristics that closely resemble real data. The NV detector is calibrated with an Americium Beryllium (AmBe) neutron source, and this chapter describes the MC simulations of calibration data. Finally, the simulation of the background from radiogenic neutrons emitted by radioactive contaminants in the detector's materials is discussed along with the expected efficiency of the NV in tagging such neutrons, therefore rejecting the induced background events in the TPC.

Chapter 4 presents the analysis and modeling of the AmBe calibration data, with a detailed description of the estimated neutron tagging efficiency. During the first two scientific runs of XENONnT, the NV has been operated as a Cherenkov detector with demineralized water. Since October 2023, Gadolinium sulphate has been dissolved into the system, thus starting the Gd-doped phase of the NV. The procedure and the impact on the optical performances are described. The chapter then discusses how the Gd doping improves the neutron tagging efficiency, the overall performance of the detector, and how Montecarlo simulations compare with experimental data.

Chapter 1

Dark Matter

This chapter introduces the concept of Dark Matter (DM), which makes up approximately 85% of the universe's mass. Despite its abundance, DM does not interact with electromagnetic forces, making it undetectable by conventional methods. Section 1.1 presents the origins of the DM hypothesis, supported by key evidence such as galaxy rotation curves, gravitational lensing, and the cosmic microwave background (CMB). Section 1.2 provides an overview of these observational proofs on galactic and extragalactic scales. Section 1.3 discusses various theoretical models and potential candidates for DM, while Section 1.4 outlines detection methods, including direct, indirect, and collider-based approaches. The chapter concludes with Section 1.5, which reviews the current challenges in DM research and highlights future prospects, particularly in overcoming the neutrino background.

1.1 Dark Matter postulation

Dark Matter remains one of the most enigmatic components of the universe, accounting for approximately 85% of its mass and about 27% of its energy density. Despite its abundance, Dark Matter does not interact with electromagnetic forces, making it invisible to telescopic observations and undetectable through direct means such as light emission or absorption. Its presence is instead inferred through gravitational effects on visible matter, such as the motion of galaxies and the bending of light (gravitational lensing). The nature of Dark Matter has profound implications for our understanding of cosmology, galaxy formation, and fundamental physics.

Dark Matter is observed through various phenomena across different cosmic scales: galaxies - which are gravitationally-bound systems composed of stars and interstellar medium with dimensions typically spanning tens of kiloparsecs - and galaxy clusters - which extend to dimensions on the order of megaparsecs - both show indications of Dark Matter. Observations consistently reveal that the gravitational effects observed exceed

what can be accounted for by the visible matter alone. This discrepancy suggests the presence of a form of matter that does not emit light and interacts with ordinary matter only through gravity.

The roots of our understanding of Dark Matter trace back to the early 20th century. Fritz Zwicky's pioneering work in 1933 on the Coma Galaxy Cluster was instrumental in revealing the existence of Dark Matter. Zwicky's study involved comparing the visible mass of the cluster with the gravitational effects it exhibited. By applying the virial theorem, he estimated the total mass of the cluster and found that the visible matter accounted for only a small fraction of the mass required to explain the observed gravitational effects. This led him to propose the existence of what he termed "Dunkle Materie" or Dark Matter (DM).

This idea was further substantiated in the 1970s by Vera Rubin and Kent Ford, who studied the rotation curves of spiral galaxies. Rubin's observations demonstrated that the rotational velocities of stars in galaxies remained constant at distances far beyond where most of the luminous matter was located. According to Newtonian mechanics, the velocity should decrease with distance from the galactic center; however, the constant velocity suggested the presence of a large amount of unseen mass extending well beyond the visible galactic disk.

These early findings have been substantiated by numerous observations across different scales. At the galactic level, discrepancies in *rotational curves* - where the observed rotational speeds of galaxies do not match predictions based solely on visible matter - provide strong evidence for Dark Matter. Similarly, *gravitational lensing*, where light from distant objects is bent around massive galaxy clusters, reveals the presence of unseen mass. On a cosmological scale, the *Cosmic Microwave Background radiation* and the *large-scale structure* of the universe further support the presence of Dark Matter. These observations collectively suggest that Dark Matter plays a crucial role in the formation and evolution of the universe.

1.2 Dark Matter evidences

The enigmatic presence of Dark Matter has become a fundamental aspect of our understanding of the universe; the evidence for Dark Matter is multifaceted, coming from a wide array of astrophysical and cosmological observations across both galactic and extra-galactic scales.

1.2.1 Galaxy Rotation Curves

One of the key pieces of evidence supporting Dark Matter arises from the study of spiral galaxies, which constitute about two-thirds of all known galaxies. These galaxies feature a flat disk with a central bulge, where most of the mass is concentrated, and spiral

arms of stars rotating rapidly around a central Supermassive Black Hole (SMBH). The rotation speed of stars and gas within these galaxies is typically measured through the 21 cm line emission of atomic Hydrogen, which provides a precise monoenergetic peak. By observing the Doppler shift in this emission, astronomers can determine the speed of the gas and, consequently, infer the rotation speed of the galaxy.

According to the principles of gravitational equilibrium, the rotation speed of an object at a distance r from the galaxy's center should be dictated by the centripetal force, which depends on the amount of mass enclosed within that radius. For spiral galaxies, most of the mass is concentrated in the central bulge, which can be approximated as a spherical distribution. As a result, one would expect the rotation speed to increase linearly with distance until reaching the edge of the bulge, and then to decrease following a square-root law. However, observations have shown that in many spiral galaxies, the rotation speed remains nearly constant even at large distances from the galactic center, far beyond the edge of the visible disk, as shown in Fig. 1.1. This discrepancy suggests the presence of a Dark Matter halo surrounding the galaxy, which contributes additional mass beyond what is accounted for by visible matter alone.

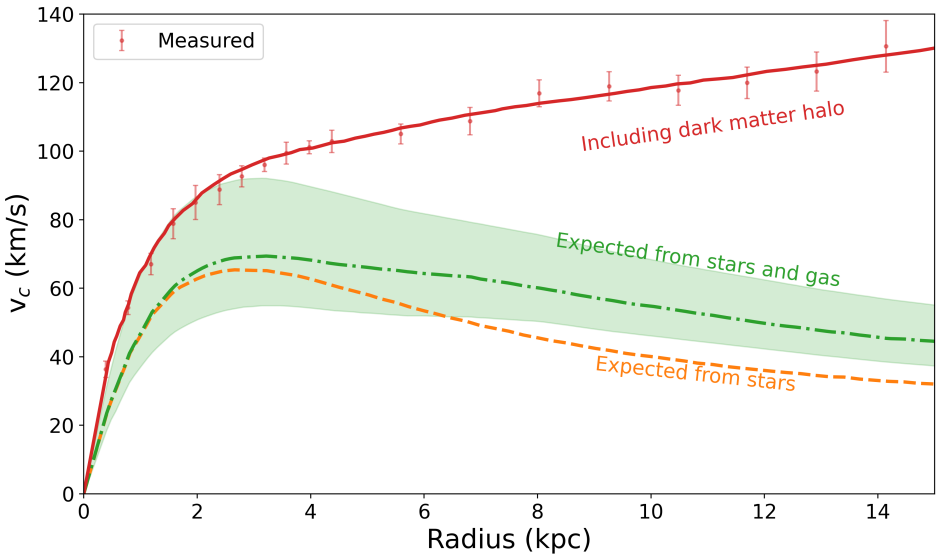

Figure 1.1: Analysis of M33 Rotation Curve, highlighting the discrepancy between measured rotation velocities (comprising ionized gas and neutral Hydrogen data) and those predicted by baryonic matter alone (stars and gas): to reconcile this difference, a DM contribution is essential. The figure combines the rotational influences of total gas, the stellar bulge, the stellar disc, and the DM halo, which are collectively integrated in quadrature to form the best-fit model (represented by the solid red line) to the observed data [1].

The study of Dark Matter began to gain traction with Fritz Zwicky's work on the

Coma Galaxy Cluster in 1933, using the virial theorem to estimate the cluster's total mass. Zwicky's calculations, which compared the observed velocity dispersion of galaxies with the visible mass, revealed a significant discrepancy, indicating the presence of unseen mass. Despite this early evidence, Zwicky's hypothesis did not achieve widespread acceptance until the 1970s. It was during this period that Vera Rubin and Kent Ford's studies of the rotation curves of spiral galaxies, such as the Andromeda Galaxy (M31) and the Triangulum Galaxy (M33), provided further support for Dark Matter. They observed that the rotation velocities of these galaxies remained unexpectedly constant at large radii, where the density of luminous matter decreases. This behavior is inconsistent with Kepler's laws, which predict that the orbital velocity should decrease as $v(r) \propto r^{-1/2}$ due to the diminishing density of stars and gas.

To reconcile these observations, the hypothesis of a Dark Matter halo was proposed. This halo, composed of invisible matter, extends well beyond the distribution of visible matter and aligns with the Navarro–Frenk–White (NFW) mass profile. The NFW profile describes the density of this dark halo as a function of radius r by the formula:

$$\rho(r) = \frac{\rho_0 R_S^3}{r(r + R_S)^2} \tag{1.1}$$

where $\rho(r)$ is the halo density, ρ_0 is the characteristic density, and R_S is the scale radius. This model has been instrumental in explaining the nearly constant rotational velocities observed in the outer regions of galaxies, providing a deeper understanding of Dark Matter's role within individual galaxies and its impact on galactic dynamics.

1.2.2 Gravitational lensing and bullet clusters

However, the pursuit of DM mysteries extends beyond the galactic boundaries, finding implications in extra-galactic phenomena. A notable instance of this is the study of gravitational lensing, especially in the context of the Bullet Cluster (1E0657-558), which provides compelling extra-galactic evidence for DM [2]. The Bullet Cluster, consisting of two colliding galaxy clusters, offers a unique opportunity to observe the interplay between baryonic and DM. The majority of the baryonic mass within these clusters exists as sparse intergalactic gas, heated during the collision and emitting intensely in the X-ray spectrum. This emission has been vividly captured by the Chandra X-ray Observatory [3] for the Bullet Cluster (1E0657-558) [4], delineating the distribution of the hot, shocked gas in detail (the pink region in Fig. 1.2). In contrast to the bright X-ray emitting gas, the galaxies within the Bullet Cluster continued their paths relatively undisturbed, following nearly unaltered ballistic trajectories through the collision. The total mass of the Bullet Cluster is inferred through weak gravitational lensing techniques. The gravitational lensing [5] mentioned here is a phenomenon predicted by Einstein's theory of General Relativity for which both clusters possess enough mass to significantly distort the space-time, acting as gravitational lenses [6]. The mass distribution, inferred

from imaging distant objects lensed by the clusters, reveals the presence of a substantial mass (depicted in blue in Fig. 1.2) where no luminous matter is observed.

Figure 1.2: Composite image of the Bullet Cluster (1E0657-558), as seen by the Hubble and Magellan optical telescopes. It features a colorized overlay highlighting mass distributions: the red regions represent data from X-ray spectroscopy conducted by the Chandra Observatory [7], while the blue areas indicate mass distributions derived from gravitational lensing measurements. Picture from [2].

1.2.3 Cosmic Microwave Background (CMB)

On the cosmological scale, the Cosmic Microwave Background (CMB) offers profound insights into the existence and role of Dark Matter in the universe. As a relic radiation from the early universe, the CMB displays a nearly perfect blackbody spectrum with a temperature of $T_0 = (2.7255 \pm 0.0006)K$, along with small anisotropies on the order of 10^{-5}. These anisotropies, which have been meticulously mapped by high-precision observations like those from the Planck collaboration [8] - as can be seen in Fig. 1.3 - are

caused by density perturbations in the early universe. Understanding these fluctuations is crucial for grasping the universe's matter and energy budget, as they reflect the complex interplay between baryonic matter, DM and radiation.

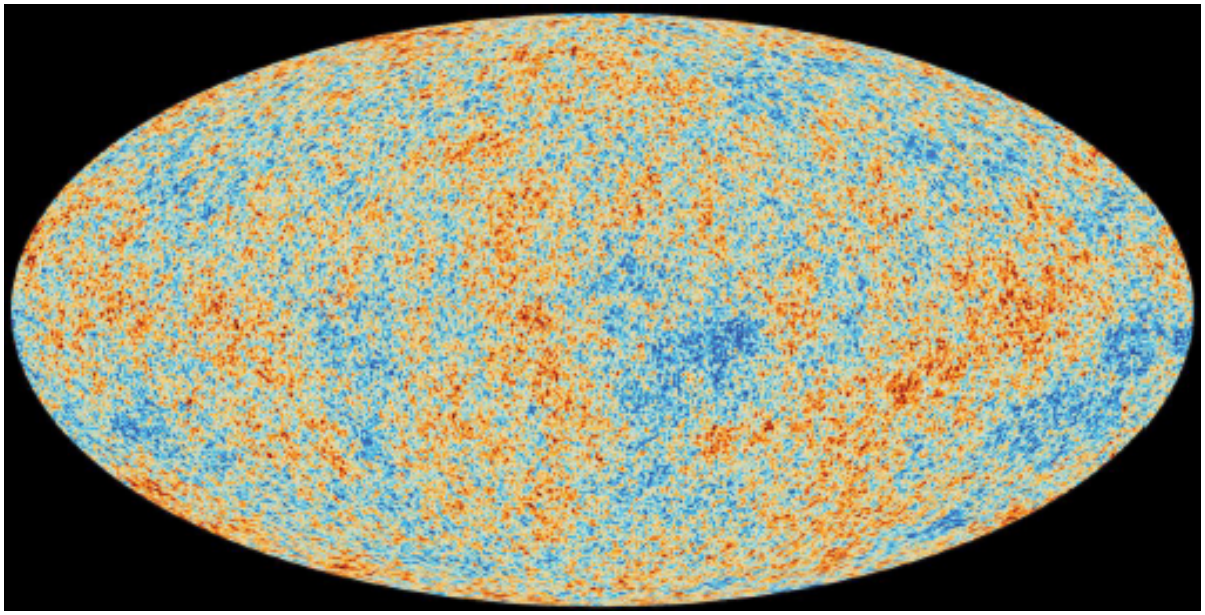

Figure 1.3: Planck data of the CMB, 2018 [9]. Different colours stand for different temperatures, highlighting the anisotropies.

The ΛCDM (Lambda Cold Dark Matter) model, strongly supported by CMB observations, describes the universe as flat, homogeneous and isotropic, undergoing accelerated expansion due to dark energy (Λ), and permeated by Cold Dark Matter (CDM). This model effectively aligns with the observed large-scale structure and galaxy formation processes, providing an explanation for the temperature anisotropies in the CMB. The model predicts the total energy density Ω_{Total}, which is given by the contributions:

$$\Omega_{Total} = \Omega_{\Lambda} + \Omega_{DM} + \Omega_{Baryon} \tag{1.2}$$

where Ω_{Λ}, Ω_{DM}, Ω_{Baryon} represent respectively the energy densities of Dark Energy, Dark Matter and Baryonic Matter.

The decomposition of CMB temperature fluctuations into spherical harmonics is a powerful technique to further analyze these anisotropies. As the multipole moment l increases, corresponding to smaller angular scales, the power spectrum derived from this expansion becomes a critical tool for testing the ΛCDM model. The exact locations of the peaks in this power spectrum are determined by the intricate interactions between radiation, matter and DM: from the excellent fit obtained reported in Fig. 1.4 it is possible to derive the main contributions to the energy density of the present-day universe

which reveal that DM constitutes approximately 85% of the mass content of the universe, underscoring its dominant role in cosmic dynamics.

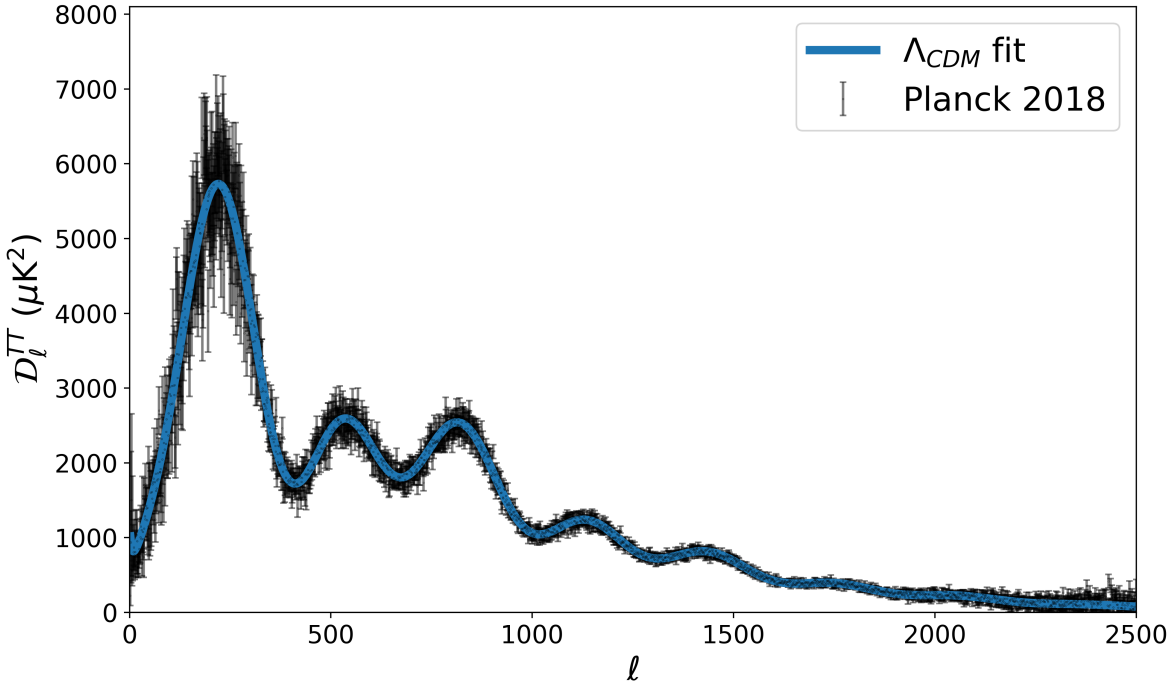

Figure 1.4: Temperature Power Spectrum of the Cosmic Microwave Background. The blue line represents the optimal fit to the Planck 2018 data release [8].

Further support for the DM hypothesis comes from Big Bang nucleosynthesis (BBN) and N-body simulations of structure formation. BBN, which is responsible for the formation of light nuclei, shows alignment with the baryon density inferred from CMB observations. N-body simulations, which frequently use CMB-derived density fluctuations as initial conditions, show remarkable agreement with observed galaxy distributions. These simulations highlight the crucial role of DM in cosmic structure formation, acting as the seeds for baryon aggregation into the large-scale structures observed today simulated in Fig. 1.5. Collectively, these findings provide the most compelling evidence for the ΛCDM model, challenging alternative theories such as modified gravity models.

1.3 Theoretical Models and Candidates

The quest to identify the constituents of Dark Matter has led to the development of a wide range of models. According to the ΛCDM model, any viable candidate for non-baryonic DM must adhere to several key properties inferred from astronomical and cosmological

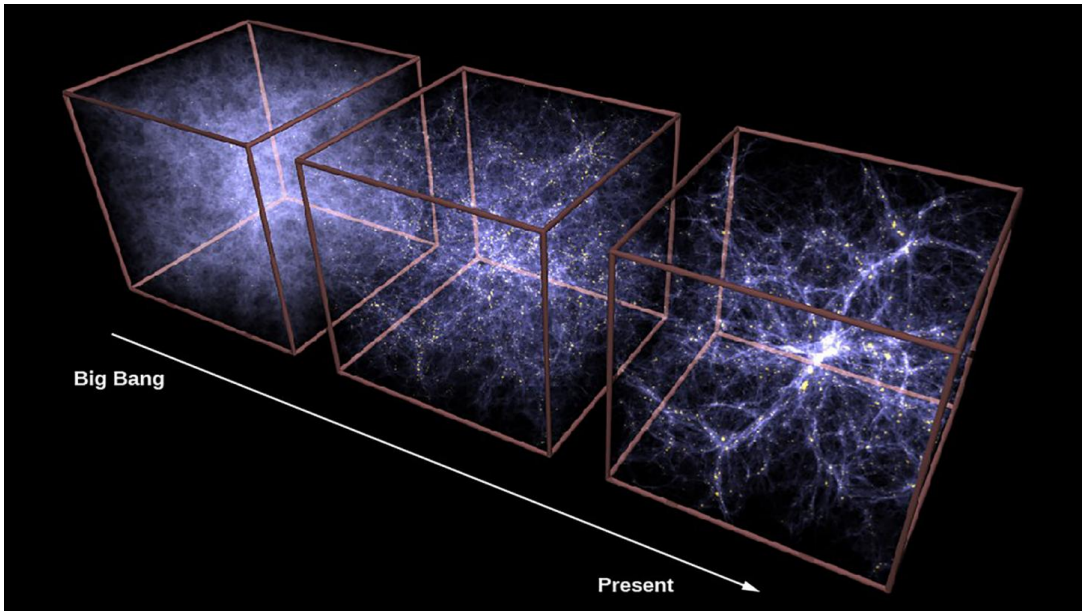

Figure 1.5: Simulation of large-scale structures in the Universe, illustrating the distribution of dark matter. The denser regions highlight the formation of dark matter filaments and halos, which are crucial for the development of galaxies and galaxy clusters. The hierarchical structure reflects the dominant role of gravity in the growth of primordial perturbations.

observations. These particles must be electrically neutral, either long-lived or stable, as their presence spans the entire history of the universe. Observations of galaxy clusters and structure formation suggest that DM has a small self-interaction cross-section and must not violate the observed baryon density constraints from Big Bang Nucleosynthesis (BBN) and the Cosmic Microwave Background (CMB), implying a non-baryonic nature.

Over the years, numerous models have been constructed to reproduce the observed DM abundance while respecting all known constraints. Some of these models rely on baryonic candidates, such as white dwarfs, neutron stars, black holes, or even lower-mass objects. Although these candidates could - in some cases - evade astronomical detection, they are generally ruled out by robust theories like BBN.

On the non-baryonic side, many models have been developed, often requiring physics beyond the Standard Model. These particle candidates are distinguished by their predicted mass and interaction cross-section, which are key parameters in both the theoretical models and the resulting experimental searches. In this context, candidates are sometimes represented in a mass-cross-section space, illustrating the vast range of possibilities (in Fig. 1.7 it is shown in the same plane the range detectable by different experiments): hypothetical masses extend from as low as 10^{-21} eV (e.g., fuzzy DM) up to 10^{27} eV (e.g., primordial black holes).

A good candidate for DM in the universe must satisfy several conditions. It must be massive enough to explain the observed mass deficit and the relic abundances. It must not interact electromagnetically or via strong interactions, as such interactions would likely have been detected by now; instead, it should interact primarily through gravity and, at most, weak interactions. Additionally, it must be stable or at least long-lived, as evidenced by its presence since shortly after the Big Bang, as confirmed by CMB observations, and its continued existence today.

An additional classification divides DM models into three categories: hot, warm, and cold Dark Matter. "Hot" DM refers to fast-moving particles, while "cold" DM refers to non-relativistic particles. Although the multitude of models covers all three cases, the cold Dark Matter (CDM) paradigm is most widely favored. CDM is preferred because it more effectively explains the formation of gravitationally-bound structures in the early universe, which, according to theory, arose through the gravitational amplification of small density perturbations.

To give a brief overview of leading candidates, they can be broadly categorized into particle-based models and alternative theories of gravity:

WIMPs Weakly Interacting Massive Particles are among the most studied candidates for Dark Matter. These hypothetical particles interact with normal matter predominantly through the weak nuclear force and gravity. Their mass is expected to be in the range of 10 GeV to several TeV, and they could have been thermally produced in the early universe. The relic abundance of WIMPs, calculated using standard cosmological models, coincides with the observed Dark Matter density, making them an attractive candidate.

Axions Axions are another leading candidate for Dark Matter, originally proposed to solve the strong CP problem in Quantum ChromoDynamics (QCD). These are light, pseudoscalar particles with masses ranging from microelectronvolts (μeV) to millielectronvolts (meV). Axions are predicted to be extremely weakly interacting, and if they exist, they could form a cold Dark Matter component that might be detectable through their conversion into photons in the presence of a magnetic field, an effect being explored by experiments like ADMX (Axion Dark Matter Experiment).

Sterile Neutrinos Sterile neutrinos are hypothetical particles that do not interact via the standard weak interactions but could mix with the three known types of neutrinos. They are another viable candidate for Dark Matter, particularly in the context of warm Dark Matter models, where they could help solve issues related to the formation of small-scale structures in the universe.

Modified Gravity Theories In contrast to the particle-based models, some theories propose modifications to Newtonian dynamics or General Relativity to account for

the effects attributed to Dark Matter. One such theory is Modified Newtonian Dynamics (MOND), which suggests a modification to Newton's laws at very low accelerations, potentially eliminating the need for Dark Matter. However, these theories face challenges in explaining the full range of cosmological and astrophysical observations.

1.4 Dark Matter detection

The quest to detect Dark Matter directly is ongoing, with experiments designed to observe the rare interactions of Dark Matter particles with ordinary matter.

In Fig. 1.6 are shown the three most used techniques for DM detection:

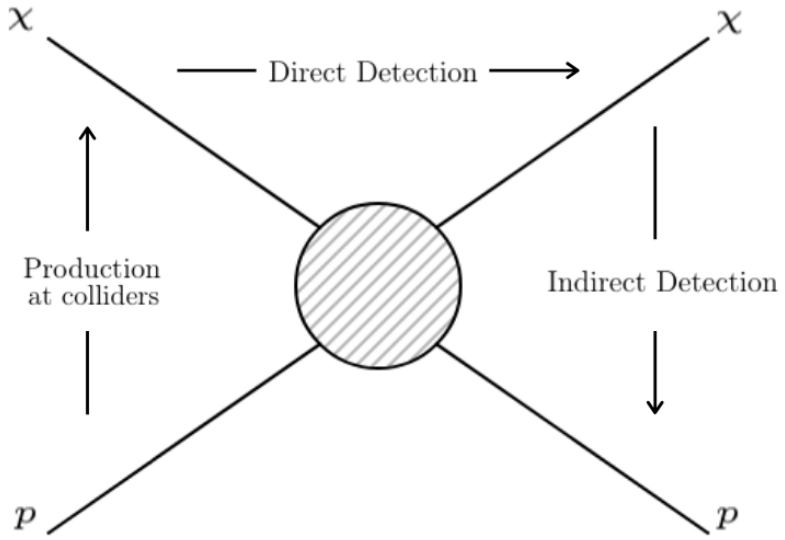

Figure 1.6: Schematic showing the couplings of a WIMP χ to ordinary matter p, with the corresponding detection technique. The annihilation of DM particles (downward arrow) would produce a pair of SM particles and this is exploited by the indirect detection technique. On the other hand, the collision of SM particles at colliders (upward arrow) could produce DM particles: their missing or unbalanced energy is usually searched. Finally, the elastic scattering of DM off nuclei (rightward arrow) is exploited in the direct detection technique.

Direct Detection Direct detection of Dark Matter involves searching for interactions between DM particles and Standard Model (SM) particles within Earth-based detectors. This method aims to detect the energy deposited when DM particles scatter off atomic nuclei or electrons. This energy can be converted into heat, light or

charge, and detectors are designed to be sensitive to these signals. Experiments are conducted in deep underground laboratories to minimize interference from cosmic rays and other sources of background radiation, such as gamma, beta and alpha radiation, as well as neutrinos. The interaction of DM with atomic nuclei is more likely than with electrons, especially for typical WIMP masses ranging $10 - 100$ GeV/c^2. This distinction helps differentiate DM signals from background noise. Various detection technologies are employed to distinguish between Nuclear Recoils (NR) and Electronic Recoils (ER), which is crucial for identifying genuine DM signals. A major challenge in these experiments is mitigating background noise from other sources, particularly neutrons and neutrinos. Neutrons can be particularly problematic as they can scatter off nuclei in a manner similar to DM particles, potentially leading to false positives. To address this, advanced detection systems incorporate Neutron Veto and multiple scatter identification techniques, as neutrons are more likely than DM particles to cause multiple scattering events. Neutrinos, on the other hand, present a unique and more difficult challenge. They can produce Nuclear Recoils via Coherent Elastic Neutrino-Nucleus Scattering (CEνNS), which is indistinguishable from the recoils expected from WIMP interactions. As DM detectors become more sensitive, they approach a sensitivity limit known as the "neutrino floor," where neutrino-induced events start to dominate the background, making it increasingly difficult to differentiate between signals from DM and those from neutrinos. Future detectors like DARWIN aim to operate at this level of sensitivity, requiring even more sophisticated methods to manage these backgrounds. Despite advanced technologies and rigorous methods, no experiment has definitively detected DM particle interactions. The DAMA/LIBRA experiment, which uses thallium-doped sodium iodide crystals, has reported a modulating signal that might be attributed to DM but this finding remains controversial and in tension with other experimental results. The field of direct detection is rapidly evolving, with future detectors like DARWIN expected to reach sensitivities that will probe the challenging region where neutrino interactions become a significant background, known as the "neutrino fog."

Indirect Detection Indirect detection seeks to observe the products of Dark Matter annihilations or decays. If WIMPs or other Dark Matter candidates can self-annihilate, they might produce detectable signals such as gamma rays, neutrinos or antimatter. Key experiments include space-based telescopes - like Fermi-LAT - and ground-based detectors - like the Pierre Auger Observatory, IceCube - and Imaging Air Cherenkov Telescopes (IACTs) such as MAGIC and VERITAS. Although some intriguing signals have been observed, none have been conclusively linked to Dark Matter: Fermi-LAT, for instance, detected a gamma-ray excess initially thought to be a DM signal but later attributed to other sources while neutrino telescopes like IceCube and Super-Kamiokande have set strict limits on DM interactions with

future improvements expected from upcoming facilities like Hyper-Kamiokande. These efforts collectively enhance our understanding of DM, despite the challenges of complex background signals.

Collider searches Particle colliders - such as the Large Hadron Collider (LHC) at CERN - play a crucial role in the search for DM, particularly Weakly Interacting Massive Particles (WIMPs). By producing high-energy collisions, the LHC allows experiments like ATLAS and CMS to detect potential DM particles indirectly through missing transverse momentum, suggesting the presence of neutral, stable particles. The key event type in these searches is Mono-X, characterized by a large missing momentum and a recoil object such as a jet or lepton. Additionally, the LHC explores DM through the search for "dark" mediators between standard model and DM particles. While these collider searches generally have lower sensitivity than direct and indirect detection methods, they provide essential complementary data, especially in the lower DM mass range, helping to refine and support other detection efforts.

1.5 Challenges and future directions

Despite the extensive evidence supporting the existence of Dark Matter, its exact nature remains one of the biggest unanswered questions in physics. The lack of direct detection has led to a broadening of the search to include lighter and less interacting particles, as well as reconsideration of alternative theories. Future experiments, such as the upgrade to the XENONnT experiment and next-generation detectors, aim to increase sensitivity by orders of magnitude, which could either detect Dark Matter or rule out large classes of models.

Moreover, advancements in computational astrophysics and cosmology are enabling more detailed simulations that might help distinguish between different DM models based on their effects on galaxy formation and evolution.

In conclusion, while the Dark Matter problem has driven significant progress in both theoretical and experimental physics, it remains an open field with much to discover. The integration of observational data, innovative detection techniques and new theoretical models will be crucial in unraveling this cosmic mystery. The current starting point for future searches is the plot in Fig. 1.7 which consists in the summa of past, present and future experiments limits.

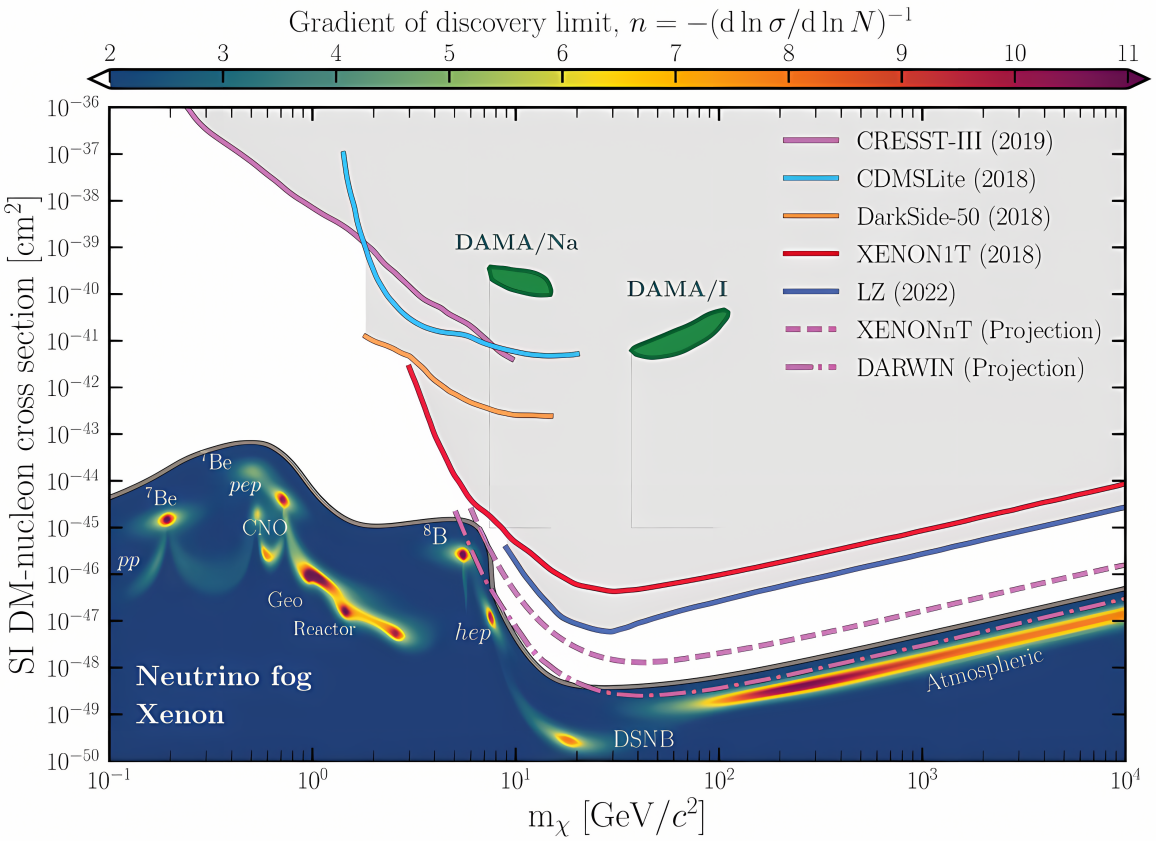

Figure 1.7: Exclusion limits on the Spin Independent (SI) DM-nucleon cross-section as a function of DM particle mass m_χ. One of the main features of this plot is the neutrino fog representation, as it is depicted as a function of the index n, present in the relation between the limit and the number of background events, as $\sigma \propto N^{-1/n}$. Here the neutrino fog is defined to be the region with $n > 2$: in this way, it is underlined that the $CE\nu NS$ is not a strict limit which makes the WIMP direct detection search impossible, but rather a background source that makes it more challenging.

Chapter 2

The XENONnT experiment

Chapter 2 focuses on the XENONnT experiment, one of the leading detectors in the search for Weakly Interacting Massive Particles (WIMPs). Section 2.1 provides a background on the XENON project, tracing its development from XENON10 to the current XENONnT phase. The details of the XENONnT detector are described in Section 2.2, with emphasis on key components such as the Time Projection Chamber (TPC), veto systems and the Gd-Water Purification System (GdWPS). Section 2.3 explains the operational principles of XENONnT and why liquid Xenon is an ideal medium for detecting rare events. Background rejection techniques are discussed in Section 2.4, focusing on how the system distinguishes between Electronic Recoil (ER) and Nuclear Recoil (NR) signals. Finally, Section 2.5 covers future advancements in XENONnT and its potential to make significant progress in Dark Matter detection.

2.1 The XENON project

Launched in 2005, the XENON program represents a series of pioneering experiments at the forefront of DM research. By utilizing Xenon-based dual-phase Time Projection Chambers (TPCs), these experiments have significantly enhanced the sensitivity in the direct detection of Weakly Interacting Massive Particles. The program is based at the INFN Laboratori Nazionali del Gran Sasso (LNGS) in Italy, a location that offers substantial shielding from cosmic radiation, making it ideal for such sensitive investigations. The progression of the program over the years can be seen in Figure 2.1, which illustrates the evolution in terms of size, active target mass, and the corresponding reduction in background levels.

The first experiment in the series, XENON10 [11], operated from 2005 to 2007 with an active Xenon mass of about 15 kg. This experiment marked a significant milestone in DM detection technology, demonstrating the long-term operational viability of Xenon-based TPCs. XENON10 established world-record upper limits on Spin-Independent (SI)

Figure 2.1: Overview of the XENON program detectors, showcasing the TPCs of varying dimensions and with the construction year noted. Displayed in blue are the active LXe masses within the TPCs. The orange indicator represents the low-energy (below 20 keV) ER background level measured in each experiment. Figure re-adapted from [10].

WIMP-nucleon cross-sections, achieving a minimum of $4.5 \times 10^{-44} cm^2$ [12] for a WIMP mass of 30 GeV/c^2, and also set limits on Spin-Dependent (SD) WIMP-neutron cross-sections, with a minimum of $5 \times 10^{-39} cm^2$ [13] at a 90% confidence level.

Following this success, the XENON100 experiment [14] was installed in 2008 with an increased target mass of 62 kg. It achieved a hundredfold reduction in background levels compared to XENON10, setting new upper limit records for the SI WIMP-nucleon cross-section at $1.1 \times 10^{-45} cm^2$ for a 50 GeV/c^2 WIMP mass. For SD WIMP-neutron and WIMP-proton cross-sections, the experiment set upper limits of $2.0 \times 10^{-45} cm^2$ and $3.5 \times 10^{-40} cm^2$ for 55 GeV/c^2 and 45 GeV/c^2 WIMP masses, respectively [15, 16]. These results marked a significant advancement in the search for DM.

The transition to ton-scale TPCs began with the launch of XENON1T [17] in 2016, which operated until the end of 2018. With a 2.0-tonne active target mass of Xenon, XENON1T pushed the boundaries of detection sensitivity, setting the most stringent limits yet on SI and SD WIMP-nucleon cross-sections, with a minimum at $4.1 \times 10^{-47} cm^2$ (SI) and $6.3 \times 10^{-42} cm^2$ (SD) for a 30 GeV/c^2 WIMP mass with 1.3 tonne-year exposure [18, 19]. These results not only solidified the XENON program's leadership in dark matter research but also broadened its scientific scope to explore new interaction channels

and rare physics events [20, 21, 22, 23].

In 2019, the program advanced to its fourth phase with XENONnT, which began data acquisition at the end of 2020. XENONnT is designed to increase sensitivity by an order of magnitude compared to its predecessors, further advancing the search for Dark Matter. Figure 2.2 shows the experiment setup in Hall B of LNGS.

Figure 2.2: A view of the XENONnT experiment located in hall B at LNGS. Prominently featured in the background is the water tank, serving both as a passive shield and an active water Cherenkov Muon and Neutron Veto. At the heart of the water tank, the TPC stands as depicted on the overlaying poster. In the foreground, the service building is visible, housing the various subsystems of the experiment including cryogenics, Xe purification, distillation, recovery, and the DAQ system.

2.2 Elements of XENONnT

The XENONnT experiment is situated in Hall B of the INFN LNGS. As the fourth phase of the XENON project, XENONnT benefits from the infrastructure of its predecessor, XENON1T, but incorporates significant upgrades to tackle the evolving challenges in DM research. XENON1T was specifically designed with its successor in mind, facilitating a rapid transition between the two experiments. The installation of XENONnT's detector systems was completed in 2020 in less than a year.

At the core of the XENONnT setup - depicted in Fig. 2.3 - is the Time Projection Chamber, positioned centrally. This is encased within a Neutron Veto (NV) detector, which features Gadolinium-loaded water to enhance the reduction of radiogenic neutron background. All components are housed in the same cylindrical stainless steel tank previously used for XENON1T. This tank is equipped with PhotoMultiplier Tubes (PMTs) and serves a dual purpose: acting as passive shielding against environmental radiation and functioning as an active water Cherenkov Muon Veto (MV).

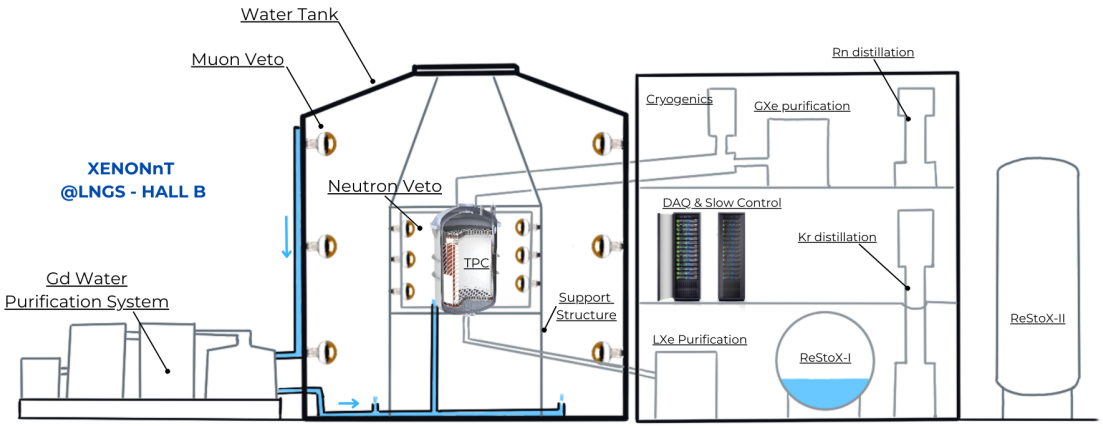

Figure 2.3: Schematic view of the XENONnT experiment and its main subsystems.

2.2.1 TPC and cryostat

At the core of XENONnT lies the TPC, now housed within a double-walled stainless-steel cryostat vessel, capable of holding a total of 8.6 tons of Xenon at approximately $-96°$C. Of this, 5.9 tons serve as the active detection medium inside the TPC, while the rest acts as a passive shield against external radiation sources. The top array is instrumented with 253 low-background 3-inch Hamamatsu R11410-21 PMTs, while the bottom array contains 241 PMTs of the same type, all selected for their low radioactivity and high efficiency in detecting Xenon scintillation light. The virtually cylindrical active region of the TPC is 1613 mm high and about 1327 mm wide, with about 4.5 tons allocated to the Fiducial Volume (FV).

The inner walls of the TPC are lined with Polytetrafluoroethylene (PTFE) panels to maximize ultraviolet (UV) photon reflection, enhancing the sensitivity of the detector. Five electrodes made of stainless-steel wires are employed to generate the necessary electric fields within the TPC. The cathode is placed at the bottom of the TPC, while the gate electrode hovers close to the liquid-gas interface, with the anode situated 3.0 mm above and 5.0 mm below this interface in the gaseous Xenon (GXe) phase. Additional perpendicular wires are integrated near the anode and gate to minimize sagging effects.

Two additional electrodes, the top screen and bottom screen, are positioned above the anode and below the cathode, respectively, to shield the PMTs from high electric fields.

This configuration allows for an efficient transition of electrons from the liquid to the gas phase, where they generate the S2 signal (see Section 2.3 for a deep discussion on S1 and S2 signals). The designed drift field was 191 V/cm, but during commissioning in November 2020, a short circuit between the cathode and the bottom screen electrode limited the cathode voltage, resulting in an average drift field of approximately 23 V/cm and an extraction field of about 2.9 kV/cm. Despite this limitation, these field strengths were sufficient to operate the TPC for scientific data collection.

During the TPC's construction, significant attention was given to material selection and cleanliness procedures to minimize background radiation. An extensive screening campaign was crucial in identifying the most radio-pure materials for use, employing techniques such as gamma-ray spectrometry and Inductively Coupled Plasma Mass Spectrometry (ICP-MS). The goal was to achieve a ^{222}Rn concentration of 1 μBq/kg, guiding both the selection of low Radon-emanating materials for all components in contact with Xenon and a meticulous cleaning campaign. A rendering of the TPC and the cryostat, including top and bottom arrays of PMTs and electrodes, is shown in Fig. 2.4.

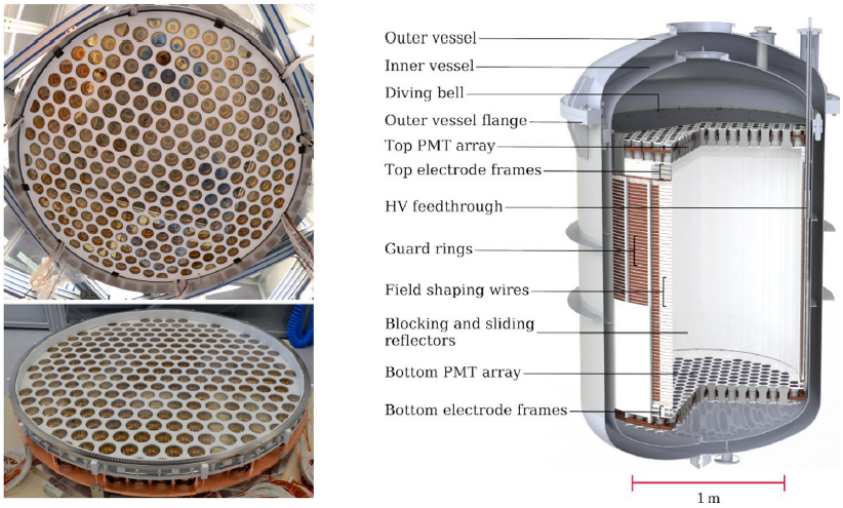

Figure 2.4: (Left) Pictures of the top and bottom PMT arrays taken during the assembly of the TPC. (Right) CAD rendering of the XENONnT TPC and cryostat from [24].

2.2.2 Veto systems

The XENONnT experiment employs two advanced veto systems (visible in Fig. 2.5), the *Muon Veto* (MV) and the *Neutron Veto* (NV), designed to significantly reduce background signals from muons and radiogenic neutrons, thereby enhancing the detection sensitivity for WIMPs.

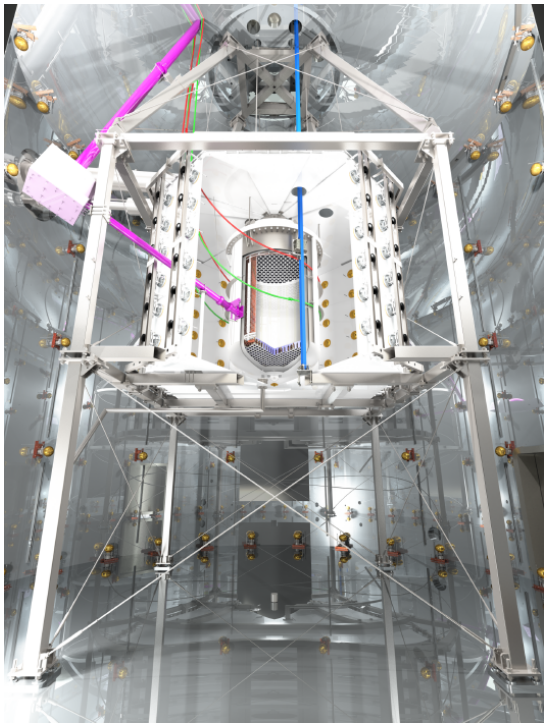

Figure 2.5: CAD rendering showing the various components inside the XENONnT water tank, including the central cryostat, the NV, the MV, and the calibration systems. In blue is the I-belt, used for moving the tungsten collimator. In purple, the L-shaped beam for neutron calibrations, and in red and green, the two U-tubes that embrace the cryostat.

The **Muon Veto**, inherited from XENON1T, is built around a water tank filled with ultrapure water and equipped with 84 Hamamatsu R5912ASSY 8-inch PMTs. It serves dual functions: providing passive shielding against radioactivity from the surrounding rock and actively vetoing cosmic muons. The MV system detects Cherenkov light emitted by muons traveling through the water, achieving a high tagging efficiency of 99.5% for muons and 70% for secondary particles.

The **Neutron Veto**, a significant upgrade introduced in XENONnT, is positioned between the cryostat and the MV, within the water tank. It is designed as a Gadolinium-doped water Cherenkov detector with an octagonal prism shape surrounding the cryostat. Instrumented with 120 8-inch Hamamatsu R5912-100-10 low-background PMTs, the NV detects Cherenkov photons and tags neutrons that scatter within the TPC by capturing them in water. Initially, with demineralized water, the NV achieves a neutron tagging efficiency of approximately 68%. At the end of 2023 NV water was doped with Gd-sulfate octa-hydrate (specifically $Gd_2(SO_4)_3 + 8H_2O$) and future operations plan to increase its quantity in the detector, which is expected to significantly increase the neutron capture

probability and boost the tagging efficiency to around 87% for the goal concentration of 5000 ppm of Gd salt. All the surfaces of the NV are covered with expanded PTFE (ePTFE) panels to enhance reflectivity, further improving the detection capabilities.

2.2.3 Xenon handling and purification

The larger Xenon volume required the development of advanced systems for Xenon handling and purification to achieve and maintain the necessary purity and low background levels. Key upgrades include the implementation of a novel liquid Xenon (LXe) purification plant and a Radon distillation column, both crucial for reducing Radon concentration within the Xenon target. The Xenon handling system is comprised of several critical components:

Cooling system The cooling and temperature control system in XENONnT is similar to that of XENON1T, utilizing a "remote cooling" concept with a vacuum-insulated cryogenic pipe linking the system to an external cooling station. Additionally, a battery-powered backup LN2 cooling system is in place to ensure stability during brief power outages.

Xenon storage and recovery The XENONnT cryogenic plant includes two storage units - ReStoX and ReStoX2 - designed to store the entire Xenon inventory. ReStoX, originally developed for XENON1T, has a capacity of 7.6 tonnes of Xenon, while ReStoX2 can hold up to 10 tonnes at room temperature. These units are essential for recovering Xenon in both liquid and gas phases, enabling rapid recovery during emergencies.

Electronegative impurity removal Removing electronegative impurities like O_2 and H_2O is crucial for maintaining the TPC's efficiency, as these impurities can reduce the number of electrons available for the charge signal during their drift (see again Section 2.3.2 for a deep discussion on signals in XENONnT). While the gas purification system from XENON1T was retained, XENONnT introduced a new LXe purification system. The effectiveness of these systems is measured by the electron lifetime, which has surpassed expectations, reaching up to 10 ms—compared to approximately 650 μs in XENON1T.

Krypton and Radon removal Krypton and Radon isotopes are significant sources of background radiation within the detector. The decay of ^{85}Kr through beta emission can contribute to the intrinsic background in the low-energy search region, while the emanation of ^{222}Rn from detector materials leads to a widespread distribution of its decay products throughout the LXe volume. To address these issues, XENONnT employs two additional systems: a *Krypton distillation column* and a *Radon distillation system*. The Krypton column, inherited from XENON1T, uses

cryogenic distillation to remove ^{85}Kr by exploiting differences in vapor pressures. The Radon removal system, integrated into the LXe recirculation loop, continuously distills both liquid and gaseous Xenon phases, effectively reducing the Radon concentration. This system has decreased the ER background - of which Radon is a major contributor - by a factor of approximately five.

2.2.4 Gd-Water Purification System (GdWPS)

The Cherenkov emission process produces a relatively low number of photons, which underscores the importance of two factors for Neutron Veto efficiency: the transparency of the water to UV and optical photons and the reflectivity of the detector walls. The latter is addressed by using highly reflective ePTFE panels while maintaining water transparency is equally crucial and necessitates continuous purification.

Until October 2023, the NV operated with demineralized water, utilizing the *Water Loop Plant* (WLP) inherited from XENON1T. The WLP's main function is to remove water-soluble ions and bacteria that can significantly reduce water transparency and, consequently, the detector's optical performance. Although the system is relatively simple, it includes a de-ionizing filter and sensors for monitoring pressure, temperature, flow, and resistivity, with the latter being a key indicator of water purity (demineralized water at 25°C typically has a resistivity of 18.18 MΩ·cm). The introduction of Gadolinium (Gd) into the water poses additional challenges, as the WLP, effective for purifying standard water, is unsuitable for Gd-water due to its potential to remove the valuable Gd ions.

Main goals of GdWPS

To address this issue, the Gadolinium-Water Purification System (GdWPS) has been developed. The GdWPS is designed with three primary objectives:

- Integration and dissolution: it ensures the successful integration and uniform dissolution of Gadolinium sulfate into the NV and, eventually, the MV water.
- Concentration maintenance: it achieves and consistently maintains the desired Gadolinium sulfate concentration. This involves not only reaching the target concentration but also continuous monitoring to ensure its stability over time.
- Preservation of optical properties: it purifies the solution to remove impurities that could negatively impact water transparency, thereby preserving the optical properties crucial for maintaining the detector's efficiency.

The design and operational strategy of the GdWPS are based on the model developed at the EGADS (Evaluating Gadolinium's Action on Detector Systems) facility, located in

the Kamioka mine. The EGADS facility [25, 26] successfully demonstrated that incorporating Gadolinium into the Super-Kamiokande (SK) detector was both safe and effective. This successful model provided the foundation for the development and implementation of the GdWPS for XENONnT.

Operating principles of GdWPS

The GdWPS is designed to manage and purify Gd-enriched water, ensuring optimal performance for the Neutron Veto and Muon Veto detectors. The system operates through several key processes and components, each crucial for maintaining water purity and Gadolinium concentration.

The operation of the GdWPS is summarized in Fig. 2.6: it begins with the dissolution of Gadolinium sulfate into water, creating a Gd-enriched solution which undergoes meticulous management to ensure uniform distribution and purity. A specialized filtration process separates the Gd-enriched solution from the Gd-depleted portion. This separation is achieved using high-efficiency filters designed to handle the specific requirements of the system.

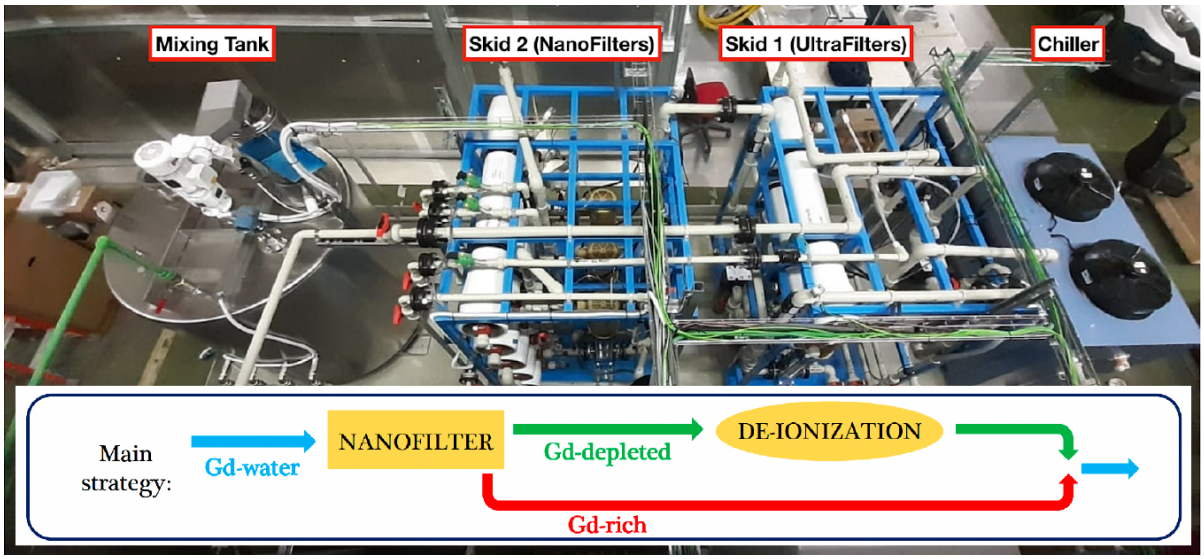

Figure 2.6: Illustration of the key steps in the GdWPS process: the dissolution and purification system for the Gd-water solution. A high-efficiency nano-filtration process separates the Gadolinium-enriched and Gadolinium-depleted portions. The Gadolinium-depleted solution is further purified through a standard ion purification system, removing impurities while minimizing Gadolinium loss. After purification, the two portions are reintegrated, ensuring a consistent solution, followed by a final filtration to remove residual impurities without affecting the Gadolinium concentration.

After separation, the Gadolinium-depleted portion of the solution is treated using

an ion purification system. This system removes impurities while minimizing the loss of Gd, which is critical for maintaining the system's effectiveness. Once the impurities are removed, the Gd-depleted solution is carefully reintegrated with the Gd-enriched portion to ensure a uniform and consistent solution. The final purification stage uses filters that do not absorb Gadolinium ions, allowing for the removal of residual impurities while preserving the Gadolinium sulfate concentration.

Components of GdWPS

The GdWPS consists of several essential components, each performing a specific function. All the components of the system are schematized in the Piping and Instrumentation Diagram (P&ID), reported in Fig. 2.7.

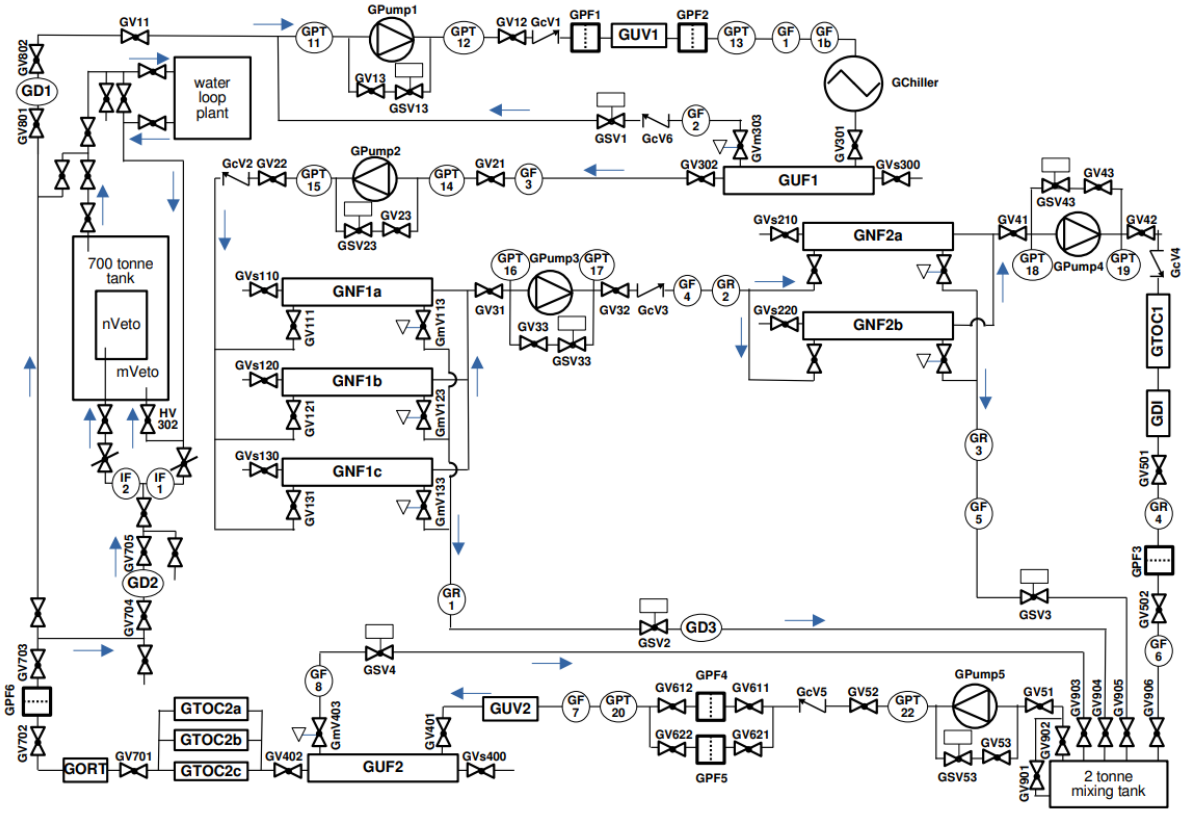

Figure 2.7: Piping and Instrumentation Diagram (P&ID) of the GdWPS. All the relevant circulation elements (such as pumps and valves), filters, and sensors are reported.

Circulation elements are crucial for the operation of the GdWPS. They include:

- **Pumps:** Five pumps work in series to circulate water from the 700 m^3 XENON tank through various filtration and sensor-equipped branches. The water flows to a

mixing tank, a 2-ton stainless-steel container where Gadolinium sulfate is dissolved. The water then returns to the XENON tank, creating a continuous purification loop at a flow rate of about 3 tons per hour. During the commissioning phase, the system uses a *bypass mode* that connects the output of the last pump back to the first. This internal loop allows for testing without affecting the detector's water quality.

- **Valves:** Manual and proportional solenoid valves regulate flow and pressure, isolate components for maintenance, and control pump intensity via a bypass line. Proportional solenoid valves are adjustable through the Slow Control system.

- **Chiller:** A dedicated chiller maintains the water temperature at around 12°C in the mixing tank, facilitating the dissolution of Gd.

Gadolinium insertion system is responsible for the introduction and dissolution of Gf sulfate:

- **Hopper:** Gadolinium sulfate is loaded into a specialized hopper at an external laboratory, sealed above ground, and transported to the underground laboratory.

- **Pneumatic transfer system:** The hopper is connected to a pneumatic transfer system that moves the salt to the mixing tank.

- **Stirrer:** A stirrer in the mixing tank ensures thorough mixing and dissolution of the Gd sulfate, essential for effective distribution and subsequent purification.

Purification elements are essential for the several filtration stages employed by GdWPS to target different types of impurities:

- **Static particle filters:** Remove particulate matter larger than 20 μm.

- **Ultrafilters:** Handle smaller particles and have a dual-output system. These filters direct impurities to a reject line while allowing purified water to pass through. Two ultrafilters are used, placed at the input and output lines.

- **Nanofilters:** Separate Gd-rich and Gd-depleted solutions. They operate similarly to ultrafilters but are designed to remove double-valence ions, including trivalent Gd ions. Five nanofiltration membranes are used - three in the first stage and two in the second stage - to progressively reduce Gadolinium concentration.

- **Resins:** De-Ionizing Resin (DI) is located in the product line of the second nanofiltration stage, it removes ionic impurities with minimal Gd loss; Organic Removal Tank (ORT) Resin is used to eliminate organic compounds without capturing Gadolinium ions, thus improving water transparency.

- **UV lamps:** Six UV lamps are used to prevent the growth of organic impurities, such as bacteria. They are strategically placed before the DI and ORT resins to ensure total Organic Carbon removal, although their use increases system temperature, necessitating cooling by the chiller.

Sensors with different characteristics are incorporated in the GdWPS to monitor and control system operations:

- **Manometers:** Installed before and after each pump and around particle filters to measure pressures and ensure proper functioning of the system. These readings help identify when filters need replacement due to saturation.
- **Flow rate meters:** Positioned in various branches to monitor water flow and calculate separation efficiency.
- **Density meters:** Measure Gd concentration based on the Coriolis effect, with placements in key branches to monitor density variations.
- **Conductivity meters:** Measure ion concentrations and water purity by applying an alternating voltage, with meters placed in lines before and after filtration stages.
- **Temperature sensors:** Integrated into density and conductivity sensors, these maintain optimal Gd dissolution temperatures. Additional thermometers monitor temperature in the mixing tank, where Gadolinium dissolution occurs.

The GdWPS ensures effective purification and management of Gd-enriched water, preserving optical properties and maintaining the system's performance.

Performance of GdWPS

The commissioning phase of the Gadolinium-Water Purification System has been successfully completed, confirming the system's readiness for the introduction of Gadolinium sulfate. This initial phase, conducted with pure water, allowed for thorough testing of all GdWPS components. Even in the absence of Gadolinium, the system effectively demonstrated its ability to purify water from various impurities.

From May 2022 to the end of the year, the GdWPS operated in alternating modes - either in bypass mode or connected to the XENON tank. This period was dedicated to extensive testing and adjustments in preparation for the first introduction of Gadolinium, which took place in January 2023. During this time, the XENON tank was also being purified using the Water Loop Plant. The initial connection of the GdWPS to the XENON tank occurred in July 2022. Subsequently, the optical properties of the Neutron Veto were monitored using specialized setups.

Throughout the latter half of 2022, the GdWPS alternated between being connected to the water tank and operating in bypass mode based on operational requirements.

When in bypass mode, the XENON tank continued to be purified by the WLP to maintain optimal optical performance. By the end of 2022, the system was fully prepared for the first Gadolinium salt insertion. During this stage, the plant was operated in bypass mode, and Gadolinium salt was added incrementally up to a total of 15 kg. Several measurements were taken to assess the system's response to this addition. With 15 kg of salt, the Gadolinium salt concentration in the system reached the target value of 0.5%.

The effectiveness of the GdWPS was evaluated using three distinct methods. The first method, an indirect measurement, involved conductivity readings and indicated a separation efficiency ϵ_{TOT} of 99.6%. The second method utilized Inductively Coupled Plasma-Mass Spectrometry for direct ion concentration measurements, resulting in a higher separation efficiency of 99.85%. Additionally, the Gadolinium salt loss rate was assessed after reconnecting the De-Ionizing resin, estimating a daily loss of approximately 600 g, corresponding to a separation efficiency of 99.68%.

Transparency measurements, conducted with a dedicated setup on samples from the plant, revealed significant improvements. The water transparency achieved by the GdWPS was nearly equivalent to that of demineralized water, with a transmittance difference of less than 0.5% compared to solutions prepared in the LNGS Chemistry Laboratory.

Having demonstrated its efficiency, the GdWPS is now engaged in purifying the Water Tank and is prepared for the introduction of high-concentration Gadolinium salt in anticipation of the upcoming Science Run of the experiment.

2.2.5 Calibration Systems

The calibration systems are pivotal for characterizing the responses of the TPC and outer detectors to various types of radiation, which is essential for determining the ER/NR bands, event positioning and energy reconstruction. These systems are categorized into two main types: internal and external calibration methods.

Internal calibration involves the direct injection of radionuclides into the Xenon target, allowing for a uniform distribution of the source and comprehensive characterization of the entire active volume of the TPC. This approach is applicable only to sources with sufficiently fast decay times. The key internal calibration sources used are:

- **^{83m}Kr:** Introduced via the Xenon re-circulation system, this metastable isotope decays into 32.2 keV and 9.4 keV conversion electrons, with a half-life of 1.83 hours. It is used to calibrate mono-energetic lines close to the WIMP search Region of Interest (ROI), defined by S1 between 0 PE and 100 PE and S2 between 126 PE and 12,58 PE (see Section 2.3.2). Regular calibrations with ^{83m}Kr are essential for monitoring the stability of light and charge yields, as well as the electron lifetime.

- **^{220}Rn:** Introduced from an electrodeposited ^{228}Th source, ^{220}Rn decays yield β, γ, and α particles. Its decay product, ^{212}Pb, provides a β spectrum useful for

characterizing the low-energy ER band. Due to its relatively longer half-life, ^{220}Rn is typically used at the beginning or end of scientific runs.

- **^{37}Ar:** This isotope emits X-rays at 0.27 keV and 2.8 keV and is employed to characterize the detector response near the low energy threshold. With a long half-life of 35 days, ^{37}Ar calibrations are conducted at the end of scientific runs, followed by removal through distillation.

External Calibration involves positioning sources outside the TPC, typically near the cryostat, to characterize specific regions of the TPC and the outer detectors. The main external calibration systems used in XENONnT are:

- **L-Shaped beam pipe:** This system provides collimated neutron beams (depicted in purple in Fig. 2.5) from a high-energy neutron generator. When used with D_2O, it allows for low-energy neutron calibration, essential for characterizing the NR band near the energy threshold.

- **I-Belt structure:** This structure (depicted in blue in Fig. 2.5) moves a tungsten collimator with an ^{88}Y-Be source along the cryostat, emitting low-energy neutrons and γ rays to aid in calibration.

- **U-Tubes**: Two independent stainless steel tubes (top and bottom) run around the cryostat at different heights (depicted in red and green in Fig. 2.5). They guide small external sources, such as Americium Beryllium (AmBe) and ^{232}Th, for characterizing the TPC and NV at various positions (see Section 3.4).

Additional calibrations are conducted weekly to assess the optical performance of the TPC and veto systems. Low-intensity LED light pulses are positioned near each PMT in the TPC, Muon Veto and Neutron Veto to monitor individual PMT performance, including gain, afterpulses and noise levels. In addition, diffuser balls and lasers are employed in the Muon Veto and Neutron Veto to evaluate the overall detector properties. The optical characteristics of the Neutron Veto are specifically measured using a dedicated system known as the Reflectivity Monitor (an example of this tool is presented in Fig. 4.13 and briefly discussed in Section 4.4.1).

2.2.6 Slow Control, DAQ and computing

To effectively monitor and control all subsystems, XENONnT employs a Slow Control (SC) system that integrates Programmable Automation Controllers (PACs) with industry-standard software (Cimplicity SCADA). This system has been enhanced to incorporate new components, including the LXe purification, Radon distillation column, ReStoX-2 Xenon storage, and the Neutron Veto along with its subsystems. The SC

system now supports advanced automated functions, such as managing cryogenics, adjusting PMT high voltage settings and performing optical calibration sequences. All the monitored parameters are stored and used to define alarm conditions and notify users of any anomalies.

In terms of data acquisition, the system handles signals from a total of 698 channels or PMTs distributed across the three sub-detectors: 494 PMTs in the TPC, 84 in the Muon Veto, and 120 in the NV. The data acquisition (DAQ) system operates with a quasi-triggerless approach, utilizing digitization thresholds to capture data. Signals from the PMTs are amplified, digitized and directed to a unified storage system. This setup ensures seamless integration of data from all detectors, which is then processed and formatted for analysis. The processed data is temporarily stored on local LNGS servers before being transferred to remote storage units in Europe and the USA, with a backup copy stored on tapes at CNAF in Italy.

2.3 Working principle of XENONnT

2.3.1 The reason behind Xenon

Xenon, particularly in its liquid phase, is a prime medium for DM detection and rare event searches due to its unique nuclear and chemical properties. The natural abundance of stable Xenon isotopes - ^{129}Xe, ^{131}Xe and ^{132}Xe - along with the presence of unstable isotopes like ^{124}Xe and ^{136}Xe (presented in Tab. 2.1), makes it an excellent candidate for DM experiments. Precisely, the lack of intrinsic radioactivity is one of the features that makes Xenon well-suited for rare events search. The high atomic mass of Xenon (A = 131) enhances the rate of spin-independent interactions, as the WIMP cross-section scales with A^2. Furthermore, Xenon's isotopes with non-zero spin, such as ^{129}Xe (spin $\frac{1}{2}$) and ^{131}Xe (spin $\frac{3}{2}$), are crucial for probing spin-dependent interactions.

^{A}Xe	Abundance (%)	Half-life	Decay-mode
^{124}Xe	0.095	1.8×10^{22} y	ECEC
^{126}Xe	0.089	stable	
^{128}Xe - ^{132}Xe	80.3	stable	
^{134}Xe	10.43	stable	
^{136}Xe	8.8	2.2×10^{21} y	$\beta\beta$

Table 2.1: Natural Xenon composition. Only two of the natural isotopes are unstable but with half-life greater than that of the universe: ^{124}Xe undergoes double Electron Capture (ECEC) while ^{136}Xe through a double-β decay. For the stable isotopes, $^{128,\dots,131}$Xe, the overall abundance is reported.

Xenon's high density (2.96 g/cm^3) in its liquid phase provides substantial self-shielding

against external backgrounds and its scintillation and ionization properties result in strong signal intensity. It remains in a liquid state at moderately cryogenic temperatures, with a triple point at 161 K, facilitating compact and scalable detector designs. When a particle interacts with a Xenon atom, it transfers energy, leading to ionization and excitation following the sketch in Fig. 2.8. This interaction produces Electronic Recoils and Nuclear Recoils, depending on whether the incident particle scatters off an electron or a nucleus. NRs typically produce shorter, denser energy tracks compared to ERs.

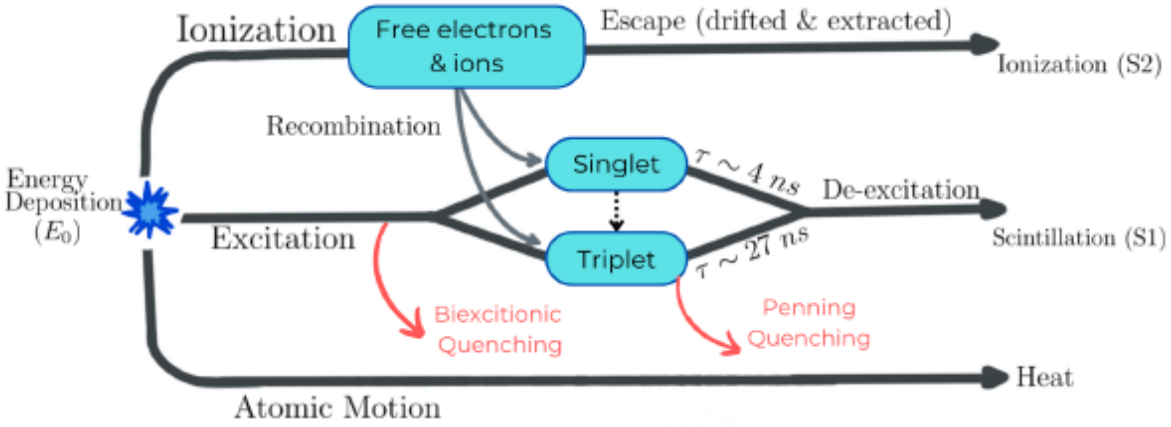

Figure 2.8: Energy depositions in LXe lead to the formation of observable scintillation and ionization signals, as well as to non-observable energy loss to heat. Atom excitation and ion-electron recombination form the prompt scintillation signal, referred to as S1. The ionization electrons are drifted and extracted by the application of electric fields, forming a proportional scintillation signal, S2. The dashed grey line depicts the process of superelastic collisions between electrons and singlet states, forming triplet molecular states. Schematic readapted from [27].

In experiments like XENONnT, detection relies on measuring scintillation and ionization signals generated by these energy deposits. Scintillation light is emitted in the ultraviolet spectrum as Xenon atoms and ions recombine and de-excite. For instance, an excited Xenon atom (Xe^*) undergoes scintillation, producing light ($h\nu$) through the following process:

$$Xe^* + Xe \rightarrow Xe_2^*$$
$$Xe_2^* \rightarrow 2Xe + h\nu$$

When ionization occurs, ionized Xenon atoms (Xe^+) are formed, and their subsequent

interactions lead to similar scintillation processes:

$$Xe^+ + Xe \rightarrow Xe_2^+$$
$$Xe_2^+ + e^- \rightarrow Xe^{**} + Xe$$
$$Xe^{**} \rightarrow Xe^* + heat$$
$$Xe^* + Xe + Xe \rightarrow Xe_2^* + Xe$$
$$Xe_2^* \rightarrow 2Xe + h\nu$$

Notably, LXe is transparent to its own scintillation light because the wavelength of emitted photons (around 178 nm [28]) is such that they are not absorbed by surrounding Xenon atoms, allowing effective photon detection with no necessity for wavelength shifters (contrary to Argon detectors). The scintillation light results from transitions between different energy states of Xenon excimers, with distinct decay times for the spin singlet (4 ns) and triplet (27 ns) states. The ratio between these states depends on the density distribution of deposited energy, which varies with particle type. While pulse-shape discrimination is possible in other noble gases like Argon due to more pronounced differences in decay times, in Xenon dual-phase TPCs this is challenging due to smaller differences in lifetimes relative to the time resolution of photosensors.

2.3.2 Dual-phase TPC of XENONnT

Double-phase Xenon Time Projection Chambers are the core technology behind experiments like XENONnT, which aims to detect Dark Matter interactions. These TPCs typically have a cylindrical shape, containing a target mass of liquid Xenon (LXe) with a thin layer of gaseous Xenon (GXe) on top, as illustrated in Fig. 2.9. The xy plane aligns with the cylinder's base, while the z axis runs parallel to the cylinder's axis, all housed within a cryostat that maintains a constant internal temperature for stable operation.

The dual-phase TPC operates by utilizing three main electrodes to create electrostatic fields in different regions of the detector:

- The **cathode** is placed at the bottom of the TPC and is kept at a negative voltage.
- The **gate** is situated near the liquid/gas interface and is set to ground voltage.
- The **anode** is located at the top of the TPC with a positive voltage.

These electrodes help apply two key electric fields: the drift field within the LXe volume, used to move electrons released after ionization towards the liquid/gas surface, and the extraction field within the GXe volume, used to extract these electrons into the gaseous phase where they generate proportional scintillation light (S2). Both fields must be as uniform as possible and are directed parallel to the z axis. Typically, the drift field is about 100 V/cm, while the extraction field is much stronger, around 10 kV/cm.

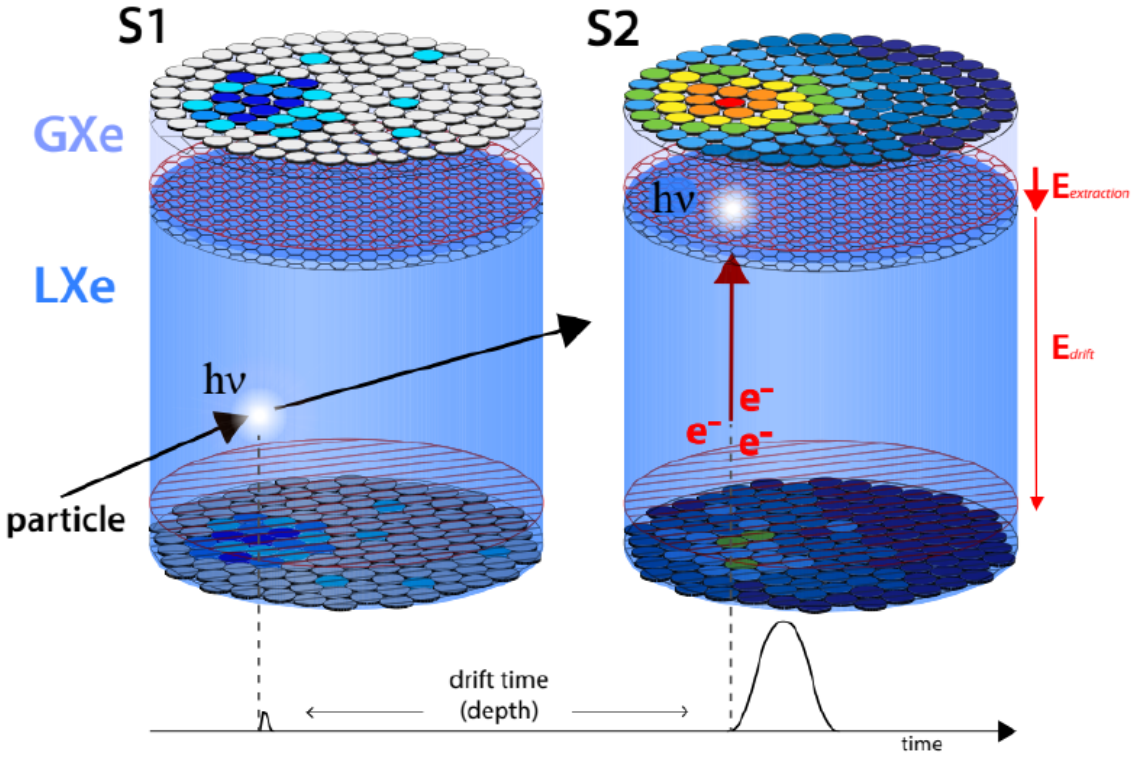

Figure 2.9: Schematic view of a particle interaction in a double-phase Xenon TPC [10]. After the prompt scintillation light produces the S1 signal, the electrons drift towards the liquid/gas interface and are extracted, producing S2. By the position distribution of the fired PMTs in the top array the XY position of the event is reconstructed. The third coordinate is related to the time delay between the two signals.

When a particle interacts with the Xenon target, it produces light and charge quanta. The first signal (S1) is generated by scintillation photons emitted isotropically when a recoil energy is released to the Xenon atoms. Simultaneously, the ionization process releases electrons, which drift towards the gaseous Xenon phase under the drift field. As these electrons approach the liquid-gas interface, the extraction field accelerates them into the gaseous phase, producing the second scintillation signal (S2). The top and bottom surfaces of the TPC are equipped with PMT arrays, which are essential for detecting these signals. The PMTs must be low-radioactive and sensitive to the Xenon scintillation wavelength, while the lateral surface is typically covered with highly reflective material like polytetrafluoroethylene (PTFE) to enhance signal collection efficiency.

The ability to detect both S1 and S2 signals is a distinctive advantage of dual-phase TPCs, enabling the detection of smaller charges and lowering the energy threshold of the detector. The distribution of the S2 signal in the top PMT array allows for estimation of

the xy position of the event, while the time delay between S1 and S2, given the constant and well-known drift velocity, helps infer the z position. Thus, the 3D position of the interaction can be fully reconstructed.

In XENONnT, this detailed signal detection and 3D event reconstruction are crucial. The ratio of the S1 and S2 signals plays a key role in distinguishing between ERs and NRs, which occupy distinct regions in the (S1, S2) parameter space as can be seen in Fig. 2.10. This distinction is critical for differentiating between potential DM signals and background events. The TPC can also distinguish between Single-Scatter (SS) and Multiple-Scatter (MS) events, which is essential for identifying true signal events versus background noise.

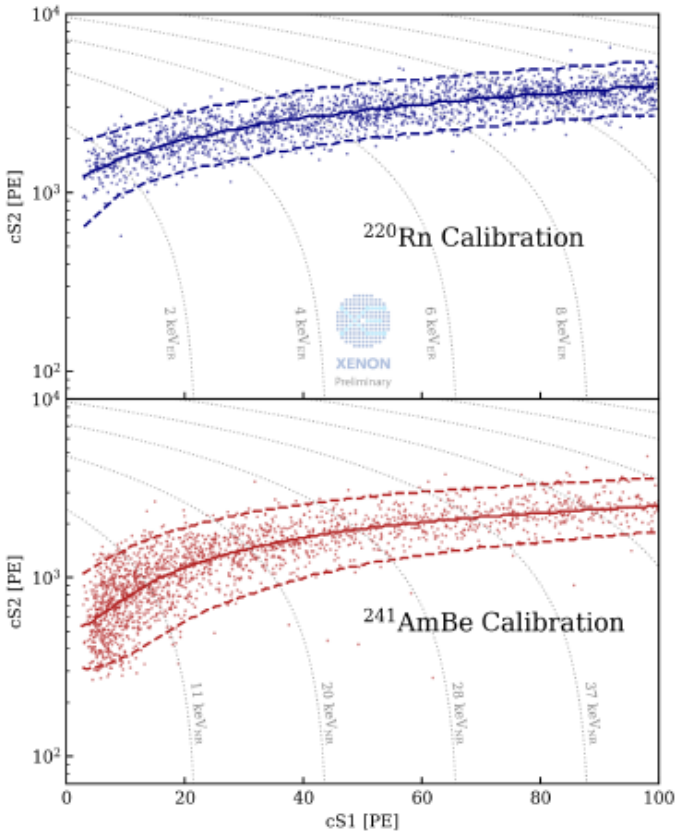

Figure 2.10: Determination of ER (top - blue) and NR (bottom - red) bands in the (cS1 area, cS2 area) parameter space in XENONnT [29]. The ^{220}Rn and ^{241}AmBe calibration data were used to identify the bands, whose median (solid line) and $\pm 2\sigma$ percentile are depicted for both types of interaction. The dotted grey lines in the plots show the respective ER and NR energies.

The corrected signals, referred to as cS1 and cS2, compensate for detector effects that

impact the number of light and charge quanta collected relative to those generated during the interaction. These effects are characterized by the g1 and g2 parameters, which are determined by analyzing the anti-correlation between S1 and S2 using various mono-energetic calibration sources. The energy deposited by an interaction is reconstructed using the equation:

$$E_{dep} = W \times \left(\frac{S1}{g1} + \frac{S2}{g2} \right) \tag{2.1}$$

where W represents the average energy required to produce either a scintillation photon or a ionized electron, and g1 and g2 are parameters obtained through calibration. While this formula is valid for ER events, in the case of NRs, one must consider the Lindhard factor, which accounts for signal quenching due to heat loss. The ability to distinguish between ER and NR events is quantified by the *ER-leakage parameter*, which depends on the energy and the applied drift field, with better separation achieved at higher drift fields due to the different recombination processes involved.

Overall, the TPC design in XENONnT allows for precise reconstruction of interaction vertices in three dimensions and the selection of events within a defined Fiducial Volume (FV), significantly reducing background interference and enhancing the sensitivity to potential DM interactions. This sophisticated detection mechanism underscores the importance of double-phase Xenon TPCs in the ongoing search for Dark Matter.

2.4 Background rejection in XENONnT

One of the most challenging aspects of a direct Dark Matter experiment is the need to detect an extremely rare signal amid a large number of background events. Understanding, simulating and reducing these background sources is therefore of paramount importance. The primary background sources for a WIMP direct search detector are summarized in Table 2.2, where they are categorized by radiation type, origin, interaction type and expected spatial distribution within the liquid Xenon (LXe) volume.

2.4.1 Electronic Recoil Background

The dangerous Electronic Recoil events appear to be the events that are not rejected by the ratio of S1 and S2, since they show up in the signal region and can mimic the expected WIMP signal. In this section, all the sources taken into account to model the ER component are presented:

Detector Components Radioactive decays within detector components contribute to the low-energy background through single Compton scatters. External gamma radiation produced by these components forms an almost flat spectrum at energies below 200 keV. In XENONnT, the cryostat vessels and PMTs are the primary contributors to this background (see Section 3.5 for the detailed analysis).

Type of radiation	Origin	Type of interaction	Spatial distribution
γ β	^{60}Co, ^{40}K, ^{137}Cs, ^{238}U and ^{232}Th decay chains from detector materials	Electronic recoil	Mostly outer layer
	^{136}Xe, ^{85}Kr and ^{222}Rn (decay chain) dissolved in LXe	Electronic recoil	Uniform
n	(α, n) and spontaneous fission from detector materials	Nuclear recoil	Mostly outer layer
	Induced by muons	Nuclear recoil	Mostly outer layer
ν	Solar	Electronic recoil	Uniform
	Solar, atmospheric and from Supernovae	Electronic recoil	Uniform

Table 2.2: Background sources of a typical Dark Matter experiment. They come from detector materials, intrinsic impurities, and external sources.

Radon ^{222}Rn emanation from detector materials is significant due to its 3.8 day half-life, leading to a uniform distribution within the LXe volume. The decay of ^{214}Pb, a product of the ^{222}Rn decay chain, significantly contributes to the ER background due to its beta decay. Despite strong efforts to reduce ^{222}Rn levels through careful material selection and the use of an online Radon distillation column, it remains the largest contribution to the total rate in the region of interest.

Krypton Traces of radioactive ^{85}Kr in the Xenon target contribute to the intrinsic background. ^{85}Kr undergoes beta decay, adding its signal to the low-energy region. Its concentration in the Xenon target is minimized through dedicated distillation.

Xenon Isotopes Unstable Xenon isotopes, such as ^{136}Xe and ^{127}Xe, add to the background through their decay processes. For instance, the decay of ^{124}Xe through double Electron Capture (ECEC), first observed in XENON1T, is a notable source of background specifically in the energy region of interest for WIMP searches. The contribution is estimated based on its measured half-life of 1.4×10^{22} years.

Solar Neutrinos Neutrinos produced mainly through pp fusion and electron capture by ^{7}Be interact with atomic electrons in the LXe target, leading to significant low-energy ER signals.

2.4.2 Nuclear Recoil Background

The Single Scatter Nuclear Recoil background is the most dangerous for the WIMP search, having the same signature expected from the WIMP interaction. Below are depicted the main sources of low energy NRs:

Radiogenic Neutrons Radiogenic neutrons in the MeV range are produced through Spontaneous Fission (SF) and (α, n) reactions in detector materials. For heavy nuclei, the high Coulomb barrier suppresses the (α, n) interaction, so neutron production is primarily due to SF. Notable contributions come from materials like stainless steel cryostat, PMTs, PTFE components and other materials close to the TPC, related to the ^{823}U/^{226}Ra and ^{232}Th/^{228}Th decay chains. These neutrons that interact in the active LXe are eventually captured in the NV volume, leading to a reduction in the estimated rate.

Cosmogenic Neutrons Induced by cosmic muons interacting with surrounding rock and concrete, cosmogenic neutrons are tagged using the active MV in the water tank. Although the rate of cosmogenic neutrons in the WIMP search region is negligible, it can be substantially suppressed thanks to the Neutron Veto system.

CEνNS Coherent Elastic Neutrino - Nucleus Scattering due to solar, atmospheric and diffuse supernova neutrinos contributes to the NR background. Solar neutrinos affect sensitivity to lighter WIMPs, while atmospheric and diffuse supernova neutrinos extend to higher energies. The expected rate of CEνNS is calculated by considering solar neutrinos ($^8B + hep$) and the sum of atmospheric and diffuse supernova neutrinos.

Double-phase time projection chambers are adept at distinguishing ER events from NR events. When an electron or nucleus scatters, the kinetic energy gained is partially released via scintillation light and partially through ionization of the Xenon atoms. Some of the electron-ion pairs formed recombine, emitting scintillation photons that contribute to the S1 signal. Electrons that do not recombine are drifted by an electric field, producing the S2 signal. Given the higher Linear Energy Transfer (LET) of nuclei, they travel shorter distances in LXe, increasing the likelihood of recombination and resulting in a lower S2/S1 ratio for NR events. This ratio is often used for ER/NR discrimination, with ER and NR events forming distinct bands in the (cS1, cS2) space (as already depicted in Fig. 2.10).

Background events originating from detector materials can also be isolated based on their spatial location within the liquid volume, as they tend to scatter near the TPC surfaces. Thanks to the 3D position reconstruction capabilities of double-phase TPCs, an internal fiducial volume can be defined where material and environmental backgrounds are suppressed. Events occurring outside this fiducial volume are excluded from WIMP searches.

Some background sources cannot be mitigated by fiducialization alone. Small quantities of impurities dissolved in Xenon, such as Krypton and Radon, can produce events uniformly distributed across the TPC. Isotopes like ^{85}Kr and ^{222}Ra contribute to the ER background, while ^{222}Ra's decay products like ^{214}Pb can leak into the NR band due to statistical fluctuations. These backgrounds must be minimized through dedicated purification systems, such as cryogenic distillation, which removes unwanted noble gas traces from the LXe and GXe.

In deep underground laboratories, the flux of muons produced by cosmic rays, while significantly lower than at the surface, is not negligible. Although muons release much more energy than WIMPs and thus do not pose a direct threat to DM searches, they can lead to secondary emissions like neutrons. Neutrons are particularly dangerous because their interactions can mimic WIMP ones. They originate from muon-induced processes like spallation or from spontaneous fission and (α, n) reactions in detector materials. Neutrons are neutral and massive, producing NR events that are more likely to occur near the detector surfaces. Neutron background can only be partially mitigated by fiducial volume cuts and not by the $\log_{10}(S2/S1)$ discrimination method. Another way to reduce neutron background is by distinguishing between SS and MS events, as WIMPs are expected to interact only once in the TPC. MS events, characterized by a single S1 and two S2 signals, can be excluded to reduce neutron background. Additionally, a dedicated Neutron Veto system, such as the one built for XENONnT, can significantly reduce neutron background by tagging neutrons.

Neutrinos from various sources also contribute to the background for DM searches. Due to their extremely low interaction cross-section, neutrino interactions are uniformly distributed within the target. Solar neutrinos, primarily from the pp chain, interact mostly with LXe electrons, allowing for ER rejection. However, higher-energy solar neutrinos, such as those from ^{8}B decay, along with atmospheric and Diffuse Supernova Neutrinos (DSN), can scatter off nuclei producing NR events. This interaction, known as Coherent Elastic Neutrino-Nucleus Scattering (CEνNS), was only recently observed by the COHERENT collaboration. As DM detection experiments reach higher sensitivities, they will begin exploring regions of WIMP interaction cross-sections where the irreducible CEνNS background will dominate, leading to a decline in sensitivity for WIMP discovery. This phenomenon is known as the neutrino floor, or more optimistically, the *neutrino fog*.

2.5 Future prospects in LXe-based DM research

The advancements in ultra-low background LXe detectors, particularly with XENON1T, have opened up exciting new possibilities beyond Dark Matter research, including the exploration of rare processes such as double electron capture decays and CEνNS. Current-generation experiments like XENONnT and LZ have significantly enhanced sensitivities

across these research areas. However, they have yet to overcome the *neutrino fog* limit in the spin-independent WIMP scattering parameter space (visible in Fig. 1.7). This limitation sets the stage for an even more ambitious endeavor - the XLZD observatory, with the merging of the leading collaborations in the current scenario (XENON and LZ) plus the future DARWIN experiment [30].

XLZD [31] is envisioned as a 60-ton LXe active mass detector, designed to be the ultimate tool in DM detection, capable of pushing the boundaries to reach the neutrino fog. Its design allows for a comprehensive search for neutrinoless double-beta decay, leveraging the natural abundance of ^{136}Xe. Additionally, XLZD will refine measurements of the solar pp neutrino flux and extend its reach to other searches beyond the Standard Model, positioning it as a leading force in the next decade of particle physics exploration.

However, such an ambitious project presents significant challenges, primarily due to its scale. It will require vast quantities of purified Xenon, a suitably large underground laboratory, and novel materials and techniques for efficient operation. Managing electrical fields within such large-scale time projection chambers poses additional challenges, including electrode sagging and the need for detector construction materials that are both structurally robust and extremely low in radioactive contaminants. The use of traditional PMTs could significantly increase background levels and raise concerns about long-term stability under cryogenic conditions. Alternatives like Silicon Photomultipliers (SiPMs) offer advantages due to their lower radioactivity levels and compact size, making them a viable option for large-scale applications.

Despite these challenges, XLZD represents a quantum leap in DM detection and rare event searches, marking a transition to the next generation of LXe detectors and setting a new standard for future research in particle physics.

Chapter 3

Montecarlo simulations of the Neutron Veto

Montecarlo (MC) simulations play a crucial role in understanding the detector's response to physical interactions, allowing for predictions and modeling of the expected experimental backgrounds and performance. The XENONnT detector is fully simulated using the GEANT4 toolkit [32], as described in Section 3.1, with the MC framework built upon the simulation package originally developed for XENON1T [33]. In particular, a detailed description of the Neutron Veto modelization can be found in Section 3.2. All relevant physical processes are simulated using GEANT4, from the neutron emission up to the production and detection of Cherenkov photons from neutron or gamma interactions in water or other detector materials. A custom package, the "NV Hitlet Simulator" (see Section 3.2.1), is used to simulate the response of the PMTs to impinging photons. This tool is able to generate low-level signal information identical to that of real data, thus allowing the application of the same data analysis chain to both real and simulated Neutron Veto data. Optical properties of the Neutron Veto and Gd de-exitation models are discussed in Sections 3.2.2 and 3.2.3, while in Section 3.2.4 some examples of neutron capture patterns are presented. As mentioned, the Hitlet Simulator is an efficient event simulator developed to complement the Neutron Veto MC simulations and is deeply described in Section 3.3. The simulations of the AmBe neutron source, used for Neutron Veto calibration, as well as the simulations of radiogenic neutron backgrounds, are discussed in Sections 3.4 and 3.5, respectively.

3.1 A unique simulation framework for XENONnT

GEANT4 [34, 35] is an open-source toolkit developed at CERN for simulating the passage of particles through matter, used in various fields such as high-energy physics, medical physics, space sciences and radiation protection. This software is designed to accurately

simulate particle interactions with materials, tracking their transport step by step. During this process, GEANT4 takes into account all possible interactions, such as energy loss, scattering, and interactions with electromagnetic fields. The transport of a particle ends when it runs out of kinetic energy, disappears as a result of an interaction, or reaches the outer boundary of the simulation, which represents the laboratory or physical world volume. A central feature of the toolkit is the ability to access the transportation process at different stages, providing detailed information to the user. Data can be retrieved at the beginning and end of transport, at the end of each intermediate step, or when a particle reaches a sensitive detector. These capabilities make GEANT4 a versatile tool for studying complex physical phenomena.

Particle interactions within the XENONnT detector are studied by simulating their generation and propagation through the various detector volumes. Energy deposits in the time projection chamber are translated into S1 and S2 signals, which are used to assess the expected background and signal distributions in the observable data space. This signal conversion is based on a model of light and charge emission following particle interactions in LXe, incorporating detector effects such as signal collection efficiency and reconstruction.

For particle generation and propagation, GEANT4 version *10.3-patch03* is employed in the XENONnT simulations. Radioactive decays are taken into careful consideration due to their importance for the background computation: they are handled through the *G4RadioactiveDecay* process, and if the decay produces an isomer its prompt de-excitation is managed by the *G4PhotonEvaporation* process. Parameters such as half-lives, nuclear level structures, decay branching ratios and energy levels are sourced from the Evaluated Nuclear Structure Data Files (ENSDF). To ensure precise tracking of gamma and electron interactions, the *Livermore* physics list is used. Neutron interactions at low energies (below 20 MeV) are modeled with high precision using the *QGSP_BERT_HP* hadronic physics list, which incorporates data-driven models from the *G4NDL4.5* neutron library with thermal cross-sections.

Additionally, the default GEANT4 modeling of gamma emission following neutron capture by Gadolinium is replaced with a data-driven model (see Section 3.2.3), correcting for both energy conservation during de-excitation and the gamma multiplicity of the cascade. However, the default models for neutron capture by other nuclei remain unchanged. Cherenkov photon generation following neutron-induced signals is also included in the simulations, tracking the process from neutron generation and recoil in the active detector volume through to the detection of these photons by the Neutron Veto PMTs.

The general idea is connecting all subdetectors in a unique simulation framework to produce a complete and consistent simulation of the entire experiment in all its constituent parts.

3.2 The Neutron Veto model in GEANT4

In the XENONnT experiment, the NV system is modeled in GEANT4 to simulate the detection of neutrons accurately. The NV system consists of several reflectors and PMTs, designed to detect Cherenkov photons produced by neutron interactions in water. Below a detailed description of the NV model as implemented in GEANT4 is provided which refers to the parts depicted in Fig. 3.1.

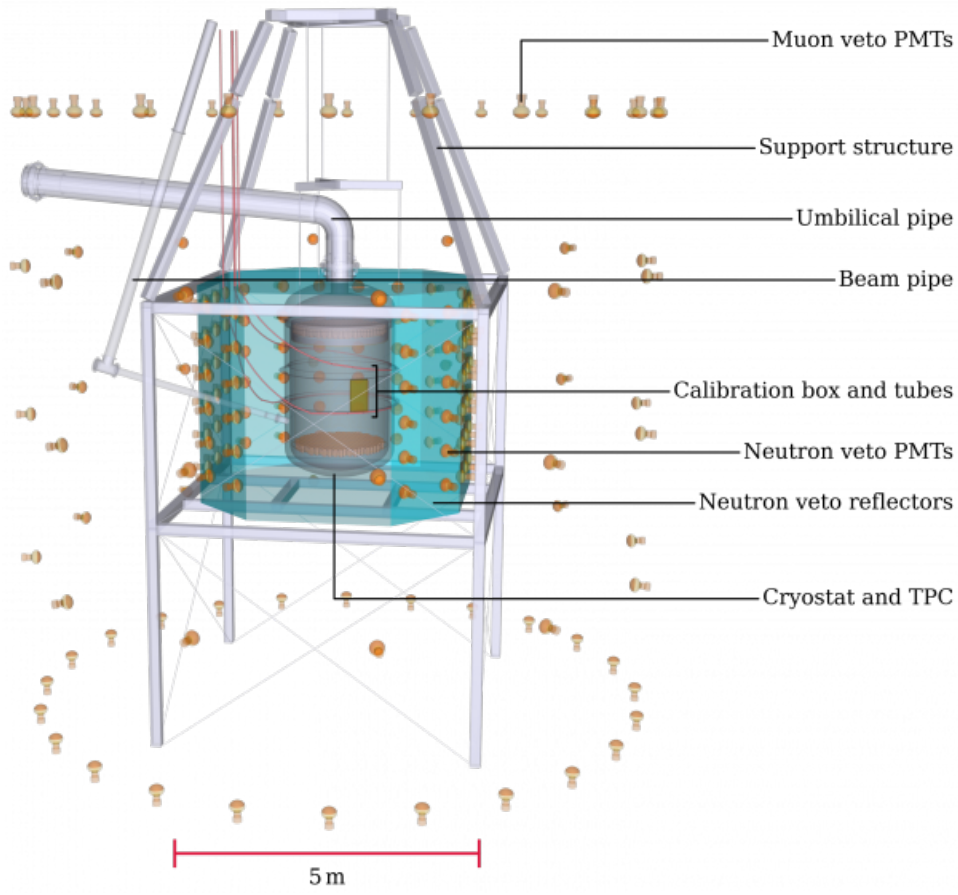

Figure 3.1: GEANT4 rendering of the three-layered detector setup, including the Muon and Neutron Veto systems. For clarity, the water tank walls, responsible for housing the MV PMTs, the Neutron Veto support framework, and various other components (such as calibration devices) are not shown in the picture. The reflective panels, which optically isolate the MV and NV regions, are displayed as translucent turquoise surfaces. The PMT windows of the NV are positioned to face its detection area through dedicated openings in the panels.

3.2.1 Detector geometry and materials

The NV system is housed within a 700-tonne water tank surrounding the cryostat that contains the TPC. The NV forms an octagonal prism standing 3.16 m in height and enclosing a $\sim$ 40 m^3 volume, of which $\sim$ 34 m^3 of water. The octagonal design consists of sides with two different widths: the wider sides measure 2.02 m, while the narrower ones are 1.22 m. This design is based on key factors such as optimizing neutron detection efficiency, minimizing background contributions from NV materials (informed by MC simulations), and addressing practical installation constraints, including interference from the calibration system components and cryostat pipes.

The lateral walls of the NV (shown in Fig. 3.2a) are constructed from 24 rectangular panels (depicted in Fig. 3.2b) made of expanded polytetrafluoroethylene (ePTFE), which offers superior reflectivity, exceeding 99% for wavelengths above 300 nm. These panels, with a thickness of 1.5 mm, are mounted using plastic frames attached to thin stainless steel bars anchored to the cryostat support structure. The ePTFE reflectors define the NV volume around the cryostat and are crucial for enhancing light collection. Additionally, ePTFE foils cover the entire surface of the cryostat, further boosting the system's reflectivity and efficiency. The octagonal shape of the NV is supported by a stainless steel structure divided into four quarters, with beams supporting a ring around the cryostat's central pipe, providing anchorage for the upper reflectors.

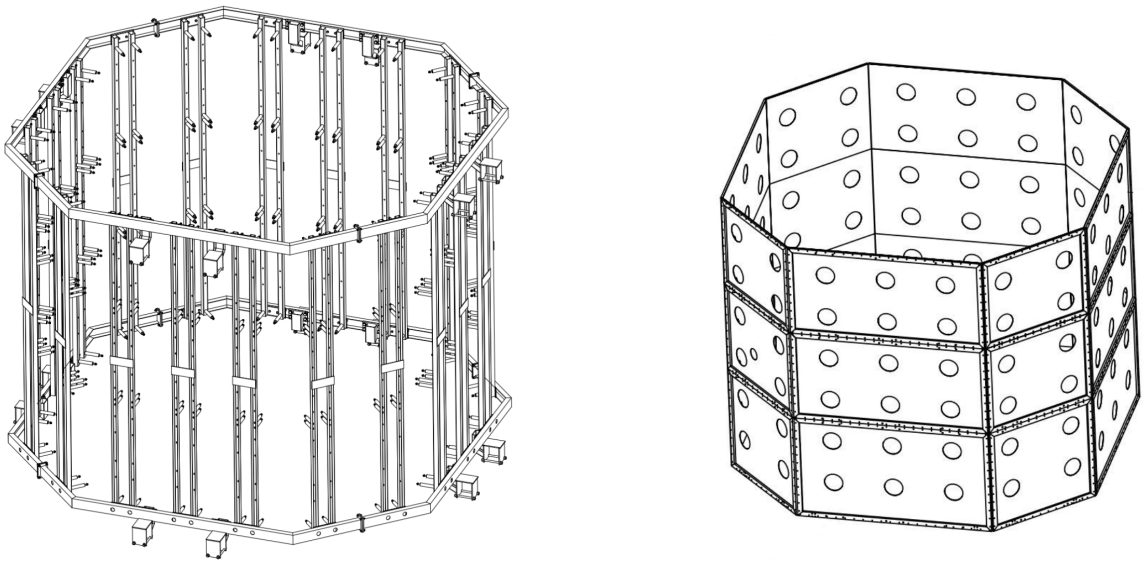

(a) (b)

Figure 3.2: (a) Technical drawing of the NV support structure, showcasing also design of the supports for the reflective panels. (b) Technical drawing of the ePTFE panel assembly constituting the reflective surface of the NV.

The floor of the NV (in Fig. 3.3a) consists of trapezoidal panels and two free reflective sheets, positioned 26 cm below the cryostat's bottom dome. The ceiling (shown in Fig. 3.3b), inclined at a 5-degree angle towards the center, is similarly constructed from trapezoidal panels and free reflective sheets, with holes and hinges to accommodate calibration elements and cryostat pipes. These reflective sheets also feature openings for the insertion of neutron generators and other equipment. These openings are the only locations where photons can travel between the Neutron Veto and the outer Muon Veto volume.

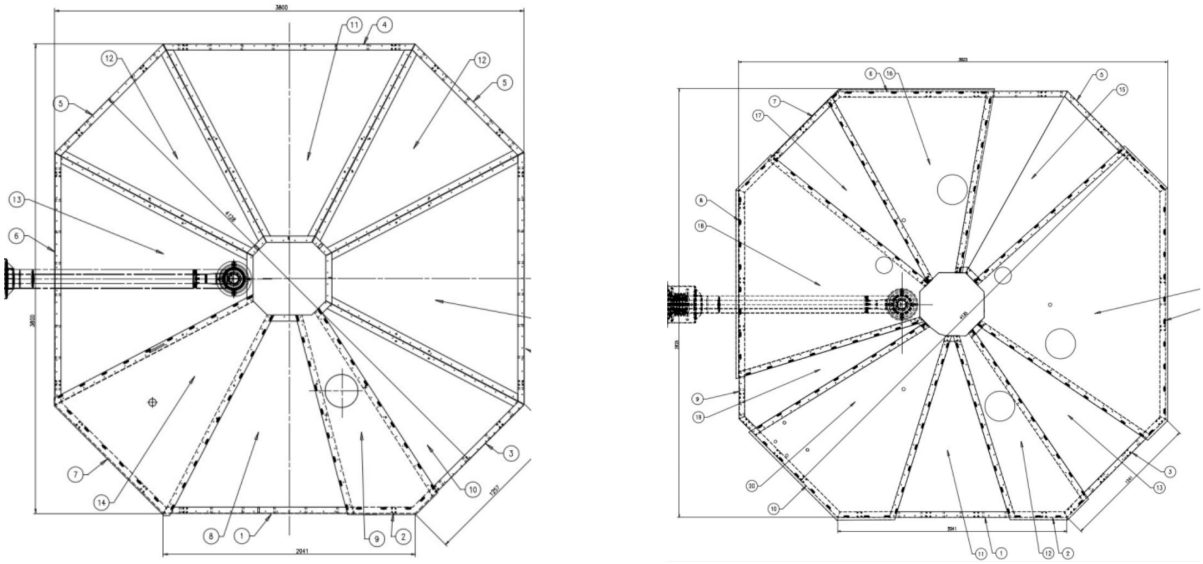

(a) (b)

Figure 3.3: Technical drawing of the ePTFE panels composing the NV floor (a) and ceiling (b).

The GEANT4 model of the NV system closely mirrors the physical setup and includes the reflectors, PMTs and structural elements, with necessary simplifications for computational efficiency. For instance, while the real top reflector has a 5-degree upward inclination, in the model it is represented as a flat, horizontal surface to reduce simulation complexity. The lateral reflectors, derived from CAD drawings, account for the thickness of the bottom reflector's frame by adding 20 mm to their height. The bottom reflector, modeled as a 1.5 mm thick horizontal octagon, directly supports the lateral reflectors, playing a key role in reflecting light towards the PMTs.

NV PMTs modelization

The NV PMTs are 120 high quantum efficiency (QE) and low-radioactivity 8-inch Hamamatsu PMTs (R5912-100-10 WA-D30-SEL-Assy). These PMTs are arranged in 20

columns, with 6 PMTs per column, spaced vertically by approximately 45 cm. The wide and narrow panels accommodate three and two PMT columns, respectively. The PMTs are mounted externally to the NV, with only their glass windows extending into the NV volume: this arrangement minimizes radioactive background contributions from the PMTs themselves.

The realistic PMT geometry (in Fig. 3.4) is incorporated using the *G4UnionSolid* feature in GEANT4 to model the head and body of the PMTs accurately, while simpler methods are employed for the internal parts to avoid performance degradation.

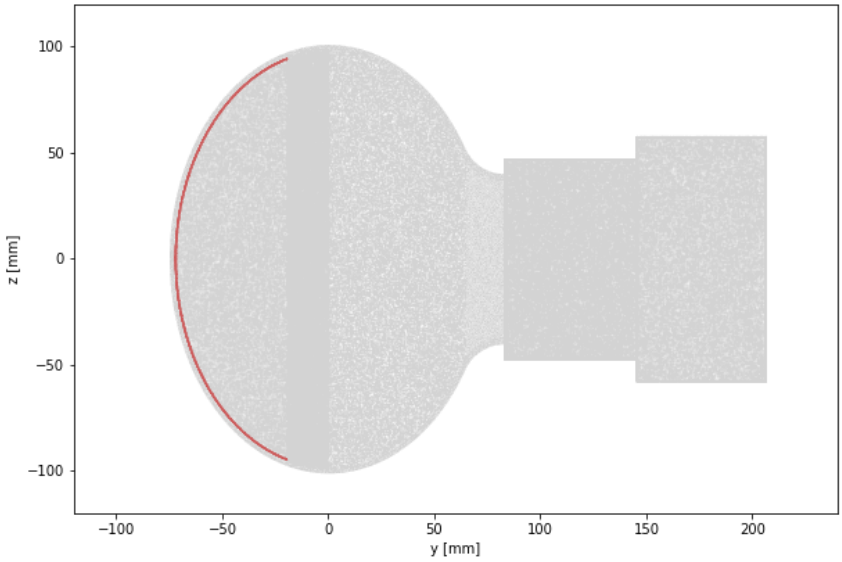

Figure 3.4: Rendering of a NV PMT, as reproduced in GEANT4. The red line highlights the photocathode of the PMT.

3.2.2 Optical properties

The Neutron Veto system in the XENONnT experiment has been extensively modeled in GEANT4, with a focus on accurately simulating its optical properties to ensure the reliable detection of Cherenkov photons produced by neutron interactions. The optical inputs for key NV components, such as water and ePTFE reflectors are critical for this simulation, influencing how photons are absorbed, reflected, and transmitted within the system.

Water absorption length

The absorption length of pure water is modeled using parameters from the Super-Kamiokande (SK) calibration [36], which includes data on refractive index, absorption length, and Rayleigh scattering length across an energy range of 1.57 - 5.03 eV. The same spectral shape of absorption length is currently kept also to model the Gadolinium-doped water as the observed NV data are well matched by tuning a global effective light collection parameter for different Gd concentrations (see Section 3.3).

The Super-Kamiokande model for the water absorption length is shown in Fig. 3.5, together with the default GEANT4 model and the measurement from the EGADS experiment [37] on Gd-water at 0.2% concentration of Gd mass. In the near future, a specific absorption length model will be derived from transparency measurements on both pure-water and Gd-water samples taken from the XENONnT water tank to improve the accuracy.

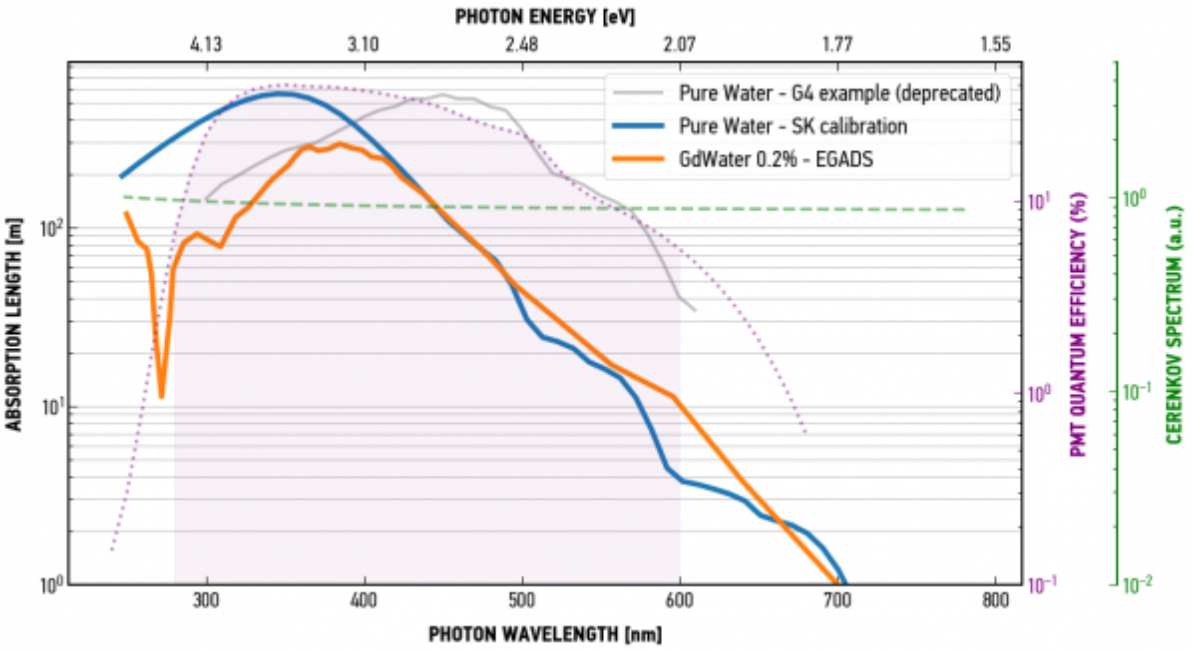

Figure 3.5: Water absorption length models considered for the XENONnT Neutron Veto simulation. The SK calibration model (blue) is currently used. A typical QE spectrum from a NV PMT number is shown as a dashed purple line. The purple shaded region indicates where $QE > 10\%$.

ePTFE reflectivity

The reflectivity of ePTFE, the material used in the reflective panels of the NV, is an essential parameter for maximizing the Cherenkov photon detection efficiency. A dedicated measurement reported a reflectivity of 99.35%, a value that can be adjusted via a preinit macro in the GEANT4 code. This high reflectivity ensures that most photons are reflected toward the PMTs, enhancing overall detection rates.

Stainless steel reflectivity

A small fraction of exposed surfaces inside the NV is made of Stainless Steel (SS) components - such as the cryostat flange, U tubes and ports on the cryostat top dome. The reflectivity of SS components is less well characterized. Tentative values for stainless steel reflectivity are set at 50%, but these values are based on surface roughness from drawings rather than direct measurements. Discussions have revealed that the surface roughness of the cryostat flange is approximately 0.8 μm. Studies on polished stainless steel suggest that surface roughness can influence reflectance, as outlined in research paper [38] on stainless steel properties. Reflectance measurements for components like the U-tubes and I-Belt are pending.

PMT photocathode

Currently, the PMT photocathodes are modeled as fully opaque surfaces. Photons hitting the photocathode are absorbed and recorded. However, the complete modelization of the PMT photocathode's reflectivity is under consideration pending dedicated measurements on the specific NV PMT model.

NV time constant model

The photon collection efficiency at the NV PMTs can be characterized by a time constant (τ), which describes the time distribution of photon arrivals. This model, developed in [39], accounts for various factors influencing photon absorption such as the water absorption length, the reflectivity of ePTFE and the geometry of the system. The time constant model is described mathematically as:

$$\tau(T, R) = \left[\frac{v}{T l_0} + k_w(1 - R) + \frac{1}{\tau_{geom}} \right]^{-1}, \tag{3.1}$$

where l_0 is the nominal water absorption length based on the Super-Kamiokande model, T is a scaling factor for the water absorption length, R represents the reflectivity of the ePTFE, k_w corresponds to the probability of a photon hitting a ePTFE surface (estimated at $k_w = 0.13$ ns^{-1}), v is the speed of light in water ($v = \mathrm{c}/1.33$) and τ_{geom} stands for the

contribution to photon absorption from non-water and non-ePTFE surfaces estimated at $\tau_{geom} = 70.69$ ns.

This model is validated by comparison with data collected using a reflectivity monitor, ensuring that the GEANT4 simulation accurately represents the optical behavior within the NV system.

3.2.3 Gd de-excitation models

In order to simulate the γ ray emissions following Gadolinium de-excitation in the Neutron Veto system we considered different models, with particular attention to accuracy and reliability. This modeling process is essential for understanding how Gd captures neutrons and releases gamma radiation, which in turn plays a crucial role in detecting neutron interactions.

GGarnet Model

The GGarnet model is a data-driven approach primarily designed for the SK-Gd experiment, which uses Gd-doped water. This model has been refined using neutron beam experiments from the J-PARC facility, incorporating data from a Germanium (Ge) detector array. GGarnet reproduces both continuous and discrete spectra, making it suitable for precise simulations of gamma-ray emissions in the XENONnT experiment. The Photon Strength Function (PFS) in this model uses an Enhanced Generalized Lorentzian (EGLO) model, enhancing the accuracy of gamma-ray emissions following neutron capture.

ANNRI-Gd Model

The ANNRI-Gd model, developed using neutron beam data at the Material and Life Science Experimental Facility (MLF) of J-PARC [40], is another model used for simulating Gd de-excitation. The ANNRI experiment utilizes an enriched ^{157}Gd sample and a Ge detector array. This model is specifically designed for GEANT4 *versions 9.x*, but modifications have been made to implement it in the current XENONnT simulation using GEANT4 *version 10.3.x*. While similar to the GGarnet model, the primary difference between the two lies in the Photon Strength Function: ANNRI-Gd uses a Standard Lorentzian (SLO) model, unlike GGarnet's EGLO. As can be seen in Fig. 3.6a the emission energy from Gd de-exitation γ for these two models is similar, while for what concerns the number of γ emitted from Gd in Fig. 3.6b they are slightly different due to the difference in implementations of the two codes.

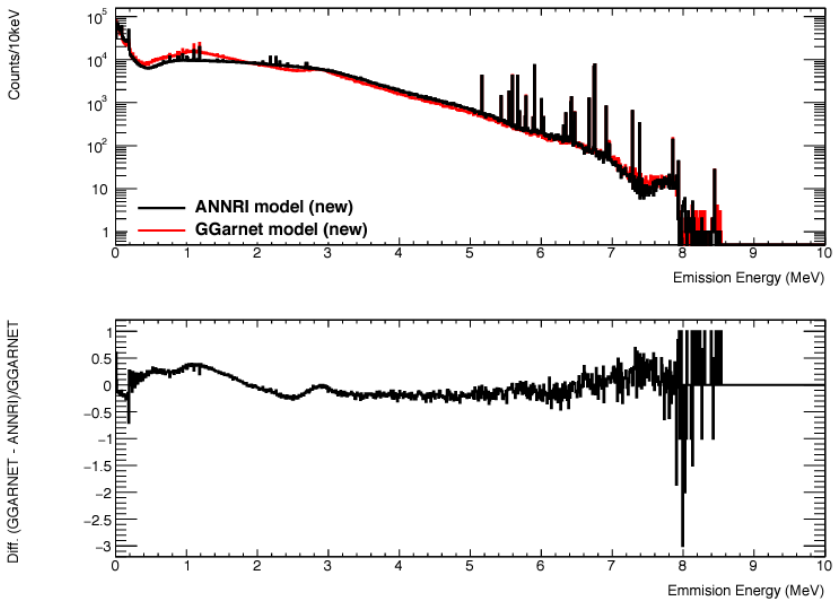

(a) Emission γ energy from Gd for different models

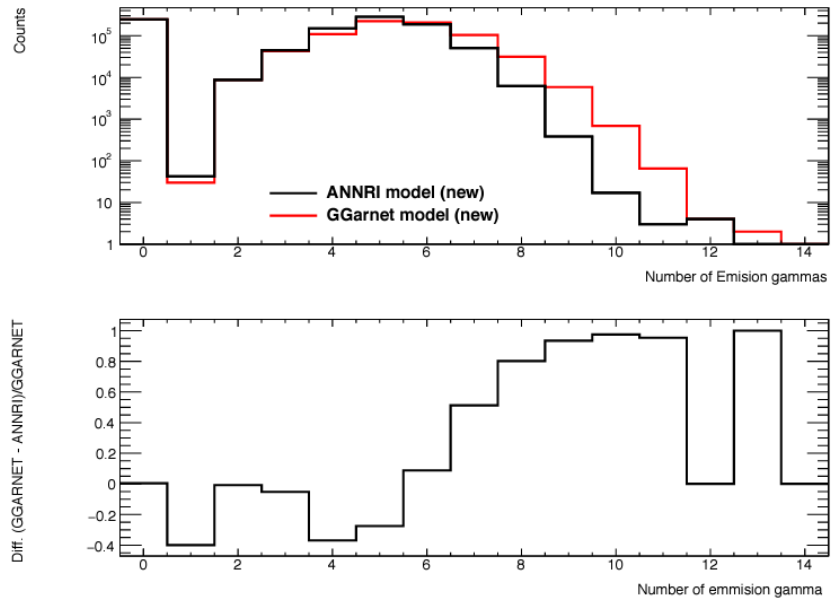

(b) Number of γ emitted from Gd

Figure 3.6: The figure at the top shows the energy spectrum of each gamma particle emitted in both ANNRI and GGarnet models, and the relative difference (second panel): these spectra are similar ($< 50\%$) for all energy regions (discrete and continuum). In the third panel, the numbers of emitted gamma for both models are represented, which are slightly different in particular at higher gamma multiplicities, together with their relative difference (bottom panel).

DICEBOX Model

DICEBOX is another sophisticated model traditionally developed at Los Alamos. While it has been available for some time, it has only recently become more accessible to the scientific community. DICEBOX is designed to simulate gamma-ray emissions for a range of nuclei, including Gd. It offers flexibility in setting parameters such as the Photon Strength Function, which can be configured to use the Standard Lorentzian (SLO) or Enhanced Generalized Lorentzian (EGLO) models.

Model selection

Several older models, including the default *GEANT4 photon evaporation model* and the *glg4sim model*, are no longer recommended for use. The GEANT4 photon evaporation model is known to have inaccuracies in conserving the total emission energy of gamma rays during Gd de-excitation. Similarly, the glg4sim model, which was developed for the KamLAND experiment, is considered outdated and does not offer advantages over newer models like GGarnet or ANNRI-Gd. For XENONnT simulations, the ANNRI-Gd model is the default for Gd de-excitation due to its higher accuracy and relevance to the experiment's needs. The GGarnet model, while similar, is also implemented and can be used depending on specific requirements or comparisons. Both models specifically focus on gamma-ray emissions following Gd decay, without affecting other hadronic processes, such as those involving xenon.

3.2.4 Neutron capture patterns

We can visualize an example of a neutron capture event of interest for the Neutron Veto thanks to a custom-developed G4-based event display. Fig. 3.7 shows an event in the Gd-doped NV generated by the emission of a neutron from a TPC's PMT, which is then captured on Gd. The following γ-emission, the Cherenkov photon production and their hit on NV PMTs are also shown in the event display.

It is useful to study the position distribution of the key processes that drive the NV capability to detect neutrons, i.e. the neutron capture, the emitted gammas and Cherenkov radiation. Fig. 3.8 shows the 95% contour profiles of neutron captures (red), end-point of gammas (light-blue), and emission point of Cherenkov photons (yellow) for neutrons emitted from the outer cryostat, with the current concentration of Gd salt (500 ppm). The last profile is particularly interesting for the analysis because it can be used as a cross-check to see if the NV design fulfills the requests for which it has been developed: the goal is that most of the Cherenkov photons should be contained inside the NV to maximize the detection efficiency. In this case, the request is almost completely satisfied, except for a few photons that escape from the NV from the top and bottom panels: this little loss is known, but can not be adjusted due to constraints in the anchoring of the

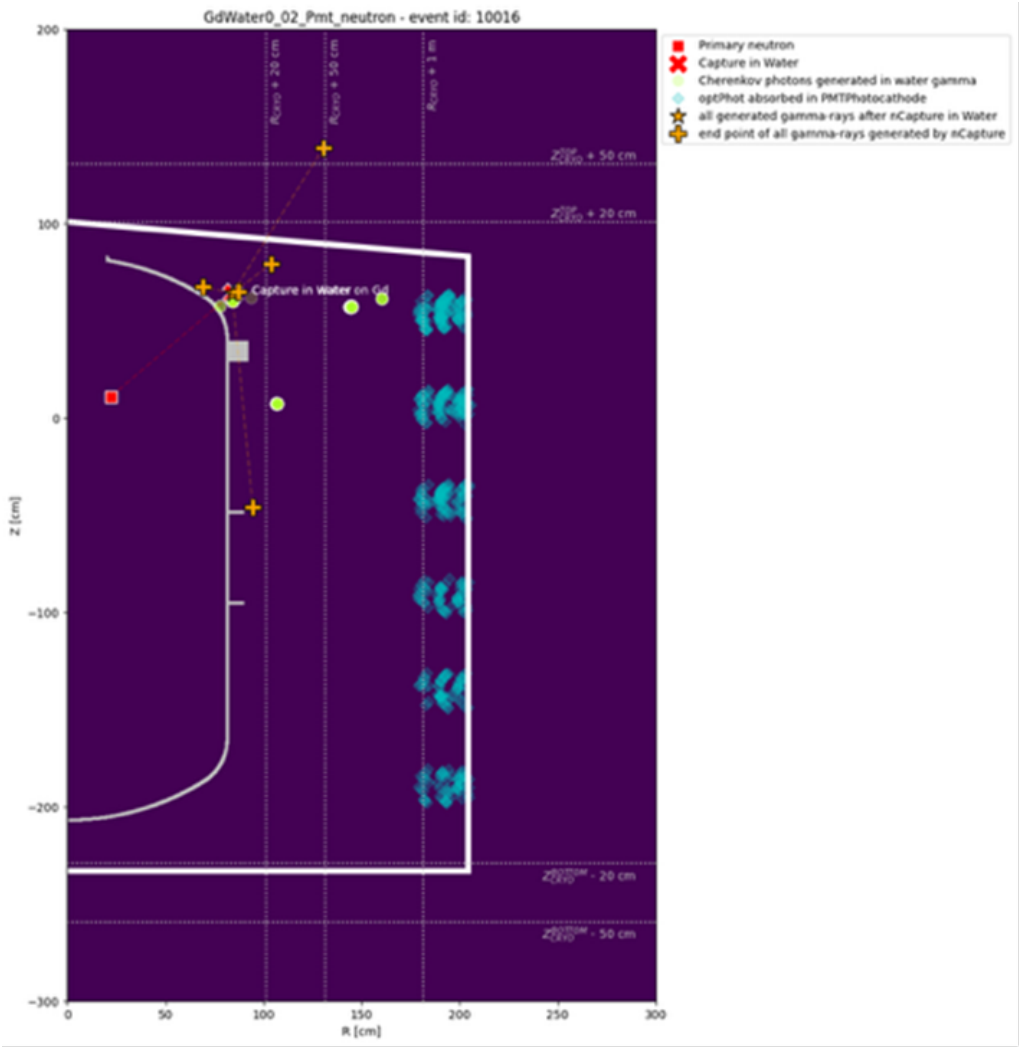

Figure 3.7: Example of a GEANT4-based event display in the XENONnT Neutron Veto. The position where the primary neutron is generated (in this case, from a PMT) is shown as a red square. A red X-shaped cross marks the position where the neutron is captured. The consequent emitted gamma rays are shown with their generation point (yellow star; very close to the neutron capture position) and their end-point (yellow cross). The position where clusters of Cherenkov photons are generated is given by lime circles. The Cherenkov photons reaching NV PMTs are displayed as cyan diamonds. The perimeter of the NV is shown in white and the profile of the outer cryostat vessel is visible in gray.

top and bottom panels.

We also simulate neutrons emitted by the AmBe calibration source (see Section 3.4), with pure-water and Gd-doped water NV configurations. Fig. 3.9a and Fig. 3.9c show

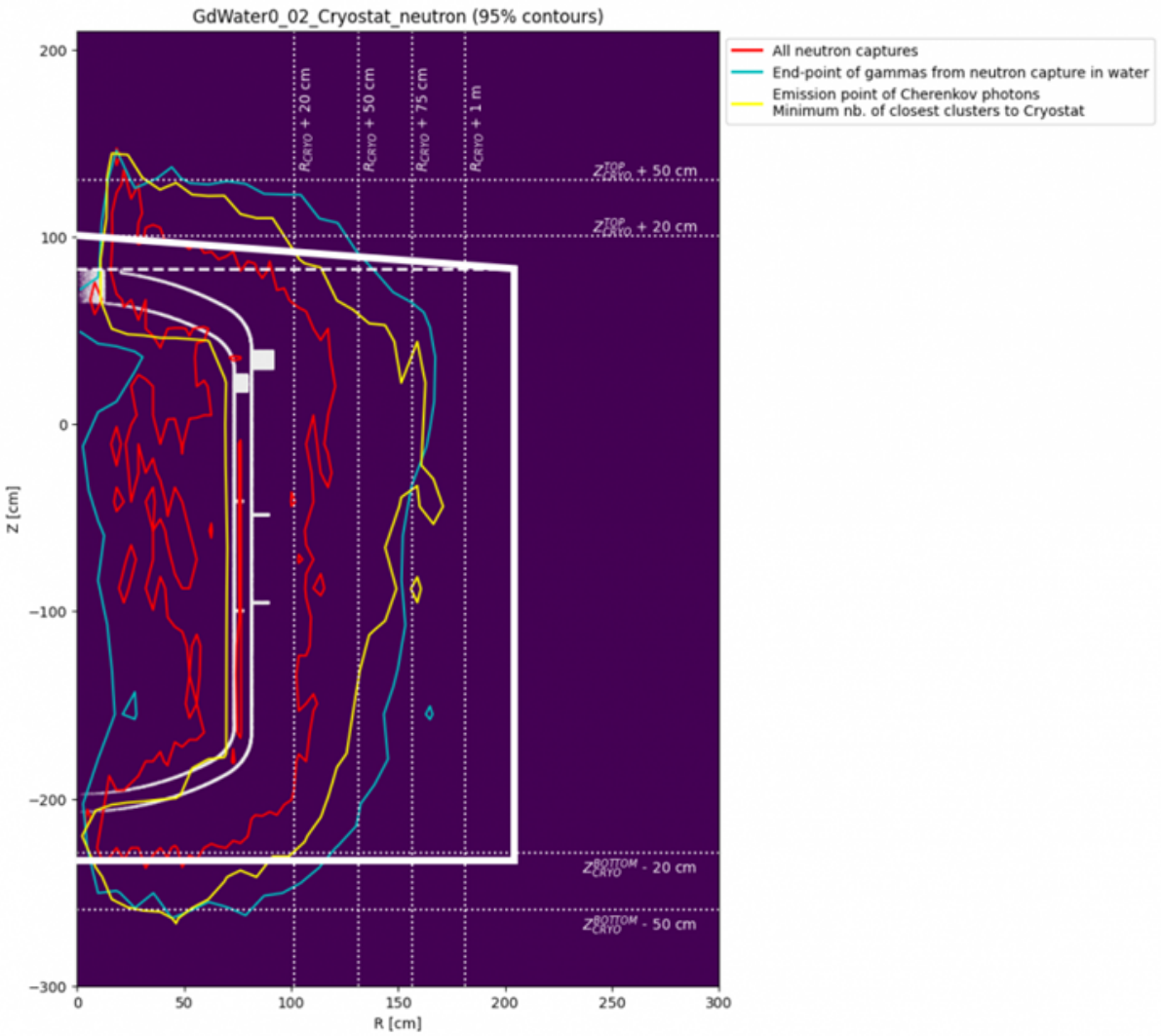

Figure 3.8: Position distribution of neutron captures (red), end-point of gammas (light-blue) and emission points of Cherenkov photons (yellow) produced with the current concentration of Gd salt (500 ppm) present in the experiment. Distributions are shown as contours that include 95% of the population.

the distribution of neutron captures for neutrons emitted from an AmBe calibration source placed in a position close to the cryostat (see Section 3.4.1). Most of the captures happen within a few centimeters from the neutron emission position in water, but neutrons can also be captured on other materials, especially on LXe inside the TPC and stainless steel components of the outer or inner cryostat vessels. The red line indicates the NV boundary, while the cryostat profile is visible thanks to the white region with no neutron captures corresponding to the empty volume between the cryostat vessels.

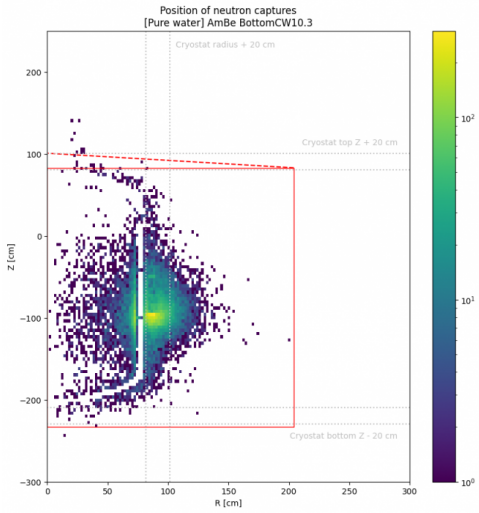

(a) Neutron capture positions in water.

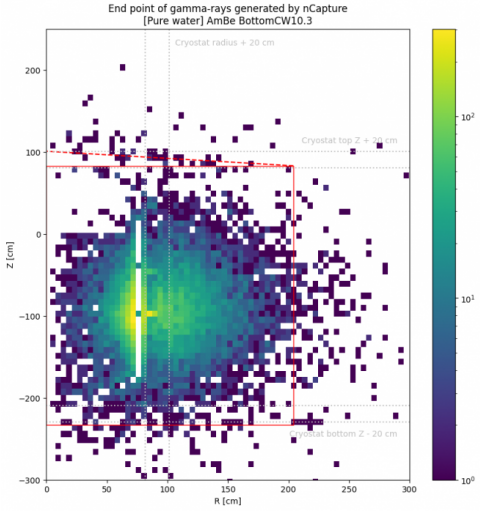

(b) Gamma end points in water.

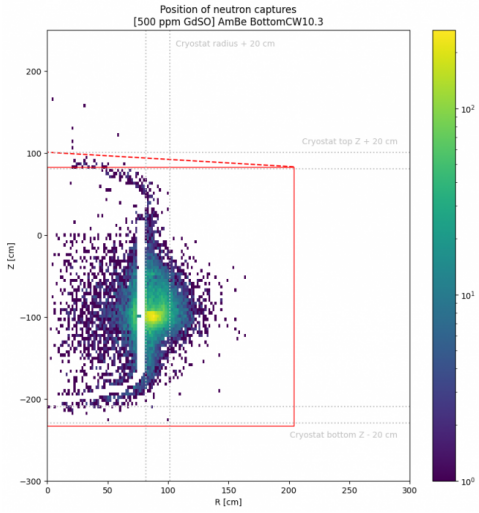

(c) Neutron capture positions in 500 ppm of GdSO.

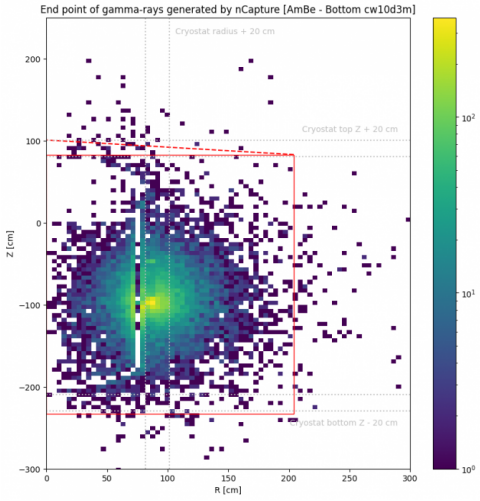

(d) Gamma end points in 500 ppm of GdSO.

Figure 3.9: Simulations of neutrons emitted by the AmBe source in the Bottom CW10d3 position (see Section 3.4.1), close to the cryostat. (Left) Positions where neutrons are captured (in water and with 500 ppm GdSO concentration). (Right) Positions where γ originated from neutron capture processes stop (top panels show the water case, while bottom ones the Gd-water case). In all the plots, the red dotted line represents the NV boundaries, while the bounded "can" in white shows the cryostat.

It is also important to understand where the gamma end-points are located: in Fig.

3.9b and Fig. 3.9d this concept is expressed with the same legenda used for neutron capture positions. As expected, the range of gamma rays is much wider than neutrons, but such radiation is almost completely confined inside the NV for this AmBe source position.

3.3 NV Hitlet Simulator

An efficient event simulator called *Hitlet Simulator* (HitSim) [41] was developed to complement the Neutron Veto MC simulations. The HitSim is designed as a fast tool for generating NV hitlets and events, assuming ideal delta-shaped PMT signals. The operational framework and methodology of HitSim are detailed in Fig. 3.10.

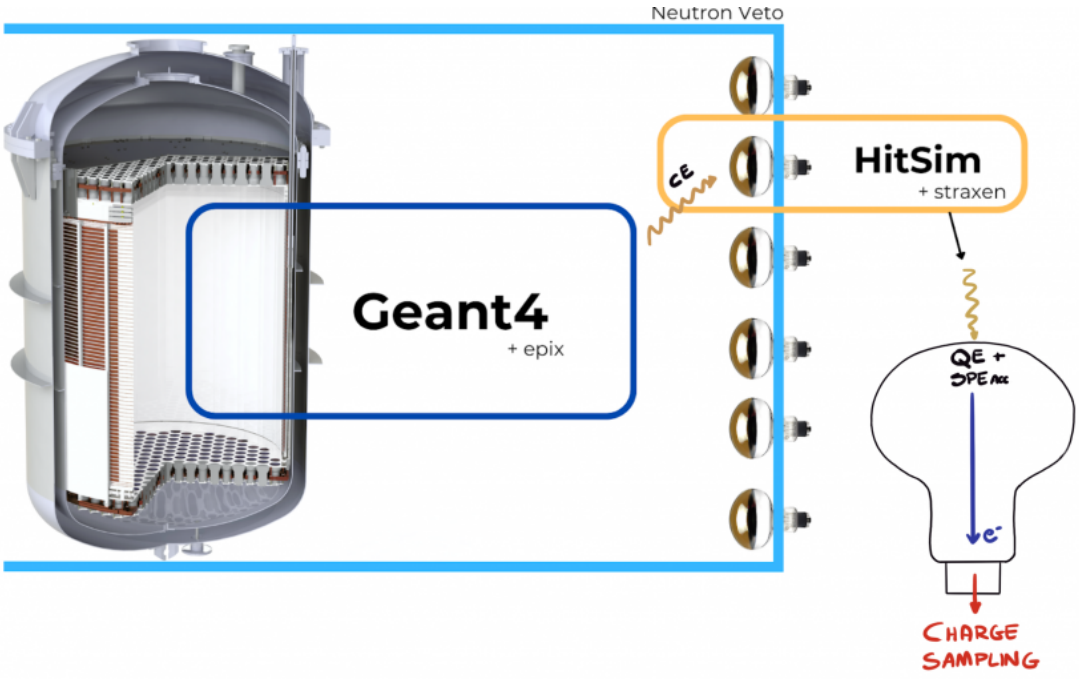

Figure 3.10: Schematic of the concept and working principle behind the Hitlet Simulator. GEANT4 takes care of all the physics processes to be simulated (blue box). Epix (Electron and Photon Instructions generator for XENON) [42] uses XENONnT GEANT4 MC data to produce inputs to the TPC Waveform-simulator (Wfsim) and thus to start the "processing"-chain of the simulated data into the TPC. Once the photon hits the NV PMT photocathode, the HitSim is used (orange box). In the HitSim, we determine if the photon is converted into a photoelectron and detected using the QE and the Single PhotoElectron (SPE) acceptance of each PMT. For each photoelectron generated, the charge is sampled from a pre-defined PDF. The hits, with their charge in photoelectrons (PE) and their timing, are then clustered into straxen hitlets and events.

For each Cherenkov photon that reaches a NV PMT, critical information such as the impact time on the PMT photocathode, the PMT channel, and the photon's wavelength, is stored in a Root TTree format, which is then processed by the HitSim.

The TPC uses a different simulator called Waveform-simulator (Wfsim), which simulates the waveform recorded by the digitizer for each hit. However, in the NV HitSim, a more simplified approach is taken, where the full time evolution of the waveform is not considered since it is not used in the analysis process, treating the PMT signal as a delta pulse.

Photon detection process in HitSim

The processing of raw waveforms recorded by the NV DAQ system is handled by an event builder using two open-source Python packages: *strax* and *straxen*. Strax provides a framework for processing chain which finds peaks and organizes them as time-ordered peak-like data, while straxen includes custom code tailored to the XENONnT experiment. To process the outcome of the NV simulation in HitSim, hits are converted into straxen events. The first step is to convert impinging photons into "detected" photons. Detection occurs when a photon generates a photoelectron at the PMT photocathode, with the probability of PE generation dependent on the photon's wavelength and the PMT's quantum efficiency. Once a PE is generated, it must reach the first dynode in the amplification stage, with its efficiency depending on the PMT's collection efficiency (CE). The overall detection probability for a single photon is represented as the following binomial distribution:

$$p_{det}(\lambda) = Binom(n = 1, p = QE_i(\lambda) \times CE) \tag{3.2}$$

where $QE_i(\lambda)$ refers to the wavelength-dependent quantum efficiency of the i-th PMT. The QE for each PMT is well-documented through Hamamatsu measurements. Fig. 3.11 illustrates the impact of applying the QE on the Cherenkov photon spectrum. The QE reaches its maximum around 350 nm, though the number of emitted Cherenkov photons per unit wavelength is inversely proportional to the wavelength squared, shifting maximum sensitivity slightly below 350 nm. Approximately 75% of the Cherenkov spectrum falls within the [290, 440] nm range, where NV is most responsive.

The CE of each PMT is less well-known and varies between PMTs. An average CE value is therefore used in HitSim, encapsulating uncertainties and discrepancies between the actual detector geometry and the simulation. In this context, CE accounts for more than just the PMT's behavior: it also captures potential mismatches between the real detector configuration and the simulated model.

SPE acceptance and detection threshold

When simulating photon detection, it is important to account for the hardware threshold imposed by the DAQ, which is set to 15 ADC counts for most channels. This threshold

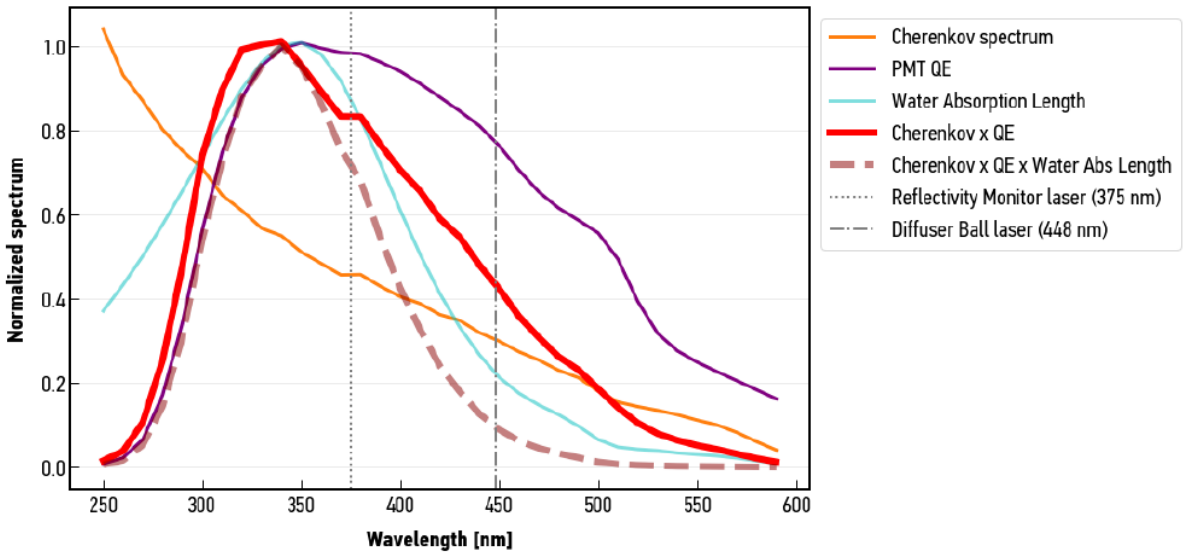

Figure 3.11: Quantum efficiency curve of one PMT (purple) overlapped and convoluted (red) to the energy spectrum of the Cherenkov photon hits (orange) from the GEANT4 output. The model of the water absorption length (cyan) used in the simulation is also reported and is convoluted to the Cherenkov Spectrum and to the QE (dashed brown). The two dashed thin black vertical lines refer to the wavelength of the Reflectivity Monitor and Diffuser Ball lasers used for the optical calibrations of the NV.

directly impacts the SPE acceptance, a critical factor in determining whether a photon hit is recorded by the PMT. SPE acceptance, derived through dedicated LED calibrations, is incorporated into the photon detection probability, modifying the detection formula to:

$$p_{det}(\lambda) = Binom(n = 1, p = QE_i(\lambda) \times CE \times SPEAcc) \tag{3.3}$$

Charge Sampling

Once a photon is detected, HitSim samples the charge associated with each detected hit using a SPE model developed during the SR1 calibration campaign, known for its robustness. This SPE model has two components: one representing under-amplified electrons via a smoothed box function, and another modeling fully-amplified electrons through a Poissonian Gaussian distribution. However, due to the DAQ hardware threshold, under-amplified electrons are often not recorded, leading to inaccuracies when using only the raw SPE model components.

To solve this, HitSim employs a hybrid charge sampling model that combines real data distributions with theoretical fit functions, compensating for the ADC threshold's impact on the charge distribution. The final charge-sampling PDF merges actual data

with theoretical predictions, as illustrated in Fig. 3.12.

Pseudo-Hitlets and Event Processing

After charge sampling, the resulting pseudo-hits are converted into hitlets via the straxen plugin. Each hitlet is treated as a delta pulse and contains information about time, PMT channel and charge. Since the timing of these hitlets is relative to the simulated GEANT4 events, HitSim applies an additional time offset. This offset can be either uniformly distributed, to simulate well-separated events, or follow a specific source rate to replicate event pile-up scenarios.

Once these pseudo-hitlets are generated, they are processed through the standard NV plugins to compute event properties, which are then compared with real experimental data to assess the efficiency and accuracy of the simulation.

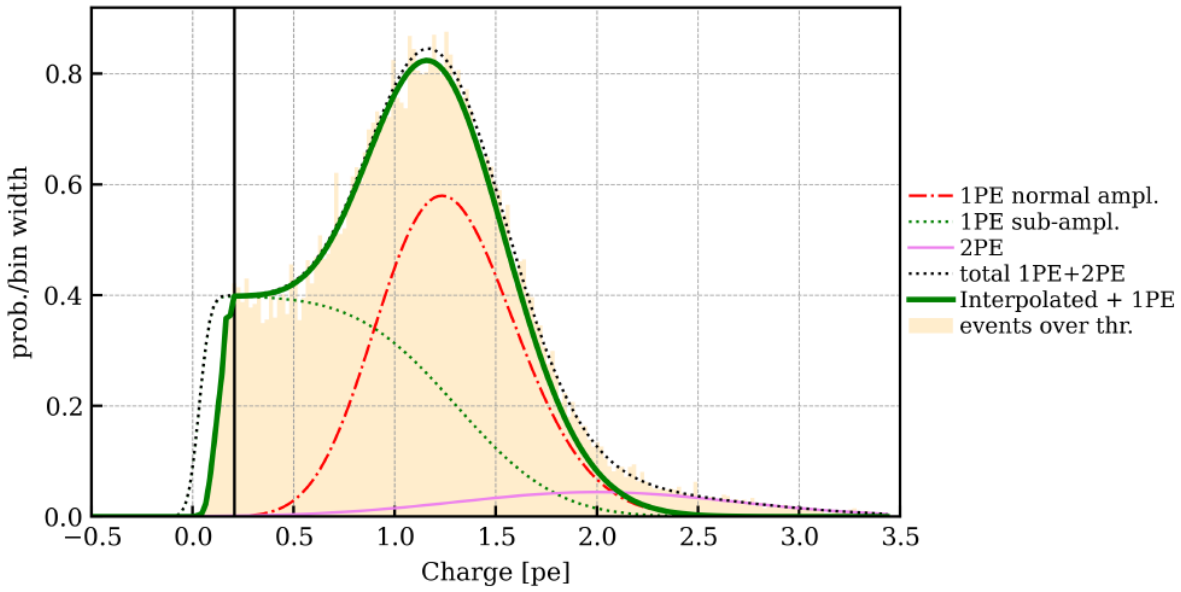

Figure 3.12: Example of a charge distribution of a NV PMT used for the charge sampling in the HitSim. It is a combination of the data with the 15 ADC count amplitude threshold applied (orange distribution) and of the SPE fit function (dashed thin black line). Up to the first intersection point (marked with the solid vertical line), the distribution follows the data, then it continues with the fit function. The final SPE model used by the HitSim is shown with the solid green line.

Validation and evaluation of the CE parameter

The HitSim has been successfully used to estimate the *effective Collection Efficiency* (CE) based on AmBe calibration datasets. To achieve this, simulations were carried out with the AmBe source placed at the position Top CW5d9 (radial distance of 13 cm from the cryostat), testing a range of CE values from 0.6 to 1.

The event area distributions from both the simulation and the actual data were compared to identify the optimal CE value: a quantitative evaluation focused on the positions of the expected 4.4 MeV and 2.2 MeV peaks (due to the gamma-ray from C de-excitation and neutron capture on H, respectively, see Section 4.1) in the AmBe area spectrum observed by the NV. Fig. 3.13 shows the simulated peak positions of the 4.4 MeV gammas (left) and the 2.2 MeV peak (right) for different CE values. The positions of these peaks in the observed NV data are shown as horizontal lines, with uncertainty marked by dashed lines. The most appropriate CE value for accurately simulating the experimental data is 87%, given by the best MC-data match for the neutron capture peak.

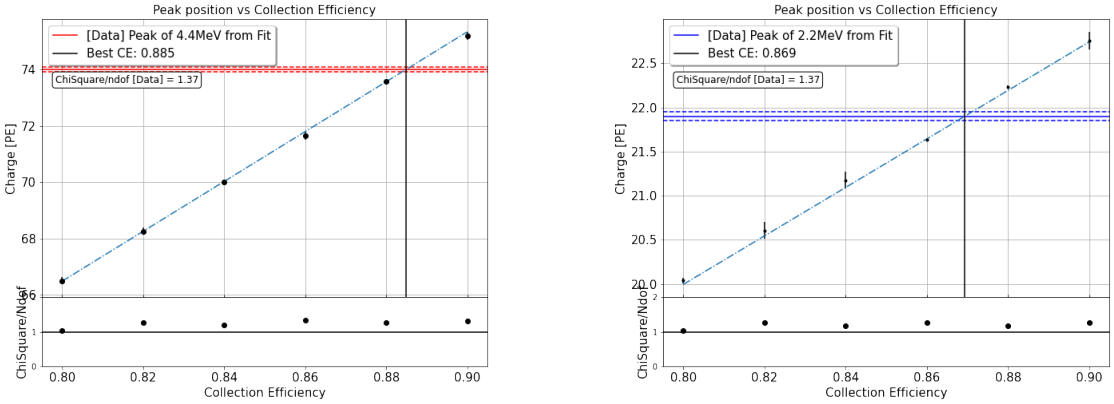

Figure 3.13: Positions of the 4.4 MeV (left) and 2.2 MeV (right) peaks in the simulated AmBe charge spectrum varying the Collection Efficiency in the range [0.8, 0.9] for SR1. From the intersection of the linear fit (dashed thin blue line) and the position of the peaks observed in real data (red/blue lines) we determined the CE value that best matches MC and data. The best CE from the two plots do not differ significantly; however, we decided to rely on the one inferred from the 2.2 MeV match since the neutron capture is the process of major interest for the NV. In the bottom panels, the reduced χ^2 of the fit of the simulated spectra are shown.

3.4 Simulation of AmBe neutron source

During the data acquisition phase of XENONnT, typically at the start of a Science Run, calibrations were conducted using neutron and gamma sources, specifically Americium-Beryllium (AmBe) and Thorium (precisely ^{232}Th). The primary calibration, critical for understanding the detector's response to elastic interactions with xenon nuclei - essential for both WIMP DM searches and CEνNS - is the Nuclear Recoil calibration of the TPC. This calibration also plays a key role in determining the NV tagging efficiency. A novel coincidence technique, which involves the simultaneous detection of neutrons and gammas emitted from an AmBe source, is applied during the calibration analysis to correlate events in both the NV and the TPC. This Section examines the key characteristics of the AmBe source and the operational principles of this calibration technique.

Neutrons are particularly useful for studying the detector's response to WIMP interactions because both processes result in elastic Nuclear Recoils in Xenon. However, neutrons also pose significant challenges for XENONnT's scientific goals: neutrons originating from spontaneous fission or (α, n) reactions within detector materials can enter the TPC fiducial volume and produce signals that mimic WIMPs. Although many neutron interactions can be distinguished from WIMP events since they may produce multiple scatters, distinguishing these interactions becomes difficult when energy deposits are small. The NV is designed to tag these neutrons by detecting the γ-ray emitted during neutron capture on H or on Gd, thereby mitigating this background source: to characterize the neutron tagging efficiency, calibrations of the NV neutron response are needed. The neutron detection efficiency of the NV, instead, is a measure of the probability of detecting a neutron after its emission and serves mainly as a benchmark for comparing the NV performance with other water Cherenkov detectors like SNO (Sudbury Neutrino Observatory) or SK.

3.4.1 Positions for AmBe calibration

In February 2021, during the commissioning of the Neutron Veto, the first calibration was conducted using a ^{232}Th source, a process repeated a few months later. Though of secondary importance compared to neutron-based calibrations, this gamma source played a key role in serving as a reference for future calibrations, particularly for positioning the AmBe source through the detector's calibration pipes, also known as U-tubes as illustrated in Fig. 3.14. The encapsulated ^{232}Th source was carefully moved through the U tubes to assess the spatial response of the NV to gamma emissions. The significance of using the ^{232}Th source lies in the proximity of its gamma emissions to the energy released during neutron capture in water (2.2 MeV), making it suitable for a preliminary evaluation of the NV's resolution and photon detection timing. Additionally, this process helped to determine the precise positioning of the calibration source within the NV, crucial for accurate neutron calibration where distance from the TPC must also be

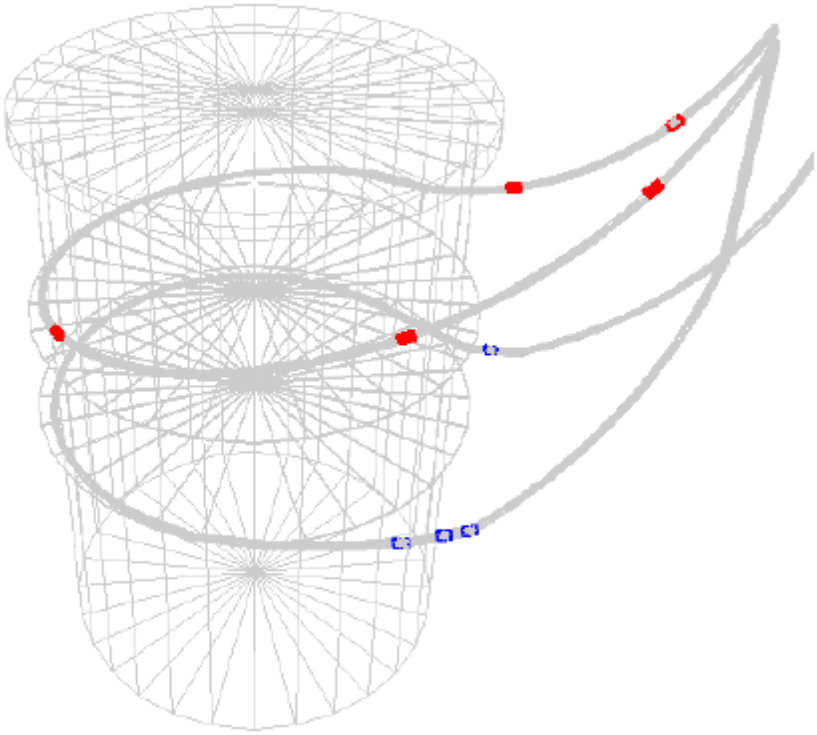

Figure 3.14: Schematic of the U-tubes embracing the cryostat, as it results from the detector geometry implemented in the GEANT4 simulation framework.

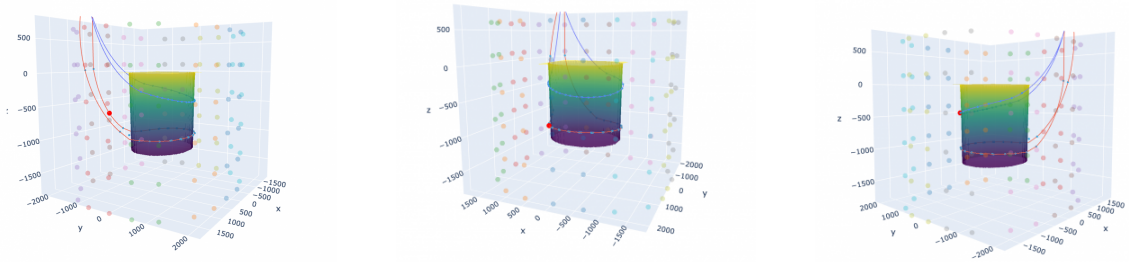

(a) (b) (c)

Figure 3.15: Visual representation of different positions for placement of AmBe source during AmBe calibration of the Neutron Veto: Fig. 3.15a represents position Bottom CW6d0, Fig. 3.15b is Bottom CW10d3 and Fig. 3.15c stands for position Top CW7d8. The small red dot indicates where the source is located. The TPC volume and the U-tubes surrounding it are also visible, as well as the NV PMTs.

considered.

Source positions were identified with specific nomenclature: an example is **Bottom CW6d9** (sometimes also written as Bottom CW6d9m or Bottom CW6.9) where is included respectively the U-tube chosen for the insertion of the source (Top or Bottom), tube orientation (CW means ClockWise) and the insertion depth (in this case of 6.9 meters). In Fig. 3.15 are represented three different positions commonly used for the AmBe calibration: Bottom CW6d0, Bottom CW10d3, Top CW7d8 (see Tab. 3.1 for details). This calibration allowed for a foundational understanding of both the detector's spatial and energy resolution, setting the stage for future calibrations with neutron sources.

Main AmBe positions

Name	Bottom CW6d0	Top CW5d9	Bottom CW10d3	Top CW7d8
Radial distance from cryostat	54 cm	13.0 cm	1.2 cm	0.3 cm

Table 3.1: Nomenclature and radial distance from the cryostat of the most used positions of the AmBe calibration source.

3.4.2 AmBe source

The AmBe calibration source used in XENONnT emits neutrons through the reaction ^{9}Be(α, n)^{12}C, where ^{12}C can end up either in the ground or first excited state. This characteristic makes the source particularly useful for calibration, as the gamma-ray emitted when ^{12}C is in its first excited state allows for clear identification of neutron interactions in either the NV or the TPC through tight coincidence between the two detectors. The alpha particles responsible for this reaction are emitted by ^{241}Am, which decays with a half-life of about 432.2 years into an excited state of ^{237}Np* at an energy level of 60 keV. The subsequent alpha capture on ^{9}Be forms a ^{13}C* nucleus, which decays via neutron emission into either the ^{12}C ground state or one of its excited states, with the two most relevant energy levels being 4.44 MeV and 7.65 MeV. A diagram of these energy levels is depicted in Fig. 3.16.

The branching ratio for the different states is determined by the kinetic energy of the alpha particles when they interact with the ^{9}Be nucleus, and this energy varies depending on how the source is manufactured. According to literature [44, 45], the branching ratio for the first excited state of ^{12}C is typically around 60%, though this is slightly lower than the 67% expected from neutron production cross-sections at the typical alpha energy of 5.5 MeV from ^{241}Am. Studies conducted during Science Run 0 revealed that the branching ratio for the source used in XENONnT was slightly lower, around 50%. A dedicated study with MC simulations of AmBe calibration data matched

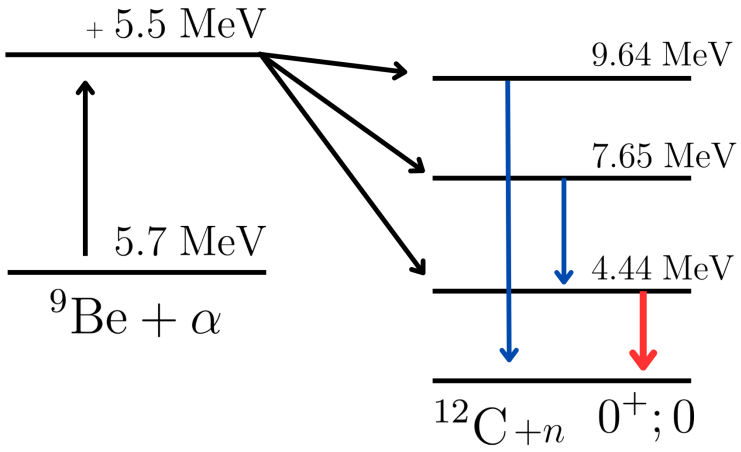

Figure 3.16: Schematic of the energy levels involved in the ^{9}Be(α, n)^{12}C reaction. The maximum kinetic energy of the ^{241}Am alpha particles is indicated by an additional energy level 5.5 MeV above the ground state of ^{9}Be. Blue arrows represent transitions via internal conversion, while the red arrow indicates a transition via gamma emission. The energy levels and the transition properties of ^{12}C are sourced from [43].

to Science Run 1 data has been carried out to determine such branching ratio (see Section 4.2). At the time of the calibration, the source had a neutron emission rate of (159 ± 4) neutrons/s, estimated based on the decay rate measured in 2013 for XENON100 [46] and accounting for the half-life of ^{241}Am.

Neutron energy spectrum

The neutron energy spectrum from the AmBe source - shown in Fig. 3.17 - is continuous, with a maximum energy around 11 MeV and an average energy of about 4.5 MeV. These values also vary slightly depending on the manufacturing process of the source. The spectrum includes distinct peaks corresponding to specific neutron production cross-sections.

There are three key components of the neutron spectrum [47], as shown in Fig. 3.17:

- (1) ^{12}C is in the second excited state (or higher), it disintegrates into 3 alpha particles with 99.96% probability and only a neutron of low energy is created.
- (2) ^{12}C is in the first excited state, both a neutro,n with intermediate energy, and a 4.4 MeV gamma are emitted.
- (3) ^{12}C is in the ground state, only a neutron is emitted, but the energy is larger.

In the past, simulations used the entire neutron spectrum without distinguishing between these components. However, for accurate estimation of the NV tagging efficiency - for

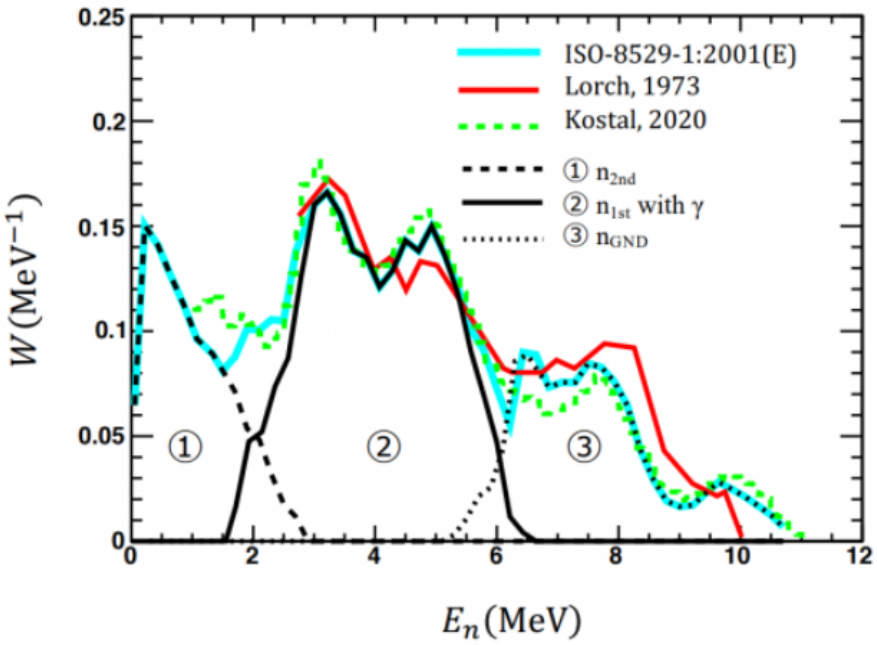

Figure 3.17: The entire neutron spectrum from an AmBe source and its three components, from [47].

which only the component with gamma coincidence is exploited - one needs to separate the simulation of AmBe neutrons emitted with or without the coincident gamma.

To account for the correlation between neutron energy and gamma emissions, we perform two separate simulations for each AmBe source position:

1. Neutron + γ simulation: This simulation uses the component of the neutron spectrum where a gamma ray is coincident with the neutron (the first excited state of ^{12}C) and sets the gamma-to-neutron ratio to 1.

2. Neutron-only simulation: This simulation uses the remaining components of the neutron spectrum, where no gamma is emitted, and sets the gamma-to-neutron ratio to 0.

If the Neutron Veto tagging is targeted, only the neutron + γ simulation results should be utilized. For rate matching purposes, the results of both simulations should be combined using the appropriate branching ratio.

3.5 Simulation of radiogenic neutrons and NV tagging efficiency

3.5.1 Background neutrons from detector components

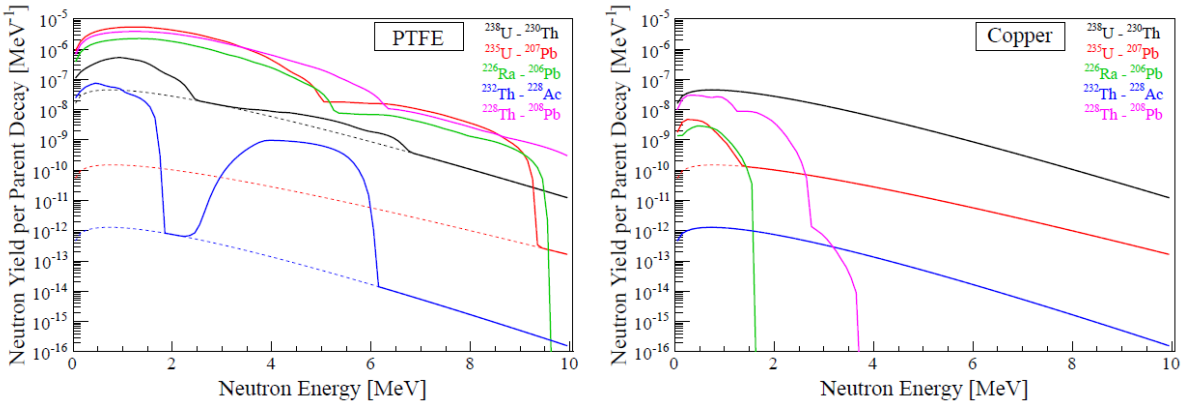

Figure 3.18: Differential yield of radiogenic neutrons in PTFE (left) and copper (right), normalized per each decay of the parent nucleus in the chain. The solid line represents the sum of neutrons from spontaneous fission and (α, n) reaction, while the dashed line shows the contribution of spontaneous fission only. The following decay chains are shown: ^{238}U $\rightarrow$ ^{230}Th (black), ^{226}Ra $\rightarrow$ ^{206}Pb (green), ^{235}U $\rightarrow$ ^{207}Pb (red), ^{232}Th $\rightarrow$ ^{228}Ac (blue), ^{228}Th $\rightarrow$ ^{208}Pb (purple).

The production rates and energy spectra of radiogenic neutrons (in Fig. 3.18) were calculated using the SOURCES-4A software [48], following the procedure used for XENON100 [49, 50]. Fig. 3.18 presents the neutron yield per parent decay for all the five relevant radioisotopes considered in the background predictions (^{238}U, ^{235}U, ^{226}Ra, ^{232}Th and ^{228}Th), taking into account chain disequilibrium. For heavy nuclei, the high Coulomb barrier significantly suppresses the (α, n) interaction, meaning neutron production is mostly due to spontaneous fission. The highest (α, n) yields come from lighter materials, such as PTFE and the ceramic in the PMT stems. Notably, neutron emission from the first part of the ^{232}Th chain is negligible. The energy spectra for two materials, PTFE (low atomic number) and copper (high atomic number) are shown in Fig. 3.18. The typical energy range of radiogenic neutrons extends up to $\sim$ 10 MeV, and for this reason AmBe neutrons are a suitable calibration sample to calibrate the XENONnT's detectors response to dangerous background neutrons, both for the TPC and NV.

For each detector component (26 in total, visible in detail in Fig. 3.19) 10^7 neutrons have been generated, using the energy spectra obtained with SOURCES-4A for each neutron source (5 radiogenic isotopes mentioned above). The events contributing to the

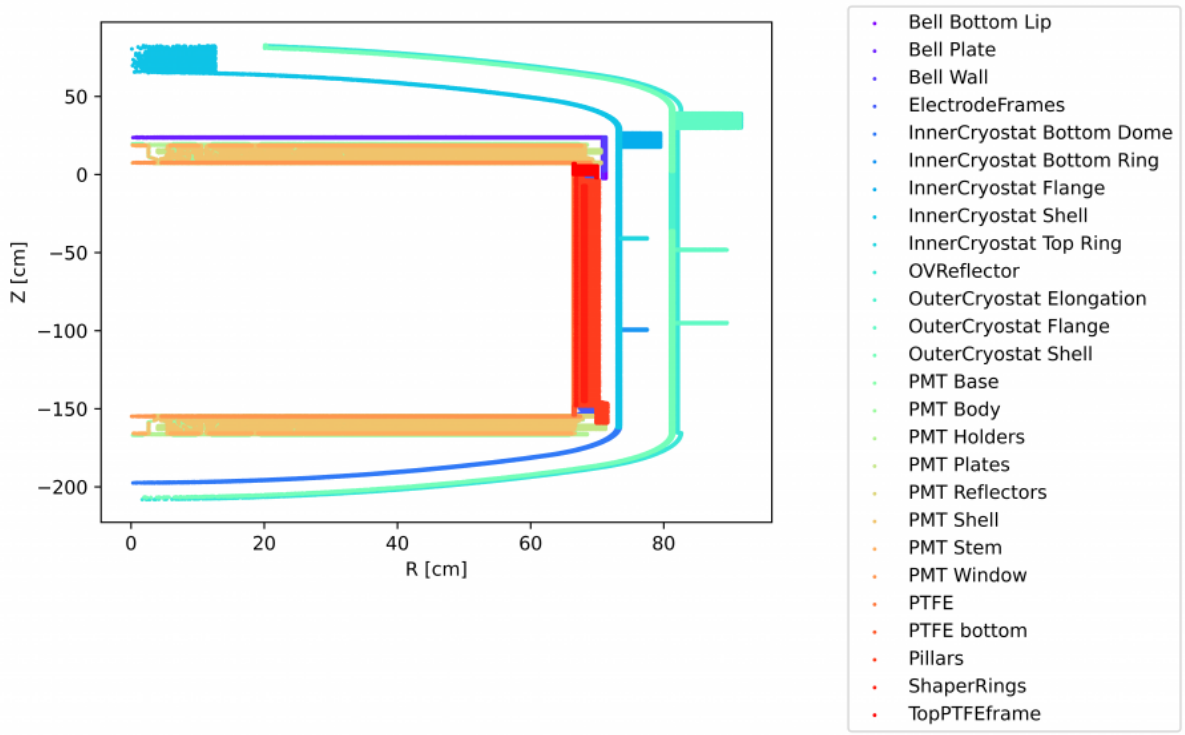

Figure 3.19: Location of all the 26 detector components simulated in GEANT4 considered for the neutron background model and the study of the NV tagging efficiency.

background budget for WIMP searches are those that mimic a WIMP signal through a single elastic scatter in the active volume, and that occur within the fiducial volume. The neutron background rate expectations are scaled by the neutron yield of each material and the contamination level of the respective component. The largest contributors to background events are the cryostat stainless steel at 28%, followed by the PMTs at 26% (mainly from the ceramic stem), PTFE at 20%, the stainless steel of the TPC at 10%, the reservoir at 7%, and the PMT bases at 5%.

3.5.2 Simulated Neutron Veto tagging efficiency

The NV tagging efficiency for the total neutron background model has been simulated using Montecarlo NV signals processed with the NV Hitlet Simulator. The full inventory of massive MC simulation of radiogenic neutrons emitted by each detector component and radioisotope is taken into account. The neutron interactions inside the TPC are simulated using the Waveform-simulator such that the exact same selection cuts as those applied to the XENONnT science data for WIMP search can be imposed to the simulated data. Therefore, only the events producing a single NR scatter inside the fiducial volume

are selected to evaluate the corresponding NV tagging efficiency. NV signals associated to the selected "dangerous" neutron events are processed from original GEANT4 files using the NV Hitlet Simulator configured for SR1. NV events are matched to TPC events through the GEANT4-id identifier (which is propagated to the Wfsim output) and no time coincidence is imposed between TPC and NV events at this stage.

To evaluate tagging efficiency, NV signals are selected based on area threshold and number of contributing PMTs, up to a maximum of 20. For cases with multiple NV signals linked to a single TPC event, the signal with the largest area is selected. The number of detected NV events is divided by the total number of Nuclear Recoil Single Scatter (NRSS) TPC events to calculate the tagging efficiency and statistical uncertainty for each of the 130 neutron sources considered.

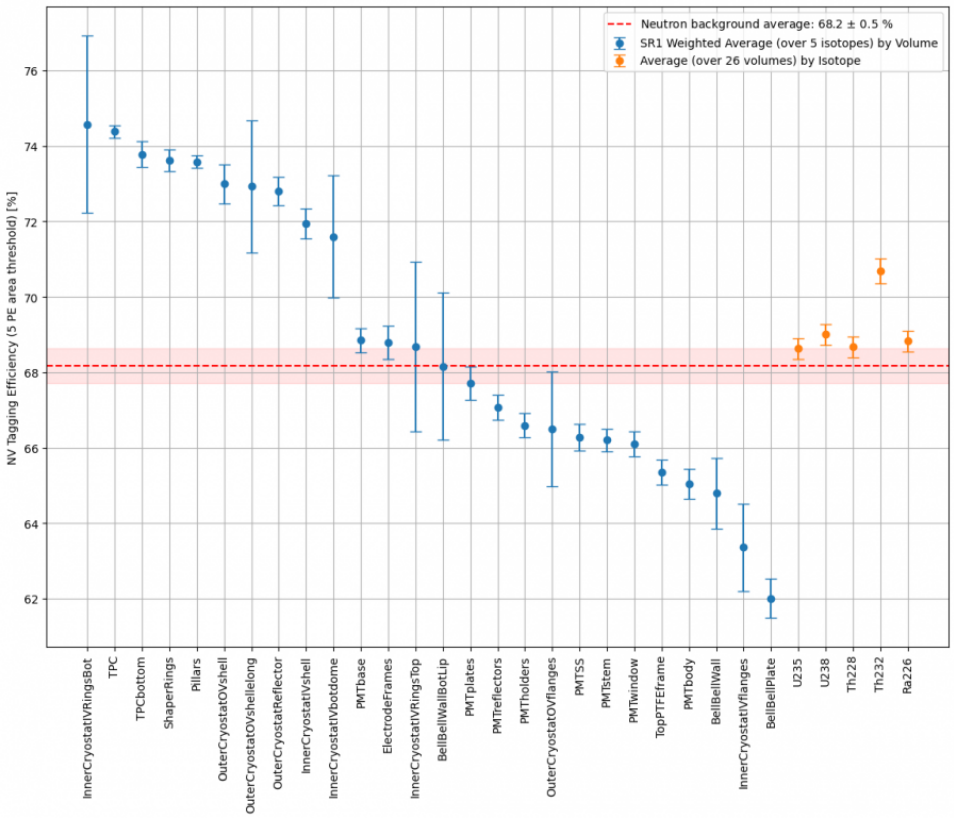

Figure 3.20: NV tagging efficiency (5 PE area threshold and 5-fold coincidence) grouped by volumes (blue points) and isotopes (orange points). The weighted average over the 5 simulated isotopes per each volume is shown with blue points. The average over the detector volumes for each simulated isotope is given as orange points. The red dotted line indicates the overall average, weighted for the specific contribution to the total neutron background of each single volume-isotope couple.

Fig. 3.20 shows the NV tagging efficiency grouped by volumes and isotopes computed as weighted average over the 5 isotopes simulated per volume. The NV tagging efficiency can vary from 74% to 62%, depending on the specific detector component where the neutrons are originating from, mostly due to different probabilities of being captured on materials different than water surrounding the cryostat. The overall NV tagging efficiency is determined as the weighted average of individual results from each background source, with weights derived from the contribution to NRSS inside the fiducial volume. The weighted average NV tagging efficiency for the overall neutron background model (single scatters within the fiducial volume) is presented in Fig. 3.21 as a function of NV area threshold and multiplicity, with statistical uncertainty. The NV overall tagging efficiency for a minimum area of 5 PE and multiplicity thresholds of 5 - corresponding to the choice made for the WIMP search - is $68.2 \pm 0.5\%$, in demineralized water.

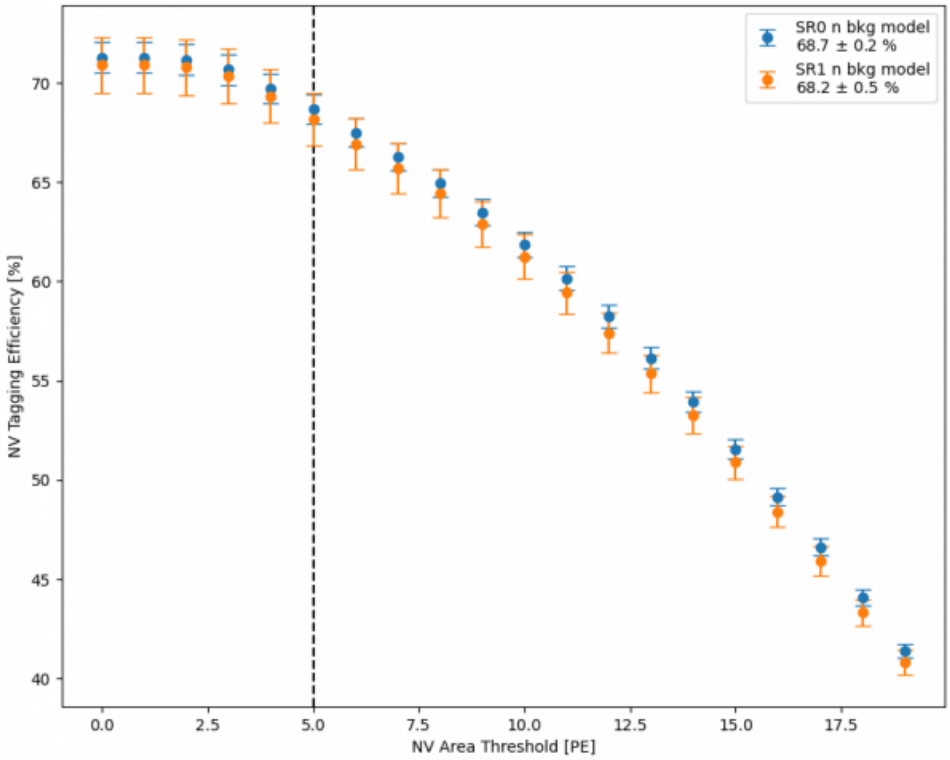

Figure 3.21: Weighted average of the NV tagging efficiency for the overall neutron background model (single scatters inside the FV). The error bars show the statistical uncertainty propagated on the weighted average tagging efficiency. The tagging efficiency is shown as a function of the NV area threshold [PE] and corresponding multiplicity [number of contributing PMTs] (e.g. area threshold = 10 PE → multiplicity threshold = 10-fold coincidence). The legend shows the results for a threshold of 5 PE (and 5-fold coincidence).

Fig. 3.21 also reports the results of the same study but using the SR0 neutron background model, which differs from the SR1 one due to a re-evaluation of the activity of specific parts of the inner and outer cryostat and bell, performed after the observation in SR0 of a NR rate larger than expected. The comparison between SR1 and the previous SR0 model shows that the SR1 tagging efficiency is slightly lower, mostly due to the increased contribution from the Inner Cryostat Flange, which exhibits lower tagging efficiency than other volumes. Nonetheless, the tagging efficiency results from both SR0 and SR1 models are consistent within the MC statistical uncertainty, indicating that changes in the neutron background model have no significant impact on the NV tagging efficiency.

Projected NV tagging efficiency with Gd

The neutron tagging efficiency was estimated assuming pure-water, and Gd-doped water NV configurations at different Gd concentrations.

The two main sources of neutron background have been simulated using GEANT4: cryostat and PMTs, which account for $\sim$ 70% of the total neutron background. Simulations were performed for the following Gd-sulphate concentrations: 0 (pure water), 0.005%, 0.05% and 0.5% (final goal of XENONnT). The analysis method develops over three main steps:

1. **Selection of TPC events**: we simplified the event selection to include multiple scatter NR events in the TPC. No additional cuts, such as fiducial volume, were applied.

2. **Processing NV events**: the selected TPC events were matched to the corresponding NV events by their GEANT4 event IDs. These events were processed through the NV HitSim, determining how many PMTs detected neutron signals. The number of separate contributing PMTs was counted, and the NV tagging efficiency was plotted as a function of PMT multiplicity (N), representing the fraction of events detected by at least N PMTs.

The final plot in Fig. 3.22 compares the NV tagging efficiency for different neutron sources and Gd concentrations, as detailed above. The tabulated data in Tab. 3.2 summarizes the tagging efficiency results for each condition for 5-fold coincidence. The prediction for the neutron tagging efficiency with the final concentration of 5000 ppm of Gd-Sulfate Octahydrate (GdSO) is $\sim$ 85%. The absolute gain in terms of tagging efficiency from the pure water case to 0.05% GdSO concentration is similar to that given by a further increase in GdSO concentration up to 0.5%, i.e. $\sim$ 6%.

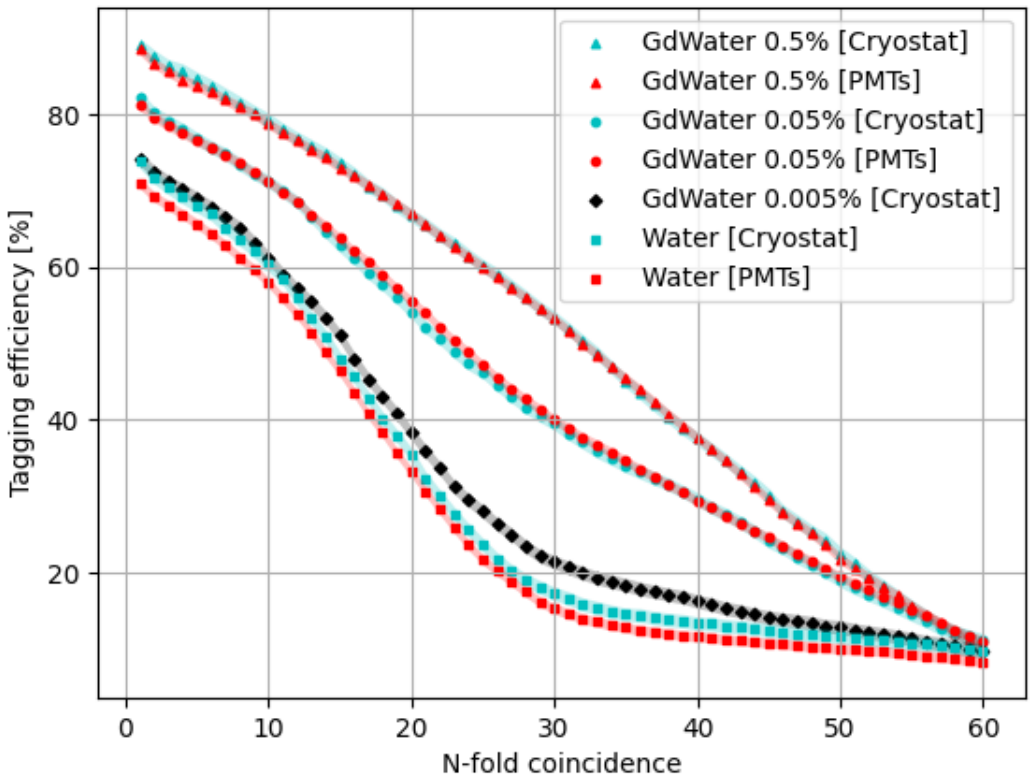

Figure 3.22: Simulated neutron tagging efficiency for radiogenic neutrons emitted from cryostat and PMTs, with different Gd concentrations as a function of the n-fold coincidence requirement. The NV selection cuts used in the data analysis is applied.

NV Configuration [neutron source]	Tagging efficiency (5-fold coincidence)
GdWater 0.5% [Cryostat]	$84.7 \pm 0.9\%$
GdWater 0.5% [PMTs]	$83.7 \pm 0.7\%$
GdWater 0.05% [Cryostat]	$76.8 \pm 0.8\%$
GdWater 0.05% [PMTs]	$76.6 \pm 0.7\%$
GdWater 0.005% [Cryostat]	$69.0 \pm 0.9\%$
Water [Cryostat]	$68.0 \pm 0.9\%$
Water [PMTs]	$65.7 \pm 0.7\%$

Table 3.2: Neutron tagging efficiency for the main radiogenic neutron sources of the experiment, cryostat and PMTs, for different concentrations of Gd sulphate. Only the 5-fold coincidence requirement is shown, the one currently used in the NV data analysis. The estimated systematic uncertainty based on the MC statistics generated for each set of simulation is reported.

Chapter 4

Study of the AmBe calibration data

The XENONnT experiment began data-taking in 2021, followed by two Scientific Runs - SR0 and SR1 - during which the Neutron Veto was operated as a pure water Cherenkov detector. In October 2023, Gadolinium was introduced into the water tank, and data-taking for the third Scientific Run (SR2) started, with the NV functioning as a Gd-doped subdetector.

This chapter examines the analysis and modeling of calibration data obtained from an AmBe neutron source. Section 4.1 outlines the methodology for processing AmBe data collected in pure water, while Section 4.2 focuses on characterizing the neutron source itself. In Section 4.3, the neutron tagging efficiency is evaluated, providing insight into the detection capabilities of the Neutron Veto system under various configurations. Section 4.4 describes the introduction of Gadolinium into the Neutron Veto system, with subsections dedicated to the Gd-doping process (Section 4.4.1) and its impact on Neutron Veto performance (Section 4.4.2). Lastly, Section 4.5 compares real experimental data with Montecarlo simulations, validating the model and contributing to the overall improvement of the system's performance.

4.1 Data analysis and modeling of AmBe data in pure water

This section aims to analytically describe the AmBe spectrum and determine the total source rate. This analysis is critical for defining the selection boundaries for the 4.44 MeV γ-ray and for the related analyses presented in this Chapter. To develop an accurate model of the AmBe data spectrum, a clean calibration sample must first be selected. The selection criteria for NV events follow the standard trigger conditions, specifically a 3-fold coincidence within 300 ns.

Before fitting the energy spectra, two data quality cuts are applied. The first cut is based on the center-time versus area distribution, with the cut boundaries illustrated

in Fig. 4.1a. The second cut utilizes the spatial distribution of NV events, calculated as the area-weighted average over all PMTs detecting signals within the first 20 ns of the event. Fig. 4.1b shows the spatial distribution for a specific source position along with the applied cut boundaries. These cuts are designed to remove any accidental coincidence events caused by the PMT dark rate. After applying the cuts to both the source and background data, a bin-wise background subtraction of the energy spectrum is performed. The energy spectrum after applying the cuts and background-subtraction is presented in Fig. 4.2.

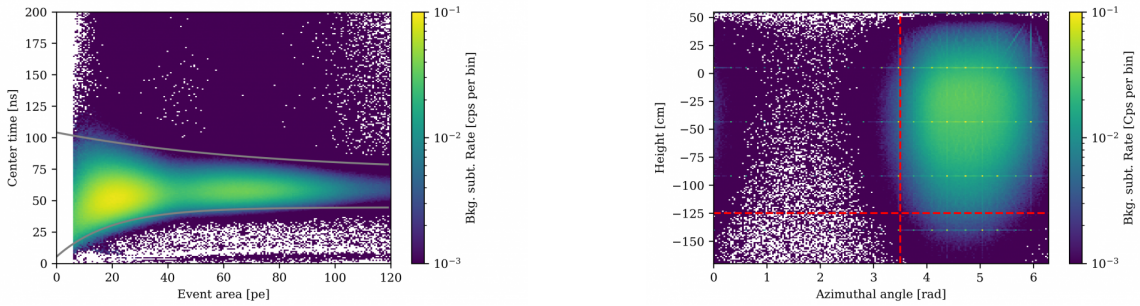

(a) (b)

Figure 4.1: (a) Background subtracted AmBe spectrum for the center-time cut space for the Top CW5d9 position. The gray lines indicate the boundaries of the center-time cut. (b) Background subtracted AmBe spectrum for the NV spatial cut for the Top CW5d9 position. The red dashed lines show the cut boundaries for the spatial distribution. The center-time cut shown in (a) has been applied to obtain this plot.

The background-subtracted spectrum is then fitted using the following function:

$$f(x;A_1, A_2, A_3, A_4, \mu_1, \mu_2, \mu_3, \mu_4, \sigma_{th}, \mu_{th}, s, o, c) = N_{cdf}(x; \mu_{th}, \sigma_{th}) \cdot \left(\sum_{i=0}^{4} N(x; A_i, \mu_i, \sigma(\mu_i, s, o)) + c \right) \tag{4.1}$$

Here $N(x; A_i, \mu_i, \sigma(\mu_i, s, o))$ represents a normal distribution, $N_{cdf}(x; \mu_{th}, \sigma_{th})$ is the cumulative distribution modeling the detector threshold, and c is added to take into account a flat background component. The width of each normal distribution is constrained by an energy resolution σ, defined as:

$$\sigma(\mu, s, o) = \sqrt{\mu \cdot s + o} \tag{4.2}$$

where μ is the position of the corresponding peak and s is left as a free parameter. This energy resolution model is based on the assumption that each peak follows Poisson statistics, with σ proportional to the square root of the number of detected photons

(μ). Due to the relatively high energy threshold of the water Cherenkov detector, an additional offset term (o) is introduced into the energy resolution.

The fitting procedure is carried out using the Least Squares method through the *iminuit* package, accounting for bin uncertainties estimated via Gaussian error propagation:

$$\Delta r_i = \sqrt{(\Delta N_{AmBe}/T_{AmBe})^2 + (\Delta N_{Bkg}/T_{Bkg})^2} \tag{4.3}$$

It is assumed that each bin in the calibration and background data follows Poisson statistics and that uncertainties in the total livetime are negligible. The best-fit results are shown in Fig. 4.2: the first peak corresponds to neutron captures on Hydrogen (2.2 MeV γ-ray), while the second is attributed to the 4.4 MeV γ-ray from Carbon de-excitation. The high-energy tail observed in the spectrum is likely due to neutron capture on ^{56}Fe, where the broadening of the peak is caused by a γ-ray cascade with a total energy of 7.6 MeV released during the capture process. In a water Cherenkov detector, where each accelerated electron has a threshold of about 264 keV in its kinetic energy, this results in a pronounced spread in the full-energy peak. Additionally, high-energy γ-rays may also arise from higher-energy Carbon de-excitation.

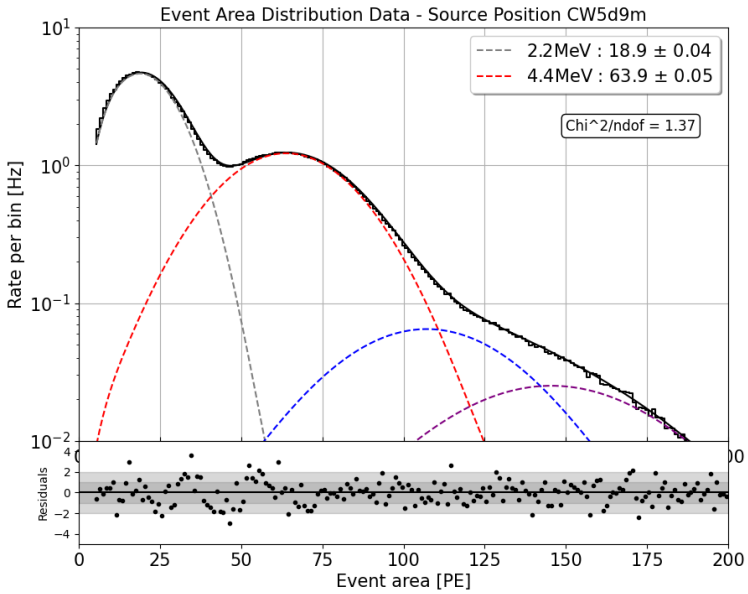

Figure 4.2: Best fit of the NV AmBe energy spectrum taken at the Top CW5d9m source position. The bottom panel shows the fit residuals. The individual fit components are shown in different colors.

Fig. 4.3 presents the absolute neutron rate and the fraction of high-energy neutron capture events producing more than 60 PE, specifically from neutron captures on ^{56}Fe.

The absolute rate of detected neutrons increases as the source moves farther from the TPC, as the solid angle of the NV around the source position grows. However, the rate of neutron captures on heavier nuclei decreases, as fewer neutrons are able to reach the cryostat due to the increased distance from the source.

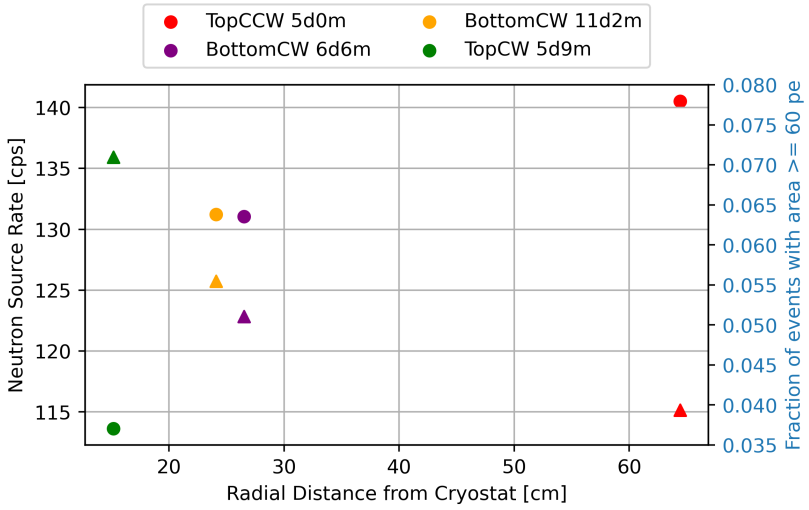

Figure 4.3: Detected neutron rate (circles) and fraction of high-energy neutron capture events (triangles) as a function of the radial distance from the cryostat.

In summary, the analysis demonstrates the effectiveness of the selected model for describing the AmBe spectrum across various source positions, providing key insights into the energy spectrum's components and their corresponding physical processes.

4.2 AmBe source characterization

This fitting model has been applied to other source positions, yielding consistent results. Despite the model's adequate performance, achieving a highly accurate analytical fit remains challenging due to the high statistical precision of the calibration data. The same model has also been used to fit the MC-generated AmBe spectrum, as shown in Fig. 4.4b. MC data are produced separately for "neutron-only emission" and "neutron with γ emission" and are combined afterwards assuming a 50% ratio between the two processes. This ratio value is thoroughly studied for the position Bottom CW6d0, at the mid-distance between the cryostat and the NV walls, since it provides the cleanest sample of neutron captures in water, as $> 90\%$ of emitted neutrons from this position get captured before reaching the cryostat.

We compared the fitted data in Fig. 4.4a with the fitted MC generated events in Fig.

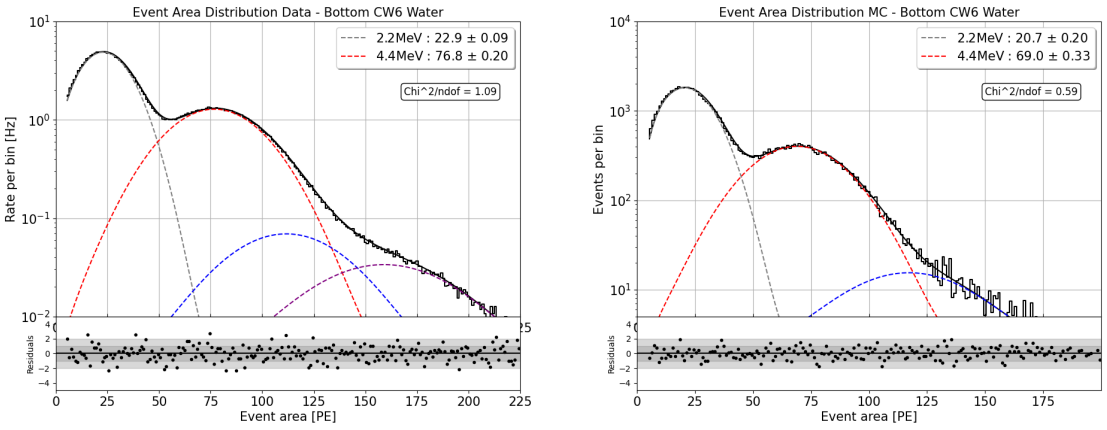

(a) (b)

Figure 4.4: (a) Best fit of the NV area spectrum produced by the AmBe source at the Bottom CW6d0 position. (b) Best fit of the NV area spectrum from Montecarlo simulation in the Bottom CW6d0 source position. The bottom panel shows the fit residuals. The individual fit components are also shown in different colors.

4.4b: the idea was computing the ratio of the areas relative to the first two peaks related to the distribution of the neutron captures on Hydrogen (2.2 MeV γ-ray) and to the 4.4 MeV γ-ray from Carbon de-excitation, respectively called $Area1$ and $Area2$.

Then we generated various MC spectra by combining the "neutron-only emission" and "neutron with γ emission" spectra with different proportions, from 30:70 to 70:30, to find the best match in the ratio of the peaks $Area1/Area2$ with the data observed in the AmBe calibration. In Fig. 4.5 is shown the region where the intersection between MC and data values happens: MC points are the blue dots, each one with the corresponding uncertainty; the red line represents the value of the area ratio for the data. Based on the best MC-data matching, we conclude that the AmBe source emits neutrons without accompanying 4.4 MeV γ in 56% of the cases.

4.3 Neutron tagging efficiency

Neutrons originating from materials within the detector present a significant challenge to WIMP Dark Matter searches. These neutrons elastically scatter off detector target nuclei in the same way as WIMPs, resulting in Nuclear Recoils that are indistinguishable from potential DM signals. In the XENON1T experiment, neutron signals were distinguished from DM by identifying multi-scatter events where two or more interactions occurred within the detector's active volume. However, due to the significant mass difference be-

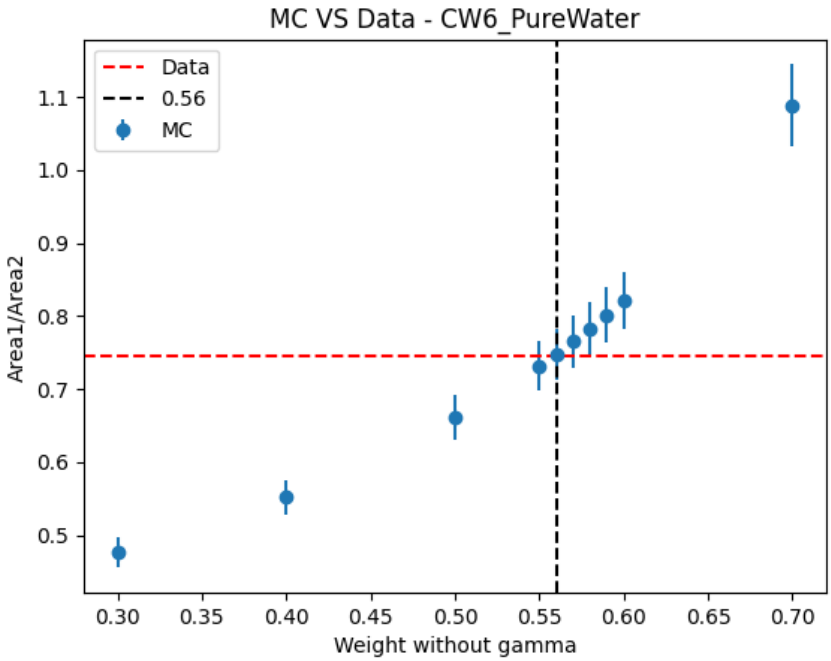

Figure 4.5: Ratio of the areas of the 2.2 MeV and 4.4 MeV peaks in the NV area spectrum for different fractions of neutrons with accompanying gamma assumed in the MC simulation of the AmBe source at the Bottom CW6d0 position. The ratio observed in real data is shown with the dashed red line. The best MC-data match is found for 56% of neutrons emitted without an accompanying gamma.

tween Xenon and neutrons, many neutrons simply backscatter off Xenon nuclei and exit the sensitive volume without undergoing a second interaction. This is why XENONnT was designed with a Gd-loaded water Cherenkov Neutron Veto, which tags neutrons in the water volume surrounding the cryostat.

This section focuses on estimating the neutron tagging efficiency of the NV, a crucial parameter that quantifies the fraction of dangerous neutron signals in the time projection chamber that are tagged by the NV. Neutron tagging is achieved through delayed coincidence with a 2.2 MeV signal from neutron capture on Hydrogen (or higher energies, for captures on Gd, when present). The neutron tagging efficiency, denoted as ζ, for a selected NR single-scatter sample, is defined as:

$$\zeta = \frac{\text{Number of neutron-capture events detected in the NV at a specific threshold}}{\text{Number of Nuclear Recoil single scatter events}} \tag{4.4}$$

The efficiency calculation is based on the AmBe calibration discussed in detail in the previous chapter. The pattern of the events under study is schematized in Fig. 4.6,

and the signature matches the one expected from the neutron background, with the distinction being the neutron origin and the additional 4.4 MeV γ-ray signal detected by the NV. According to the definition of the tagging efficiency, it relies on the selection thresholds set for NV events and the length of the time window where delayed coincident signals are sought. These parameters must be optimized to balance between achieving the desired tagging efficiency and minimizing the loss of livetime in the TPC due to accidental coincidences with background events in the NV.

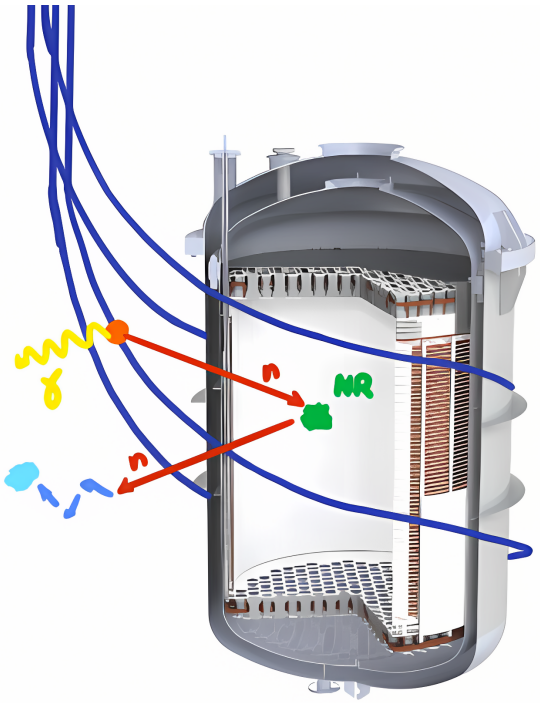

Figure 4.6: Schematic of the method used to measure the neutron tagging efficiency with the AmBe calibration. We search for the time-coincidence between the 4.4 MeV gamma in the NV (yellow) and the S1 signal of the neutron-induced NR in the TPC (green), then we look for the 2.2 MeV gamma of neutron capture in the NV (light blue).

NRSS events were selected by requiring a tight time-coincidence between the 4.4 MeV γ-ray signal recorded by the NV and the NR S1 signals detected in the TPC within a 400 ns window. This ensures the selection of well-reconstructed NR S1 signals with 99.9% purity. Additional data quality cuts were applied to ensure that only well-reconstructed single-scatter events were selected. The NR signals used for the NV tagging efficiency calibration were further constrained within the 90% contour of the NR band. The selected data are shown in Fig. 4.7.

The potential neutron capture signals in the NV related to the NR interactions were identified using a dedicated plugin, inherited from the base coincidence framework used

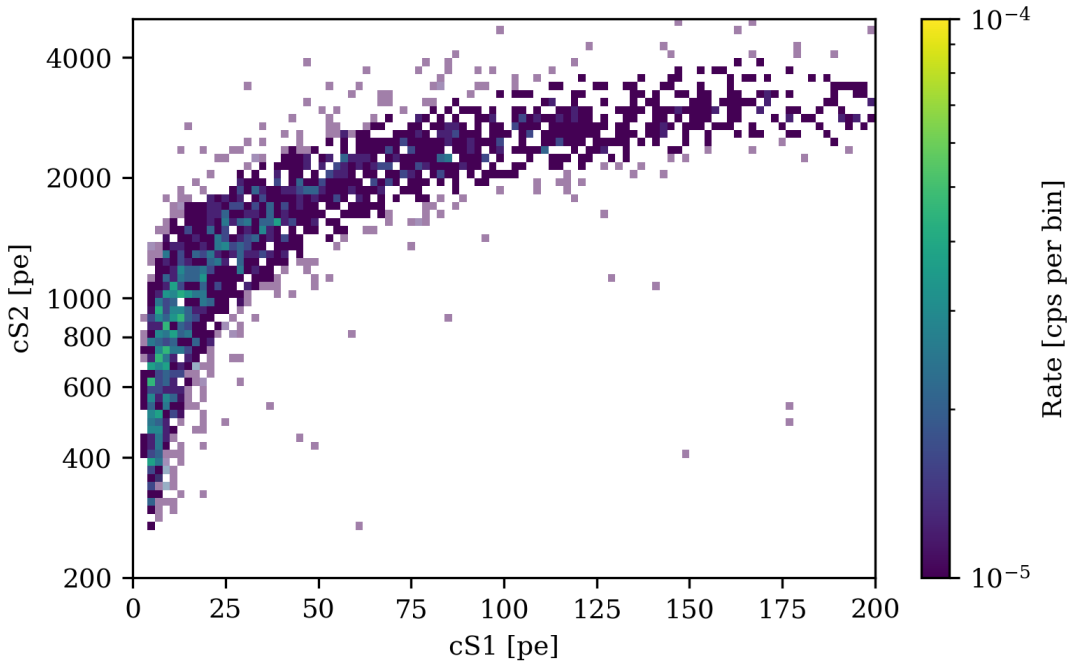

Figure 4.7: Distribution of the TPC signals (cS1, cS2) of all the NR single-scatter events (partially transparent) and of those events within the 90% contour of the NR band (fully colored).

for event building. The coincidence was built between the time of the S1 signal (which acted as the trigger) and the NV event within a time window spanning from -1000 μs to 2000 μs, as depicted in Fig. 4.8. The resulting spectrum exhibited a well-known structure, with a pronounced peak at the center followed by an exponentially decreasing distribution, set atop a flat plateau.

The central peak corresponds to 4.4 MeV γ-rays detected in the selected time window, with smaller peaks appearing near 2 μs and 8 μs, likely due to events from PMT afterpulses. The exponential distribution is associated with radiative neutron capture signals, particularly on Hydrogen. The decay constant of this distribution is shaped by the effective capture time of all isotopes that capture neutrons and generate detectable signals within the NV, including materials such as stainless steel. The plateau is attributed to random coincidences between the two detectors.

To estimate the number of neutron capture signals detected by the NV, a comparison is made between events in the purple region (30 μs to 630 μs, mostly populated by neutron capture events) and those in the orange reference region (-1000 μs to -400 μs, dominated by accidental coincidences). The boundaries of the purple region were selected

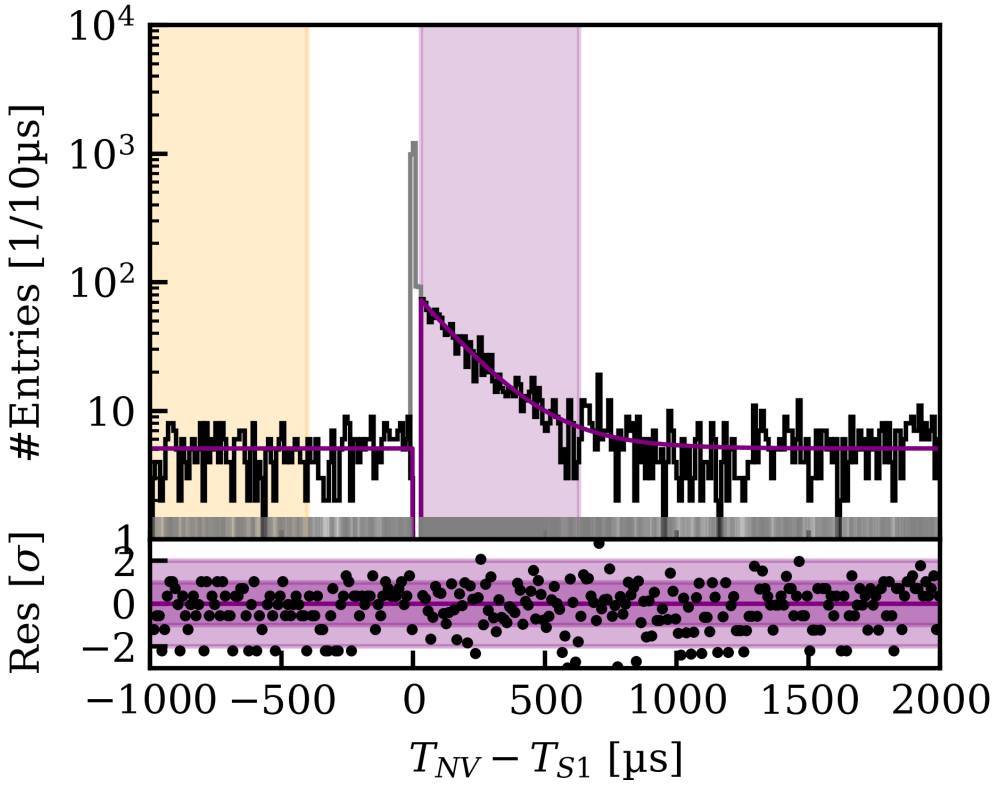

Figure 4.8: Distribution of the time difference between NV events and the triggering single-scatter NR S1 signal in the TPC. The small gray vertical lines indicate the individual time differences. The purple line shows the best fit of the time distribution. The purple and orange areas indicate the region of interest and background reference regions explained in the text. The black histogram shows a binned representation of the data whereas the gray-shaded part indicates bins excluded from the fit region. The bottom panel shows the residuals of the best fit with the binned data.

to maximize the detection of neutron capture signals while avoiding contamination from afterpulses occurring between 0 μs and 30 μs. The area distribution of the selected events is shown in Fig. 4.9, where the events in the purple region show a peak structure, aligning with the Hydrogen neutron capture peak as deduced from the previous fit.

By integrating the counts within the purple region and subtracting those from the orange background reference, the number of tagged NR single-scatter signals is determined. This calculation informs the neutron tagging efficiency for the chosen veto window of [30 μs, 630 μs]. However, for scientific data analysis, this window may not be entirely suitable, as many capture events are known to occur within the first 30 μs. Additionally,

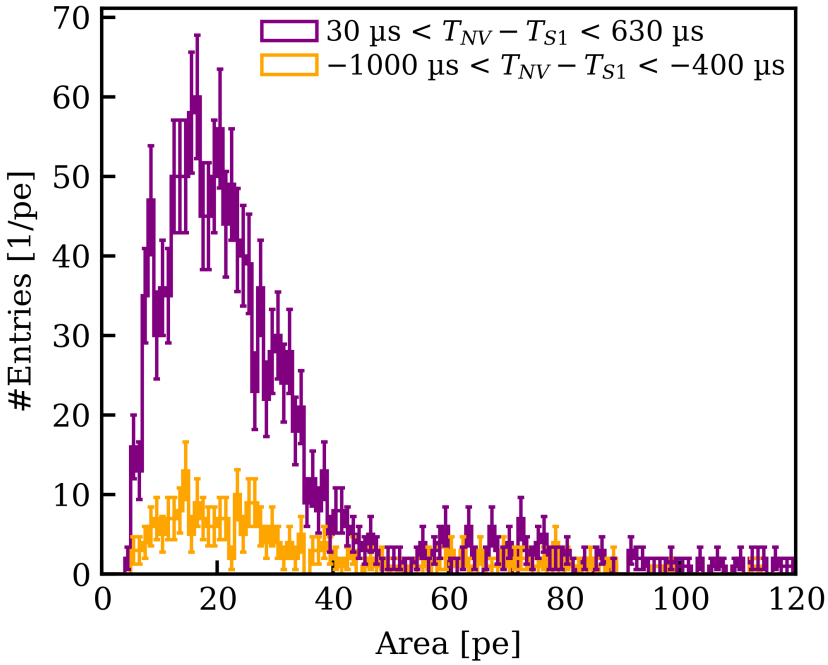

Figure 4.9: Event area distribution for the neutron capture signal (in purple) and background (in orange) reference region of Fig. 4.8. The error bars indicate the statistical uncertainties in each bin.

the total duration of the window during the WIMP search is shorter than 600 μs, to minimize the detector dead-time.

To accurately compute the tagging efficiency, the veto window correction factor (ϵ_{TW}) must be calculated, accounting for the exponential distribution decay constant associated with radiative neutron capture. This is estimated by fitting the time distribution (excluding the γ-peak and afterpulse region) using an unbinned log-likelihood method, shown in Fig. 4.10. The resulting best-fit decay constant is $\tau_C = 180 \pm 8$ μs, slightly lower than the expected value of ~ 200 μs for pure water, likely due to neutron capture on other isotopes like ^{56}Fe present in the cryostat materials.

The correction factor ϵ_{TW} is derived by comparing the fraction of the exponential distribution covered by the veto window to the full time range used for neutron capture detection:

$$\epsilon_{\mathrm{TW}} = \frac{\exp_{cdf}(t_1, \tau_{\mathrm{C}}) - \exp_{cdf}(t_0, \tau_{\mathrm{C}})}{\exp_{cdf}(630\mu s, \tau_{\mathrm{C}}) - \exp_{cdf}(30\mu s, \tau_{\mathrm{C}})} \tag{4.5}$$

where t_0 and t_1 denote the start and end of the veto window used for NV tagging in the science run.

Lastly, a geometrical correction factor (ϵ_{geo}) accounts for the spatial distribution of neutron sources intrinsic to the TPC. This factor was estimated using GEANT4

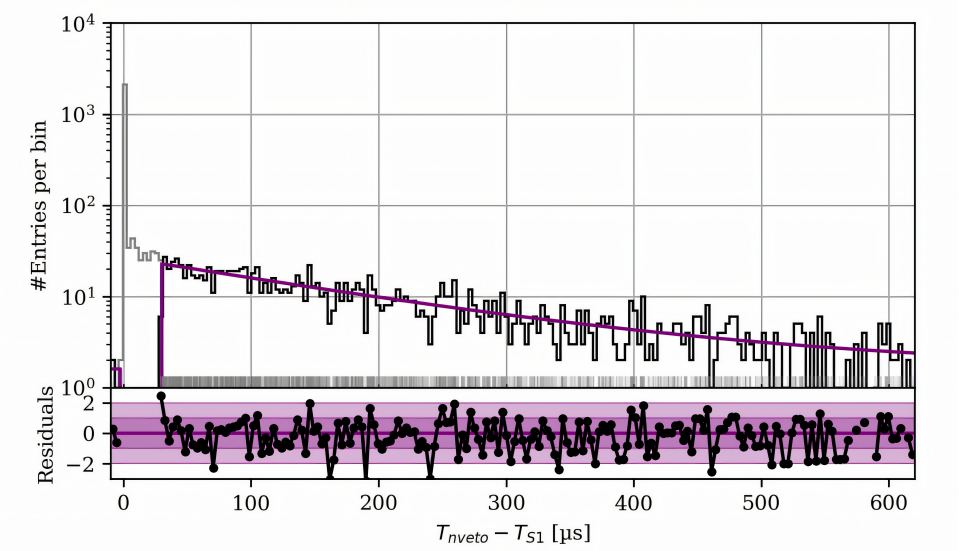

Figure 4.10: Best fit of the hit time distribution in AmBe calibration runs, zoomed in the [0, 600] μs region. The gray part of the histogram indicates the data in the initial time region excluded from the fit represented by the purple line. The bottom panel shows the residuals of the fit.

simulations and compares the tagging efficiency for background neutrons to that for neutrons from the AmBe calibration. Simulations predict a tagging efficiency of (71 ± 1)% for an infinitely long tagging window, which aligns with the (70 ± 3)% observed in data for a 1200 μs tagging window. The correction factor ϵ_{geo} is determined to be 1.01 ± 0.02, indicating that the spatial distribution of neutron sources has minimal impact on overall tagging efficiency.

After applying all corrections, the neutron tagging efficiency is estimated using the equation:

$$\zeta\left(t_0, t_1\right) = \epsilon_{\mathrm{vw}}\left(t_0, t_1\right) \cdot \epsilon_{geo} \sum_{i=A_{\mathrm{th}}}^{\infty} n_{\mathrm{sig},i} - n_{\mathrm{bkg},i} \tag{4.6}$$

where $n_{sig,i}$ and $n_{bkg,i}$ represent the number of neutron capture signals and background signals found in the i_{th} bin of Fig. 4.9, respectively, for a specific n-fold coincidence requirement and an event area threshold A_{th}.

The tagging efficiencies for 250 μs and 600 μs windows are presented in Fig. 4.11, using a 5-fold PMT coincidence requirement for different NV signal area thresholds. During Science Run 0, a neutron-tagging window of 250 μs with a 5 PE area threshold and a 5-fold PMT coincidence was used, achieving a tagging efficiency of (53 ± 3)% with a 1.6% livetime loss. For a 600 μs window, the efficiency increased to (68 ± 3)%. The decision to use a shorter tagging window reflects a trade-off between detector deadtime

and tagging efficiency.

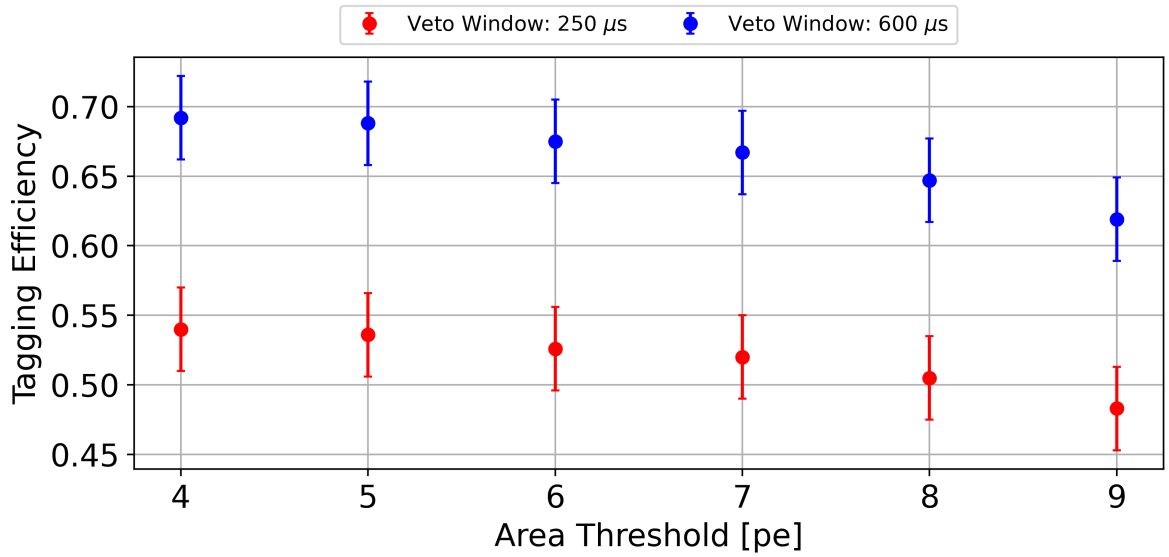

Figure 4.11: Neutron tagging efficiency of the NV in SR0. The red and blue data show the tagging efficiency for a 250 μs and 600 μs veto-window, respectively. In both cases, it was required that at least 5 PMTs contribute to a NV event.

4.4 Gd-doped Neutron Veto phase

4.4.1 Gadolinium insertion in XENONnT

The key improvement between SR0/SR1 and SR2 was the addition of Gd-Sulfate Octahydrate (GdSO) to the water tank, converting the NV into a Gd-water Cherenkov detector. The target Gd concentration was gradually reached. This section covers the insertion process, salt dissolution and the subsequent performance of the NV with Gd.

As described in Section 2.2.4, during SR1 the Gd-Water Purification System was commissioned and tested using demineralized water. From July 2022, the 700 tons of water in the XENONnT tank, typically treated by the WLP, was circulated through the GdWPS with stable pressure, flow and temperature. Water purified in the GdWPS was reintroduced to the XENONnT water tank through two inlet points (see Fig. 4.12), with a consistent flow rate. Weekly reflectivity monitor runs confirmed stable optical properties of the water.

In January 2023, GdSO was first added to the GdWPS in closed loop (not connected to the main water tank), with 15 kg of salt dissolved into $\sim$ 3 tons of water, resulting

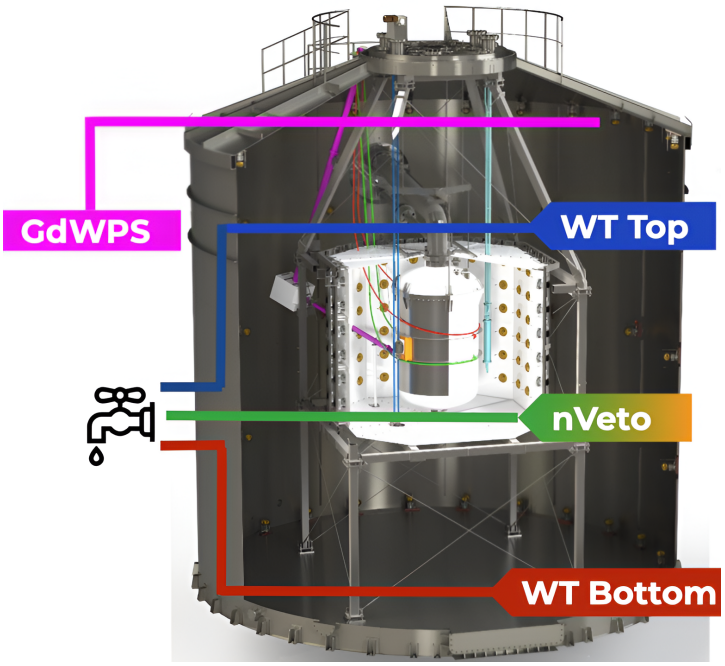

Figure 4.12: CAD rendering of the water tank and NV with the sampling points where the Gd-water solution is extracted for further analyses. The 4 sampling points are reported with different colors. For the NV port there are two colors indicating that for those samples the measurements of the concentration are performed with two different methods (conductivity and ICP-MS). The GdWPS line is positioned on the top of the water tank since the solution flows in the plant from that spot.

in a concentration of 5000 ppm, the target level. The system was operated in this configuration for several months to optimize Gd separation efficiency at the nanofiltration stages. In June 2023, a reduced concentration of 500 ppm (10 times lower than nominal) was chosen for the first introduction of GdSO into XENONnT, as a risk mitigation precaution. At this concentration, $\sim$ 60% of neutron captures were expected to occur on Gd. This configuration was thus reproduced also in the GdWPS, which operated steadily at the reduced concentration since then, with minimal GdSO loss.

The insertion of GdSO into the water tank began in October 2023. Initially, 1.5 kg of GdSO, previously used in a closed loop, was added to the tank, split between the two inlet points. Immediately, the NV data rate increased by $\sim$ 50%, likely caused by an increase in light seen by the PMTs rather than background events. The rate continued rising until October 12, when the input line to the NV was closed, stabilizing the situation after 7-10 days. Subsequent GdSO insertions only affected the bottom inlet of the water tank, producing smaller increases in the NV data rate.

The GdSO concentration in the water tank was monitored by sampling at various locations, including the NV floor (as shown in Fig. 4.12). Concentration was measured directly via ICP-MS and indirectly by conductivity. The precise cause of the increased data rate during GdSO insertions is still unclear: the most likely hypothesis, under study in a dedicated setup at LNGS, is light production due to changes in GdSO concentration, possibly caused by pH variations during the transient until the salt is uniformly dissolved in the medium.

To ensure that these operations did not degrade NV performance, water transparency and wall reflectivity were regularly monitored using the reflectivity monitor whose trend is shown in Fig, 4.13. Any drop in optical performance, indicated by changes in the exponential distribution parameter (τ), was temporary and improved after a few days of water recirculation through the GdWPS. However, after a significant GdSO injection in December, the optical properties gradually worsened, resulting in an overall decrease in light collection efficiency of about 20%.

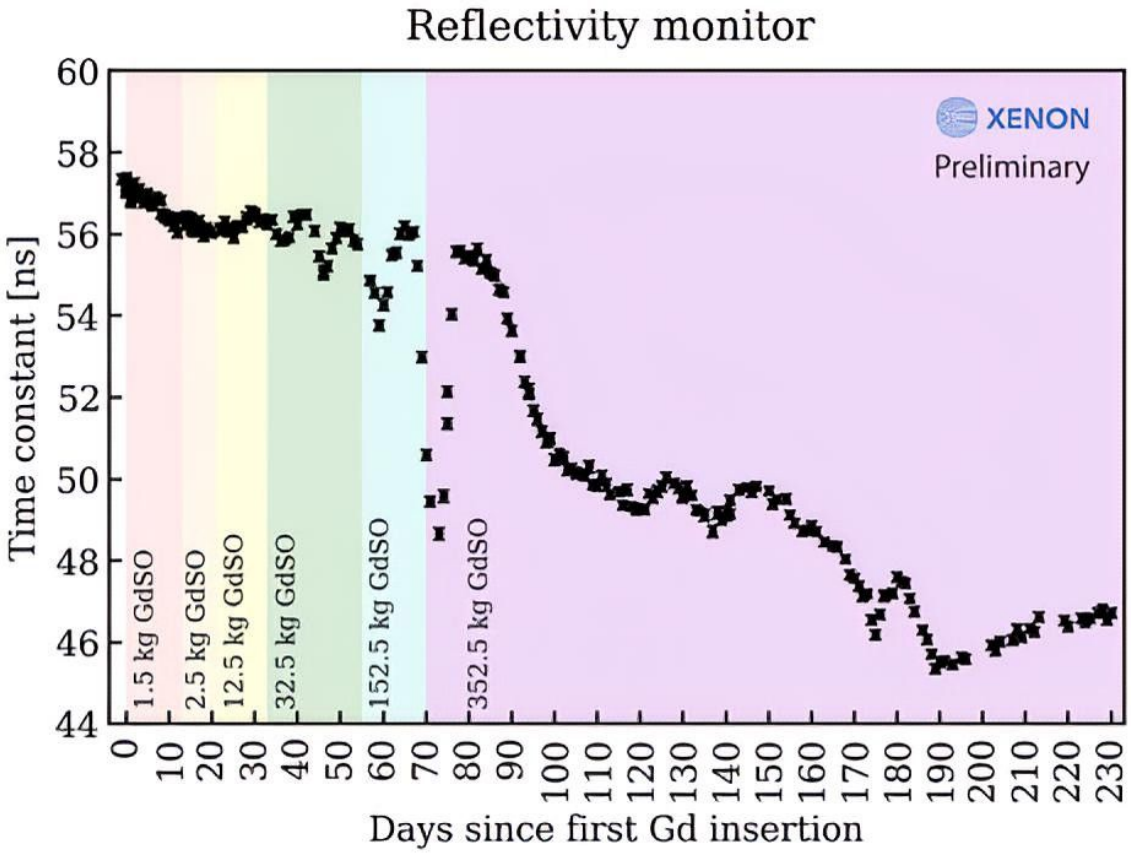

Figure 4.13: Evolution of the average time parameter τ estimated from the fit of the time distribution of the daily reflectivity monitor runs taken during the Gd-loading operation. Each GdSO insertion step is marked by a different color.

4.4.2 Analysis of Neutron Veto performance with Gd

To monitor the effects of GdSO in water, regular AmBe calibrations were performed before, during and after the Gd insertion period. These calibrations measured the charge spectra with the source consistently positioned at the center of the NV (in position Bottom CW6d0m). As shown in Fig. 4.14, the spectrum observed in the NV was analyzed using the same model previously described, with an additional Gaussian component to account for neutron captures on Gd (indicated by the red solid curve). No significant changes in the charge spectra were observed until a Gd concentration of 50 ppm was reached, corresponding to 32.5 kg of Gd salt, when the first captures on Gd were detected.

By monitoring the position of each peak over time, particularly those associated with the 2.2 MeV and 4.4 MeV lines, a direct measurement of the reduction in light collection efficiency was obtained. Additionally, the area under each Gaussian curve provided insights into the amount of captures on both H and Gd. The results are shown in Fig. 4.15: in the top panel (Fig. 4.15a), the decrease in optical properties is reflected by the shift in the peak positions (for both the neutron capture on H and the γ from de-excitation of ^{12}C). The optical performances of the system are kept under control by periodic replacement of the particle filters in the GdWPS. At present, the light collection efficiency at 500 ppm GdSO is about 80% of the one measured with demineralized water, as it was expected by the insertion of the salt inside the previously ultra-pure water. However, the number of events lost due to the 5 PE threshold remains minimal, at only a few percent. In the bottom panel (Fig. 4.15b), the capture rates on H, Gd, and the total are displayed. The overall neutron capture rate remains largely unchanged, increasing only slightly, as most neutron capture events in the center of the NV were already detected even with demineralized water. As the GdSO concentration increases, the data clearly shows that most events shift from H captures to Gd captures.

To finally measure the neutron tagging efficiency with Gd, an AmBe calibration was conducted with the source positioned near the cryostat (Top CW7d8), closely simulating the neutron background from this detector part. Fig. 4.16 compares directly the spectra in NV for pure water and Gd-doped water with the current concentration of GdSO (500 ppm), highlighting the improvement in the number of neutron captures after Gd insertion: approximately 60% of them now occur on Gd rather than H, as also shown in Fig. 4.15b. The results, analyzed using the same method described earlier, showed that the neutron capture time decreased from (163 $\pm$ 3) μs in SR1 (demineralized water) to (75 $\pm$ 2) μs in SR2 (Gd-water), as illustrated in Fig. 4.17. The observed neutron tagging efficiency for a 5-fold PMT coincidence is shown in Fig. 4.18 as a function of the area threshold (in PE), for AmBe data in the position Top CW7d8. With the current configuration, we observe an improvement of more than $\sim$ 24% (absolute value) in the tagging efficiency: it reached 77% with 500 ppm of GdSO (red), compared to 53% with demineralized water (blue) in SR0, with a coincidence window of 250 μs. With these

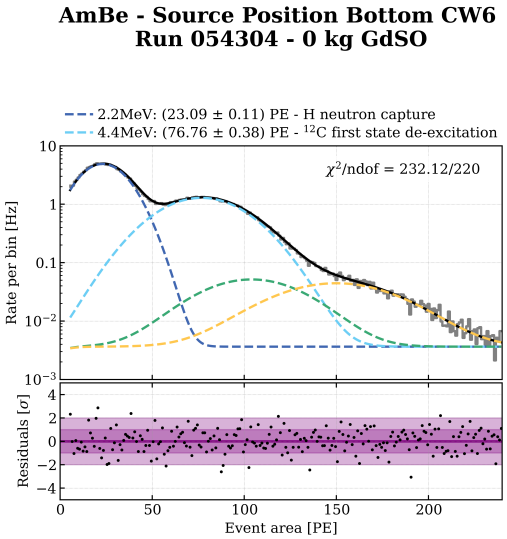

(a) Demineralized water

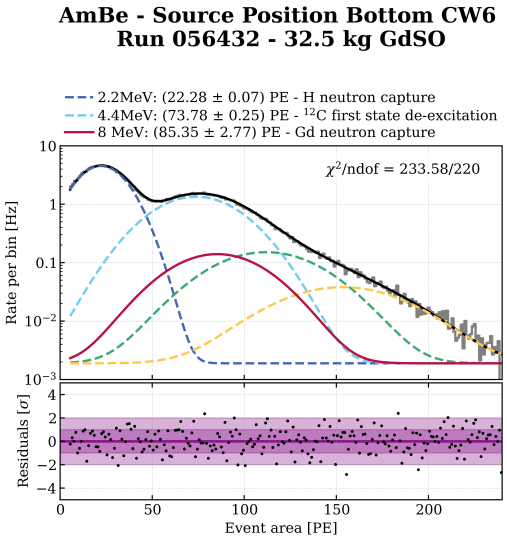

(b) GdSO Concentration: 50 ppm

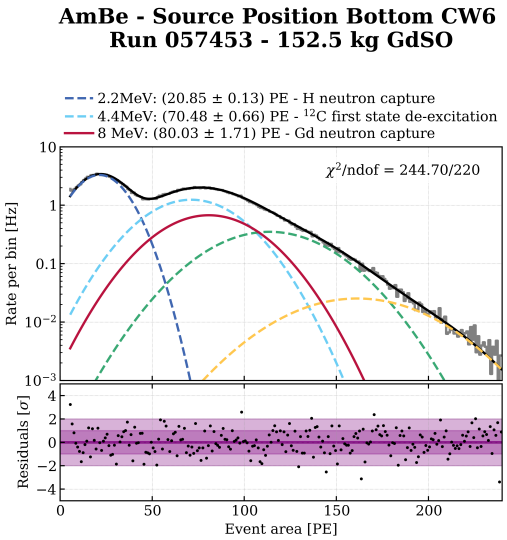

(c) GdSO Concentration: 200 ppm

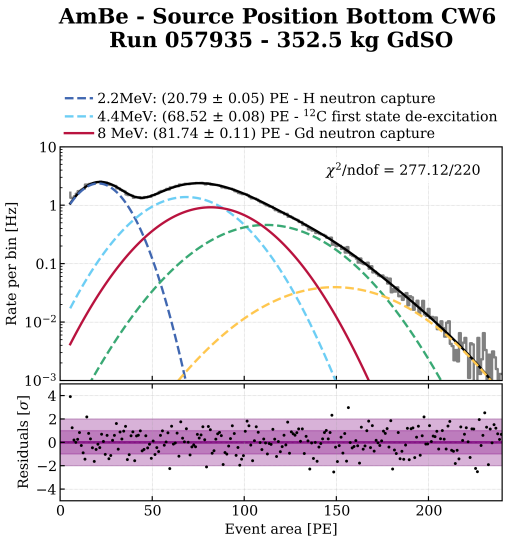

(d) GdSO Concentration: 500 ppm

Figure 4.14: Event area spectrum in the NV during AmBe calibration for different GdSO concentration: (a) Demineralized water (as the one already shown in Fig. 4.2); (b) 32.5 kg of GdSO (corresponding to $\sim$ 50 ppm); (c) 152.5 kg of GdSO (corresponding to $\sim$ 200 ppm); (d) 352.5 kg of GdSO (corresponding to $\sim$ 500 ppm). The bottom panels of all the plots show the fit residuals. The individual fit components are also shown in different colors. For all the plots with Gd an additional Gaussian component (shown in red solid line) has been added to take into account the contribution of neutron captures on Gd.

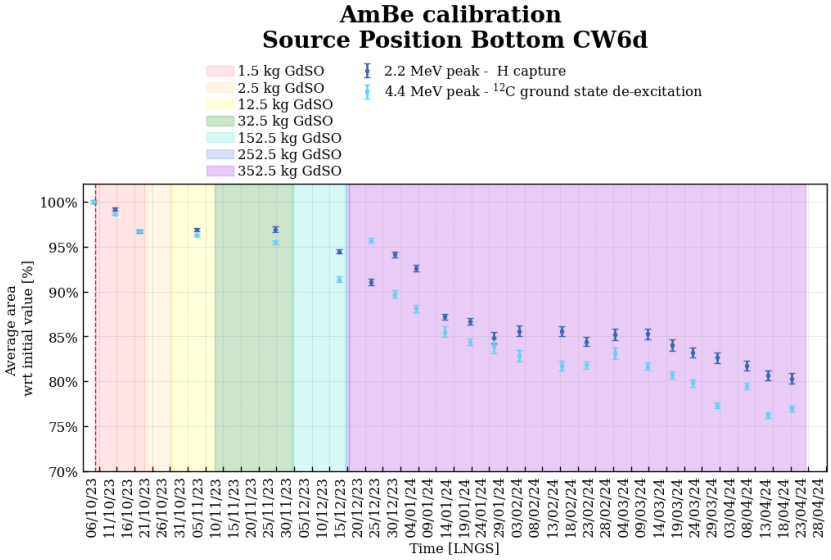

(a)

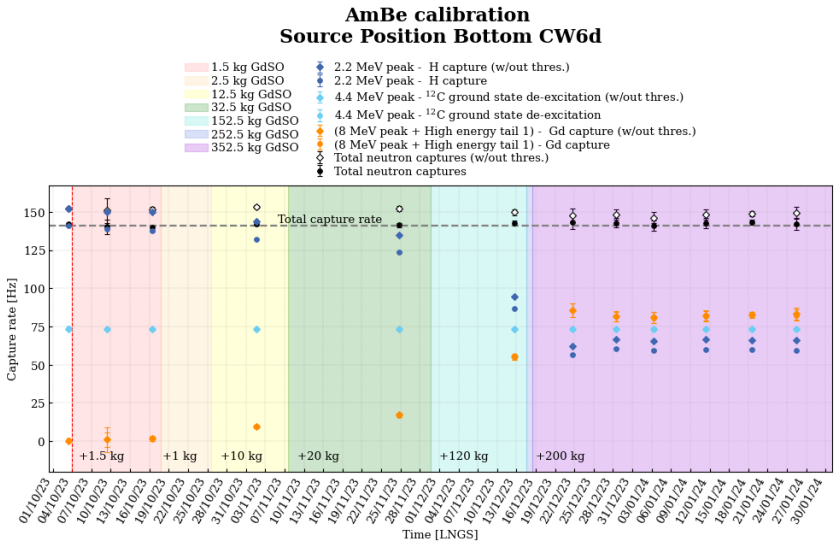

(b)

Figure 4.15: (a) Time evolution of the mean values of the Gaussian corresponding to H captures and ^{12}C de-excitation, normalized to their initial value. (b) Time evolution of the rate of n capture for H (blue), Gd (brown) and the ^{12}C de-excitation (light-blue). The open diamonds represent the values obtained without considering the 5 PE threshold, while the solid points show the results above it. Also, the total number of captures (the sum of the H and the Gd captures) is shown for reference.

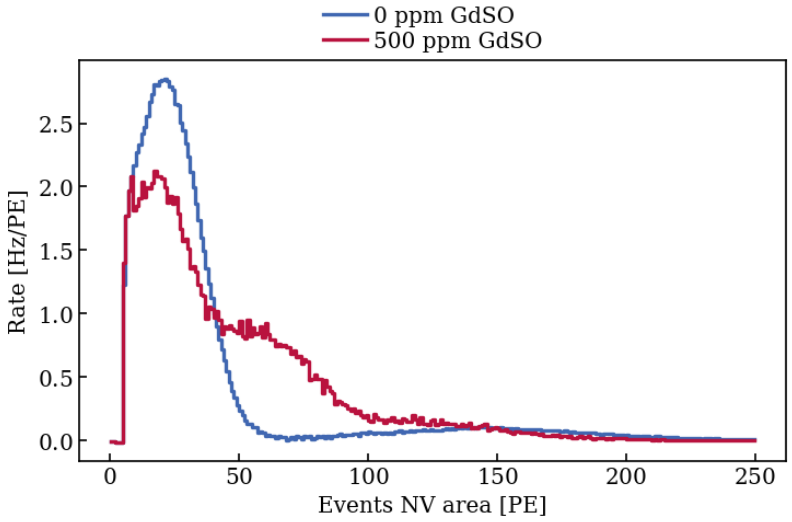

Figure 4.16: Event area distribution of AmBe calibration after the 4.4 MeV γ subtraction (this contribution has been estimated with the usual fit described in Section 4.1), for demineralized water (blue) and 500 ppm GdSO-water solution (red).

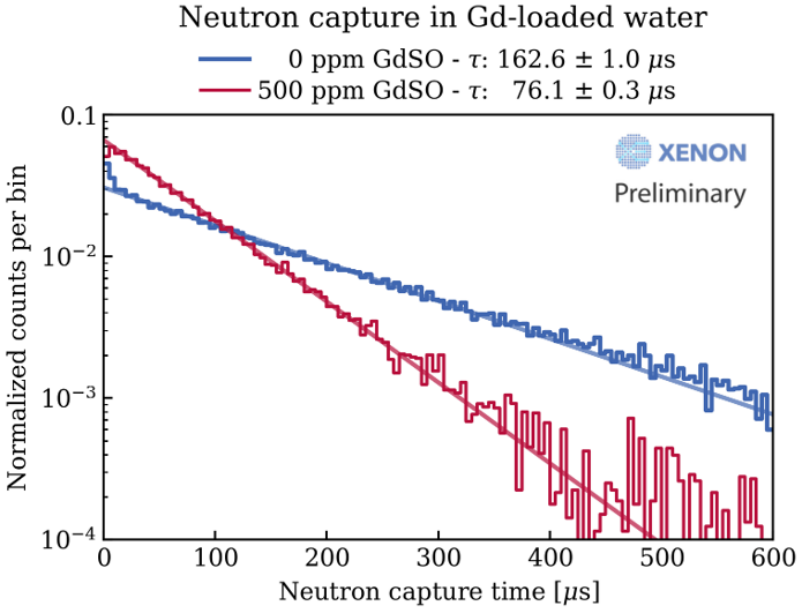

Figure 4.17: Time distribution of the neutron captures with 0 ppm and 500 ppm of Gd sulphate concentration.

results, the neutron background in SR2 is reduced by a factor 2 with respect to the previous Science Runs with demineralized water.

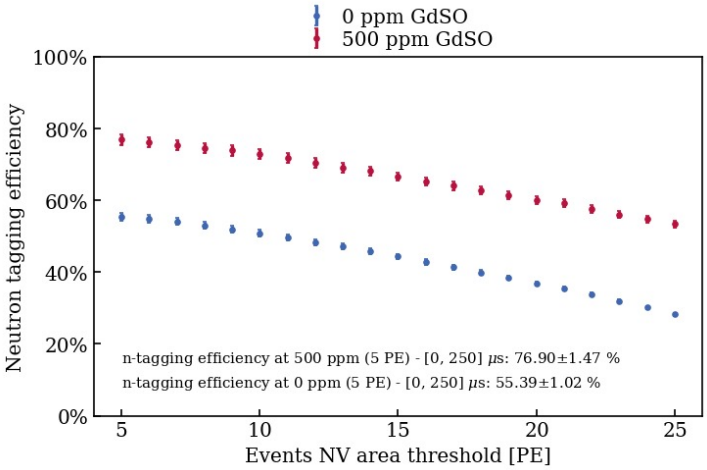

Figure 4.18: Neutron tagging Efficiency measured with an AmBe calibration with the source positioned close to the cryostat (Top CW7d8). The tagging efficiency is displayed here for the time window of [0, 250] μs, the one used in Science Run 0 analysis (Section 4.3).

4.5 Comparison between data and Montecarlo

An important physical aspect regards how data and MC compare each other because this is fundamental in validating the models we use and in making predictions on NV performance.

NV event area spectrum

A first MC-data comparison is presented in Fig. 4.19 where we show a comparison between data (in blue) and MC (in red) AmBe spectra in the NV for the position Bottom CW10d3 applying only the NV selection cuts (area $\geq$ 5 PE and PMT multiplicity $\geq$ 5). The MC spectra are scaled according to the predicted rate of the AmBe source of (159 $\pm$ 4) neutrons/s and assume 50:50 ratio for neutron emission with and without 4.4 MeV gamma. The two curves match well as can be seen directly from the plot.

NV event rate

In Table 4.1, we compare the rate of observed events in the NV with the AmBe source at three positions: Top CW7d8, Bottom CW10d3, and Bottom CW6d0.

Specifically, the numbers from real data are estimated as follows:

1. NV spectrum after selection cuts (area $\geq$ 5 PE and PMT multiplicity $\geq$ 5) is considered.

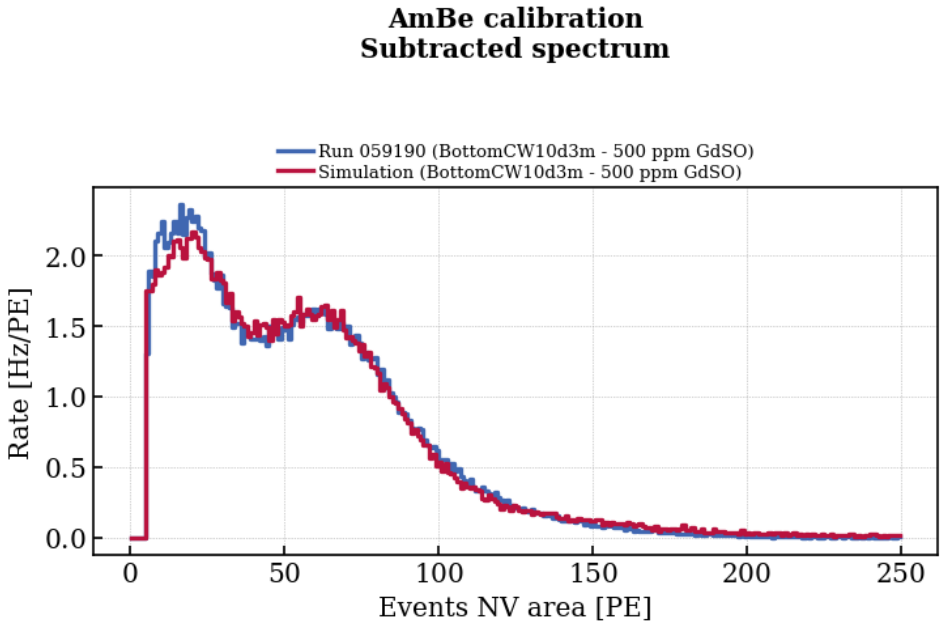

Figure 4.19: Comparison of the event area spectra obtained from data (blue) and MC predictions (red) for the AmBe source at the position Bottom CW10d3m with 500 ppm GdSO concentration.

Source	Pure water		500 ppm GdSO		Relative increase	
	Data	MC	Data	MC	Data	MC
Top CW7d8	95.6 ± 0.2 Hz	114 Hz	106.3 ± 0.4 Hz	128 Hz	+11.2%	+12.5%
Bottom CW10d3	91.3 ± 0.9 Hz	115 Hz	100.2 ± 0.9 Hz	128 Hz	+9.7%*	+11.5%
Bottom CW6d0	142.1 ± 0.4 Hz	154 Hz	144.1 ± 0.3 Hz	159 Hz	+1.5%	+3.6%

Table 4.1: Event rate induced by the AmBe calibration source in the NV, as observed in real data and simulated via GEANT4. The MC rate assumes a source activity of 159 emitted neutrons per second. The last two columns show the relative increase of the NV event rate after the insertion of GdSO at 500 ppm concentration. The value for data in pure water in the position Bottom CW10d3 was actually measured with a 50 ppm GdSO concentration, but the difference from the pure-water case is negligible.

2. The NV background spectrum is subtracted.

3. The Gaussian contribution of the 4.4 MeV gamma fitted to AmBe data in pure

water is subtracted.

4. The number of residual events in the spectrum is computed.

To get the corresponding information from MC, we considered the simulation of AmBe neutrons without the 4.4 MeV gamma and then computed the expected rate based on the estimated source rate of 159 neutrons/s. The small discrepancy is under study yet, to deepen the knowledge oh this phenomena and to characterize better the AmBe source, however there is a consistent agreement in the rate improvement after Gd insertion for all the positions.

Neutron capture lifetime

The neutron capture lifetime is the time constant of the distribution of the time elapsed from the emission of a neutron to its capture. From simulations, this is obtained by fitting the time distribution of neutron capture events selected from GEANT4: Fig. 4.20 reports the estimated neutron capture lifetime from GEANT4 for different conditions of GdSO concentration in the detector, precisely with 0 ppm and the current 500 ppm.

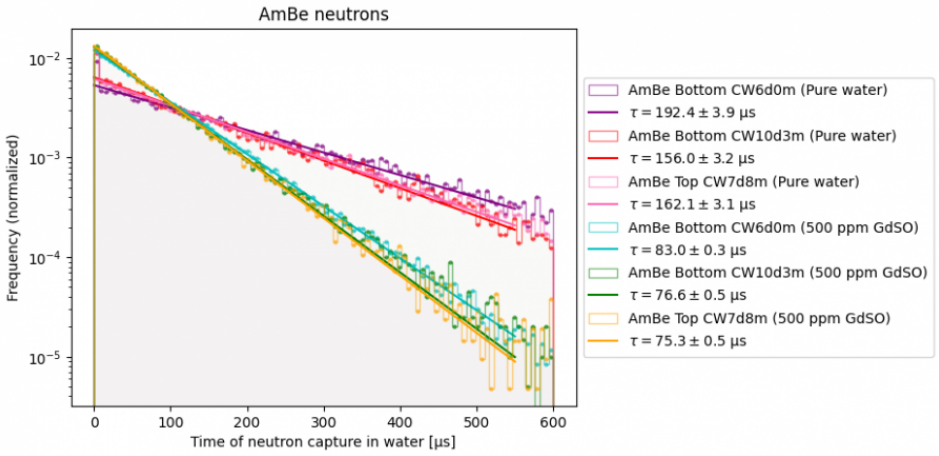

Figure 4.20: Time distribution of the simulated neutron captures, identified by their flags in the MC. The distribution is shown for several positions and and in different conditions (pure water and 500 ppm GdSO concentration); with the current Gd concentration it is expected to halve the average capture time (estimated here with an exponential fit of the distribution).

In Tab. 4.2 the average neutron capture time obtained from data and MC is compared. The results show a good agreement between data and MC both in pure water and Gd-doped water and at the different AmBe source positions considered. The simulated neutron capture lifetime for radiogenic neutrons emitted from the cryostat is also

Neutron source	GdSO concentration	MC	NV data
Cryostat	5000 ppm	17 ± 1 μs	
Bottom CW6d0	500 ppm	83.0 ± 0.3 μs	81.3 ± 0.1 μ s
Bottom CW10d3	500 ppm	76.6 ± 0.5 μs	76.7 ± 0.3 μs
Top CW7d8	500 ppm	75.3 ± 0.5 μs	76.1 ± 0.3 μs
Cryostat	500 ppm	78 ± 1 μs	
Bottom CW6d0	0	192 ± 4 μs	201.9 ± 0.5 μs
Bottom CW10d3	0	156 ± 3 μs	n/a (150.9 ± 0.9 μs @ 50 ppm GdSO)
Top CW7d8	0	162 ± 3 μs	163.7 ± 0.9 μs (140.0 ± 0.9 μs @ 50 ppm GdSO)
Cryostat	0	168 ± 2 μs	

Table 4.2: Comparison between data and MC of the average neutron capture time, computed by fitting the time distribution of time elapsed from the neutron emission and the subsequent NV signal due to the neutron capture.

reported. Their capture lifetime is significantly smaller than that of AmBe neutrons emitted from the position Bottom CW6d0, far away from the cryostat. The latter are almost exclusively captured in water, while neutrons emitted close to the cryostat suffer from a fraction of captures happening in the Cryostat stainless steel (which can also generate detectable signals in the NV) with a shorter time scale compared to captures on Hydrogen. With the final 5000 ppm GdSO concentration we expect to reduce the neutron capture lifetime below 20 μs, as obtained by MC simulations for cryostat neutrons.

Neutron capture properties

By using our GEANT4 simulations, we can investigate the fraction of neutrons captured on H, Gd, and other detector materials. In Tab. 4.3, three positions for the AmBe source are considered — Bottom CW6d0, Bottom CW10d3, and Top CW7d8. For each position, the fraction of generated neutrons that are captured in water is evaluated under two different concentrations of dissolved GdSO (0 ppm and 500 ppm). In the other cases, neutrons are mostly captured on the cryostat stainless steel and in LXe inside the TPC, with a small fraction involving other materials.

A significant increase in captures is observed with the presence of Gd, particularly in the Bottom CW10d3 and Top CW7d8 positions (as indicated by the values in paren-

Source	Pure water	500 ppm GdSO	Relative increase
AmBe - Bottom CW6d0	98.1%	98.9%	+0.8%
AmBe - Bottom CW10d3	56.3%	66.7%	+18%
AmBe - Top CW7d8	59.3%	68.9%	+16%

Table 4.3: Fraction of generated neutrons, from three different AmBe positions, captured in water for the pure water NV configuration and with 500 ppm Gd-sulphate concentration.

Source	Relative fraction captured on Gd	Relative fraction captured on H
AmBe - Bottom CW6d0 [500 ppm GdSO]	62.4%	35.0%
AmBe - Bottom CW10d3 [500 ppm GdSO]	63.3%	34.3%
AmBe - Top CW7d8 [500 ppm GdSO]	63.1%	34.4%

Table 4.4: Relative fraction of neutrons captured on Gd and on H, calculated among those captured in Gd-water, with 500 ppm GdSO concentration.

theses, which represent relative variation between the case of pure water and 500 ppm GdSO), as these are closer to the cryostat. The shorter mean capture time of Gd plays a crucial role, allowing neutrons to be captured before entering the TPC or being absorbed by the stainless steel of the cryostat. For the Bottom CW6d0 position, the increase is less notable because this position is located more in the center of the NV (as detailed in Section 3.4.1). In this case, most captures occur in water before the neutrons have a chance to escape.

Furthermore, an analysis was conducted to determine how many neutron captures occurring in water were on Gd or H in the presence of 500 ppm GdSO. The results are presented in Tab. 4.4, showing that $\sim 63\%$ of these occur on Gadolinium for all the three positions considered (Bottom CW6d0, Bottom CW10d3 and Top CW7d8), while $\sim 34\%$ of neutrons are captured on Hydrogen and the rest mainly on Oxygen. This value agrees with the predictions discussed in Section 4.4.2 and visible in Fig. 4.15b.

Conclusions

Dark Matter (DM) remains one of the greatest mysteries in modern astrophysics, constituting approximately 85% of the universe's total mass. Despite its significant gravitational influence, DM has evaded direct detection, with Weakly Interacting Massive Particles (WIMPs) being leading candidates.

The XENONnT experiment aims to detect WIMPs using a dual-phase Time Projection Chamber (TPC) with liquid Xenon as the target material. Understanding and mitigating background signals, particularly neutron-induced events, is crucial for enhancing the sensitivity of the detector in the search for WIMPs. For this reason, the XENONnT experiment is surrounded by two concentric water Cherenkov detectors, a Muon Veto and a Neutron Veto (NV), which respectively aim at detecting background muons and neutrons. This thesis is focused on the performance of the NV system, particularly after the introduction of Gadolinium started in October 2023 after the first two Scientific Runs (SR0 and SR1) where the NV was operated with demineralized water. SR2 marked the beginning of operations with a Gd-doped NV to improve the rejection of neutron background events.

XENONnT employs a unified simulation framework capable of producing detailed simulations for each individual subdetector. In particular, the Hitlet Simulator is tailored for the NV, tracking gamma-ray interactions resulting from neutron captures and generating simulated signals that closely replicate those observed in real data. The NV response to neutron captures is calibrated using an Americium Beryllium (AmBe) neutron source.

The results from Montecarlo (MC) simulations demonstrate the effectiveness of the NV in detecting neutron capture events. The AmBe calibration data, obtained using both pure water and 500 ppm GdSO (current concentration), revealed substantial improvements in neutron detection efficiency, and the MC simulations are in agreement with them. The introduction of Gd resulted in a significant reduction in neutron capture lifetime, from 163 μs in pure water to 75 μs in Gd-doped water, indicating faster neutron capture processes. Moreover, the neutron tagging efficiency in a 250 μs window increased from 53% in SR0 with pure water to 77% with 500 ppm GdSO in SR2. This corresponds to a reduction of a factor 2 in the neutron background compared to the previous runs with demineralized water, in agreement with the predictions from MC simulations.

In conclusion, the introduction of Gd into the Neutron Veto system has significantly enhanced the XENONnT experiment's ability to suppress neutron-induced background events, showing a good matching between simulation and experimental data. This improvement paves the way for greater sensitivity in future DM searches, bringing the XENONnT experiment closer to achieving its goal of detecting WIMPs.

Bibliography

[1] E. Corbelli and P. Salucci, "The extended rotation curve and the dark matter halo of M33," *Monthly Notices of the Royal Astronomical Society*, vol. 311, no. 2, pp. 441–447, 01 2000. [Online]. Available: https://doi.org/10.1046/j.1365-8711.2000.03075.x

[2] D. Clowe, A. Gonzalez, and M. Markevitch, "Weak-Lensing Mass Reconstruction of the Interacting Cluster 1E 0657–558: Direct Evidence for the Existence of Dark Matter," *The Astrophysical Journal*, vol. 604, no. 2, p. 596, apr 2004. [Online]. Available: https://dx.doi.org/10.1086/381970

[3] M. C. Weisskopf, B. Brinkman, C. Canizares, G. Garmire, S. Murray, and L. P. V. Speybroeck, "An Overview of the Performance and Scientific Results from the Chandra X-Ray Observatory," *Publications of the Astronomical Society of the Pacific*, vol. 114, no. 791, p. 1, jan 2002. [Online]. Available: https://dx.doi.org/10.1086/338108

[4] D. Clowe, M. Bradač, A. H. Gonzalez, M. Markevitch, S. W. Randall, C. Jones, and D. Zaritsky, "A Direct Empirical Proof of the Existence of Dark Matter," *The Astrophysical Journal*, vol. 648, no. 2, p. L109, aug 2006. [Online]. Available: https://dx.doi.org/10.1086/508162

[5] A. Einstein, "Lens-Like Action of a Star by the Deviation of Light in the Gravitational Field," *Science*, vol. 84, no. 2188, pp. 506–507, 1936. [Online]. Available: https://www.science.org/doi/abs/10.1126/science.84.2188.506

[6] M. Bartelmann, "Gravitational lensing," *Classical and Quantum Gravity*, vol. 27, no. 23, p. 233001, nov 2010. [Online]. Available: https://dx.doi.org/10.1088/0264-9381/27/23/233001

[7] Weisskopf, M. C. and Brinkman, B. and Canizares, C. and Garmire, G. and Murray, S. and Van Speybroeck, L. P., "An overview of the performance and scientific results from the Chandra X-ray Observatory (CXO)," *Publ. Astron. Soc. Pac.*, vol. 114, pp. 1–24, 2002.

[8] N. Aghanim *et al.*, "Planck 2018 results. VI. Cosmological parameters," *Astron. Astrophys.*, vol. 641, p. A6, 2020, [Erratum: Astron.Astrophys. 652, C4 (2021)].

[9] E. Collaboration, "Planck's view of the Cosmic Microwave Background," 2018. [Online]. Available: https://sci.esa.int/s/wQdrX4A

[10] P. Di Gangi, "The Xenon Road to Direct Detection of Dark Matter at LNGS: The XENON Project," *Universe*, vol. 7, no. 8, p. 313, 2021.

[11] E. Aprile *et al.*, "Design and Performance of the XENON10 Dark Matter Experiment," *Astropart. Phys.*, vol. 34, pp. 679–698, 2011.

[12] J. Angle *et al.*, "First Results from the XENON10 Dark Matter Experiment at the Gran Sasso National Laboratory," *Phys. Rev. Lett.*, vol. 100, p. 021303, 2008.

[13] ——, "Limits on spin-dependent WIMP-nucleon cross-sections from the XENON10 experiment," *Phys. Rev. Lett.*, vol. 101, p. 091301, 2008.

[14] E. Aprile *et al.*, "The XENON100 Dark Matter Experiment," *Astropart. Phys.*, vol. 35, pp. 573–590, 2012.

[15] ——, "Dark Matter Results from 225 Live Days of XENON100 Data," *Phys. Rev. Lett.*, vol. 109, p. 181301, 2012.

[16] ——, "Limits on spin-dependent WIMP-nucleon cross sections from 225 live days of XENON100 data," *Phys. Rev. Lett.*, vol. 111, no. 2, p. 021301, 2013.

[17] E. Aprile, "The XENON1T Dark Matter Search Experiment," *Springer Proc. Phys.*, vol. 148, pp. 93–96, 2013.

[18] E. Aprile *et al.*, "Dark Matter Search Results from a One Ton-Year Exposure of XENON1T," *Phys. Rev. Lett.*, vol. 121, no. 11, p. 111302, 2018.

[19] ——, "Constraining the spin-dependent WIMP-nucleon cross sections with XENON1T," *Phys. Rev. Lett.*, vol. 122, no. 14, p. 141301, 2019.

[20] ——, "Search for inelastic scattering of WIMP dark matter in XENON1T," *Phys. Rev. D*, vol. 103, no. 6, p. 063028, 2021.

[21] ——, "Search for Coherent Elastic Scattering of Solar ^{8}B Neutrinos in the XENON1T Dark Matter Experiment," *Phys. Rev. Lett.*, vol. 126, p. 091301, Mar 2021. [Online]. Available: https://link.aps.org/doi/10.1103/PhysRevLett.126.091301

[22] ——, "Emission of single and few electrons in XENON1T and limits on light dark matter," *Phys. Rev. D*, vol. 106, no. 2, p. 022001, 2022.

[23] ——, "Searching for Heavy Dark Matter near the Planck Mass with XENON1T," *Phys. Rev. Lett.*, vol. 130, no. 26, p. 261002, 2023.

[24] ——, "Projected WIMP sensitivity of the XENONnT dark matter experiment," *JCAP*, vol. 11, p. 031, 2020.

[25] L. Marti *et al.*, "Evaluation of gadolinium's action on water Cherenkov detector systems with EGADS," *Nucl. Instrum. Meth. A*, vol. 959, p. 163549, 2020.

[26] A. Renshaw, "Research and Development for a Gadolinium Doped Water Cherenkov Detector," *Phys. Procedia*, vol. 37, pp. 1249–1256, 2012.

[27] E. Hogenbirk, J. Aalbers, P. A. Breur, M. P. Decowski, K. van Teutem, and A. P. Colijn, "Precision measurements of the scintillation pulse shape for low-energy recoils in liquid Xenon," *JINST*, vol. 13, no. 05, p. P05016, 2018.

[28] E. Aprile and T. Doke, "Liquid Xenon Detectors for Particle Physics and Astrophysics," *Rev. Mod. Phys.*, vol. 82, pp. 2053–2097, 2010.

[29] E. Aprile *et al.*, "First Dark Matter Search with Nuclear Recoils from the XENONnT Experiment," *Phys. Rev. Lett.*, vol. 131, no. 4, p. 041003, 2023.

[30] J. Aalbers *et al.*, "DARWIN: towards the ultimate dark matter detector," *JCAP*, vol. 11, p. 017, 2016.

[31] ——, "A next-generation liquid xenon observatory for dark matter and neutrino physics," *J. Phys. G*, vol. 50, no. 1, p. 013001, 2023.

[32] E. Aprile *et al.*, "Projected WIMP sensitivity of the XENONnT dark matter experiment," *JCAP*, vol. 11, p. 031, 2020.

[33] ——, "Physics reach of the XENON1T dark matter experiment," *JCAP*, vol. 04, p. 027, 2016.

[34] S. Agostinelli *et al.*, "GEANT4 - a simulation toolkit," *Nucl. Instrum. Meth. A*, vol. 506, pp. 250–303, 2003.

[35] J. Allison *et al.*, "Recent developments in Geant4," *Nucl. Instrum. Meth. A*, vol. 835, pp. 186–225, 2016.

[36] K. Abe *et al.*, "Calibration of the Super-Kamiokande Detector," *Nucl. Instrum. Meth. A*, vol. 737, pp. 253–272, 2014.

[37] L. Marti *et al.*, "Evaluation of gadolinium's action on water Cherenkov detector systems with EGADS," *Nucl. Instrum. Meth. A*, vol. 959, p. 163549, 2020.

[38] Y. Namba and H. Tsuwa, "Surface Properties of Polished Stainless Steel," *CIRP Annals*, vol. 29, no. 1, pp. 409–412, 1980. [Online]. Available: https://www.sciencedirect.com/science/article/pii/S0007850607613614

[39] F. Casadei, "The XENONnT Neutron Veto: commissioning of the Gadolinium-water purification system," Master's thesis, Università di Bologna, 2023. [Online]. Available: http://amslaurea.unibo.it/28775/

[40] T. Tanaka *et al.*, "Gamma-ray spectra from thermal neutroncapture on gadolinium-155 and naturalgadolinium," *PTEP*, vol. 2020, no. 4, p. 043D02, 2020.

[41] Andrea Mancuso, "The XENONnT neutron veto: design, construction and performance," Ph.D. dissertation, alma, Giugno 2024. [Online]. Available: http://amsdottorato.unibo.it/11437/

[42] XENONnT collaboration, "Epix - XENONnT." [Online]. Available: https://github.com/XENONnT/epix

[43] Triangle Universities Nuclear Laboratory, "Nuclear Data Evaluation Project." [Online]. Available: https://nucldata.tunl.duke.edu/nucldata/

[44] J. Scherzinger *et al.*, "Tagging fast neutrons from an ^{241}Am/^{9}Be source," *Appl. Radiat. Isot.*, vol. 98, pp. 74–79, 2015.

[45] I. Murata *et al.*, "Neutron and gamma-ray source-term characterization of AmBe sources in Osaka University," *Progress in Nuclear Science and Technology 4*, p. 345–348, 2014.

[46] E. Aprile *et al.*, "Response of the XENON100 Dark Matter Detector to Nuclear Recoils," *Phys. Rev. D*, vol. 88, p. 012006, 2013.

[47] H. Ito *et al.*, "Analyzing the neutron and γ-ray emission properties of an americium–beryllium tagged neutron source," *Nucl. Instrum. Meth. A*, vol. 1057, p. 168701, 2023.

[48] W. Wilson *et al.*, "SOURCES - 4A," Los Alamos (USA), Tech. Rep., 1999.

[49] E. Aprile *et al.*, "The neutron background of the XENON100 dark matter search experiment," *J. Phys. G*, vol. 40, p. 115201, 2013.

[50] A. Kish, "Dark matter search with the XENON100 experiment," Ph.D. dissertation, Universität Zürich (Switzerland), 2011.

List of Figures